THE ENERGY BALANCE OF AN URBAN CANYON

by

MANUEL NUNEZ

B.Sc., University of Montreal, 1963
M.Sc., McMaster University, 1971

A THESIS SUBMITTED IN PARTIAL FULFILMENT OF

THE REQUIREMENTS FOR THE DEGREE OF

DOCTOR OF PHILOSOPHY

in the Department
of

Geography

We accept this thesis as conforming to the required standard

THE UNIVERSITY OF BRITISH COLUMBIA

December, 1974

Department of GEOGRAPHY

The University of British Columbia
Vancouver 8, Canada

Date JAN 23, 1975

ABSTRACT

A review of the literature indicates that there are deficiencies in numerical models which describe the sensible heat flux at the complex urban interface. Similarly, experimental techniques are not applicable to the urban area (e.g., Bowen's ratio, aerodynamic methods) or can only be applied at a sufficient height above the roughness elements (eddy correlation). This study investigates an experimental approach to calculating the sensible heat flux for cloudless skies and light winds. Using the energy balance at the surface, this term is obtained as a residual if the other terms are measured.

The experiment was conducted in what was considered to be the essential unit of the urban structure: the 'urban canyon' consisting of the combination of walls and ground (street) and the air volume contained between two adjacent buildings. If the fluxes of sensible heat are known at the three canyon surfaces, then the sensible heat released to or from the atmosphere is obtained if proper consideration is given to advection and heat storage change in the canyon-air volume.

The canyon chosen was located in central Vancouver, B.C., was aligned North-South and consisted of two concrete food processing plants, painted white and separated by a clay-base floor covered by gravel. The canyon was approximately 8 m in width, 6 m in height and 79 m in length. A boom was installed across the canyon top and served as a trackway for a movable carriage and a vertical mast. Eight net radiometers and thermocouple air temperature sensors were mounted on the mast, and seventeen subsurface flux plates were installed on the canyon walls and ground. A lysimeter measured the surface water loss. In addition to these measurements, special experiments were conducted to investigate the individual roles of advection, solar radiation and subsurface heat storage in the canyon.

Results indicate that the solar radiation received along the walls is a function of the solar zenith and azimuth angle. The average solar flux received by each canyon surface is characterized by a peak; with added secondary maxima on each wall corresponding to periods of maximum irradiance on the opposite wall. The albedo of the canyon system shows two distinct peaks at the times of maximum irradiance of the white walls. At noon the albedo of the canyon system approximates that of the canyon floor.

Both the net radiation and subsurface heat flux respond to solar radiation during the day and thus a similar dependence on solar zenith and azimuth angle is observed for these quantities. At night the net long-wave radiation at locations in the canyon varies linearly with the sky view factor.

The transport of heat by advection into or out of the canyon air volume depends to a large extent on the wind field. With winds ∿2 m s^{-1} on cloudless days, the net advection gives rise to an upward flux of approximately 70 W m^{-2}. With winds of 1 m s^{-1} the corresponding advection is 15 W m^{-2}. In the absence of strong advective fluxes, the partitioning of the radiant energy, across the canyon top, and at solar noon on a clear summer day is as follows: net all wave radiation flux: 510 W m^{-2}, sensible heat flux: 320 W m^{-2}, latent heat flux: 50 W m^{-2}, subsurface heat flux: 140 W m^{-2}.

At night the wind field drops below 1 m s^{-1} and a balance is established between the net radiation deficit and the subsurface heat flux which flows towards the canyon-air volume. Typical values for both are 60 W m^{-2} at the canyon top. Both the sensible and latent heat fluxes are close to zero. Measurements indicate that under these nocturnal conditions, the *volume* divergence of net radiation is the main cooling mechanism for the canyon-air volume. The cooling may also be approximated by the Brunt formula curve which employs a mean canyon surface admittance and a net radiation across the canyon top.

A modelling scheme is devised which calculates solar radiation as the main energy source during periods of sunny skies and light winds. Linkages are then sought, via canyon measurements, between the net solar radiation, the net all-wave radiation and the subsurface heat flux. The sensible heat flux is the end result. The results appear

promising, although more measurements are needed over a variety of urban surfaces.

TABLE OF CONTENTS

Page

CHAPTER

LIST OF TABLES

LIST OF FIGURES

FIGURE Page

FIGURE Page

FIGURE Page

LIST OF SYMBOLS

SYMBOL	DESCRIPTION	TYPICAL UNITS
A_1	Cross-sectional area in canyon (=W.H)	m^2
A_2	Cross-sectional area in canyon (=L.H)	m^2
A_i	ith surface of the canyon-air volume	m^2
a	Y-intercept obtained from a linear regression of Q^* vs L^*	
b	Slope of the regression of Q^* vs L^*	
C	Heat capacity of a solid	$J\ m^{-3} K^{-1}$
$\bar{C}$	Heat capacity averaged over the three canyon surfaces	$J\ m^{-3}\ K^{-1}$
C_x	Constant in turbulent transfer equation	
c'	Specific heat of a surface	$J\ kg^{-1}\ K^{-1}$
c_p	Specific heat of air at constant pressure	$J\ kg^{-1}\ K^{-1}$

SYMBOL	DESCRIPTION	TYPICAL UNITS
D	Diffuse incoming solar radiation incident on canyon top	$W\ m^{-2}$
D_e, D_w, D_g	Diffuse solar radiation incident on the east, west and ground surfaces of the canyon	$W\ m^{-2}$
F_1, F_2	Fraction of the incoming diffuse radiation D that is incident on either of the two canyon walls, and ground respectively	
H'	Vertical distance between the top of the eastern wall and the shadow height of the irradiated wall	m
H	Canyon height	m
H_e	Height of east wall in canyon	m
h	Surface heating coefficient	
I_o	Extra-terrestrial solar radiation intensity	$W\ m^{-2}$
I'	Incoming direct radiation after depletion by Rayleigh scattering, water vapour and aerosols	$W\ m^{-2}$
j_1, j_2	Direction cosines of two vectors in calculation of ψ	deg

SYMBOL	DESCRIPTION	TYPICAL UNITS
$K\downarrow_t, K\uparrow_t$	Incoming and outgoing solar flux on the canyon system (averaged across the canyon top) respectively	$W\ m^{-2}$
$K\downarrow_i, K\uparrow_i$	Individual measurements of incoming and outgoing radiation at canyon top	$W\ m^{-2}$
$K\downarrow_e, K\downarrow_w, K\downarrow_g$	Incoming solar radiation averaged over the east, west and ground surfaces of the canyon respectively	$W\ m^{-2}$
K^*_e, K^*_w, K^*_g	Net solar radiation averaged over the east, west and ground surfaces of the canyon respectively	$W\ m^{-2}$
K^*_t	Net solar flux of the canyon system (averaged across the canyon top)	$W\ m^{-2}$
$K_{\downarrow}'$	Mean solar radiation received on a canyon surface from an irradiated second canyon surface	$W\ m^{-2}$
K_x	Eddy diffusivity for heat or water vapour	$m^2\ s^{-1}$
K_H	Eddy diffusivity of heat	$m^2\ s^{-1}$
K_H'	Eddy diffusivity of heat for the canyon system	$m^2\ s^{-1}$
k	Thermal conductivity	$W\ m^{-1}\ K^{-1}$

SYMBOL	DESCRIPTION	TYPICAL UNITS
$\bar{k}$	Thermal conductivity averaged over the three canyon surfaces	$W\ m^{-1}\ K^{-1}$
k_s, k_c	Thermal conductivity of sand and concrete respectively	$W\ m^{-1}\ K^{-1}$
L	Arbitrary canyon length	m
$L\downarrow$, $L\uparrow$	Incoming and outgoing long-wave radiation flux respectively	$W\ m^{-2}$
L^*	Net long-wave radiation flux	$W\ m^{-2}$
L^*_g	Mean net long-wave radiation along the canyon ground	$W\ m^{-2}$
m	Solar air mass	
P	Per cent of the canyon walls in sunlight	
p_1, p_2	Direction cosines of two vectors in calculation of ψ	deg.
Q^*	Net all-wave radiation flux	$W\ m^{-2}$
Q^*_e, Q^*_w, Q^*_g	Net all-wave radiation averaged over the east, west and ground surfaces of the canyon respectively	$W\ m^{-2}$

SYMBOL	DESCRIPTION	TYPICAL UNITS
Q^*_i	Net all wave radiation averaged over the ith surface of the canyon	$W\ m^{-2}$
Q^*_t	Net all-wave radiation flux of the canyon system (averaged across the canyon top)	$W\ m^{-2}$
$\bar{Q}^*$	Net all-wave radiation averaged over the three canyon surfaces	$W\ m^{-2}$
Q^*_N, Q^*_S	Net all-wave radiation in the vertical plane and averaged over the north and south cross-section of the canyon respectively	$W\ m^{-2}$
$[Q^*]$	Net storage of Q^* in the canyon-air volume	$J\ s^{-1}$
$[Q^*]_c$	Net storage of radiant energy in the canyon-air volume due to divergence in the net all-wave radiation normal to the canyon cross-section	$J\ s^{-1}$
$[Q^*]_H$	Net storage of radiant energy in the canyon-air volume due to divergence in the all-wave radiation in a plane normal to the canyon cross-section	$J\ s^{-1}$
$[Q_{Adv}]$	Advected heat in the canyon-air volume due to horizontal mass transport	$J\ s^{-1}$

SYMBOL	DESCRIPTION	TYPICAL UNITS
Q_E	Latent heat flux	$W\ m^{-2}$
Q_{Et}	Latent heat flux of the canyon system (averaged across the canyon top)	$W\ m^{-2}$
Q_F	Anthropogenic heat flux released from buildings	$W\ m^{-2}$
Q_G	Subsurface heat flux	$W\ m^{-2}$
$Q_{G(o)}$	Conductive heat flux at the interface	$W\ m^{-2}$
$Q_{G(z)}$	Subsurface heat flux at depth z	$W\ m^{-2}$
Q_{Ge}, Q_{Gw}, Q_{Gg}	Spatially averaged subsurface heat flux for the east, west and ground surfaces respectively	$W\ m^{-2}$
Q_{Gt}	Subsurface heat flux of the canyon system	$W\ m^{-2}$
$\bar{Q}_G$	Subsurface heat flux averaged over the three canyon surfaces	$W\ m^{-2}$
Q_H	Sensible heat flux	$W\ m^{-2}$
Q_{He}, Q_{Hw}, Q_{Hg}	Sensible heat flux to or from the east, west and ground surfaces respectively	$W\ m^{-2}$

SYMBOL	DESCRIPTION	TYPICAL UNITS
Q_{Ht}	Sensible heat flux of the canyon system (averaged across the canyon top)	$W\ m^{-2}$
q_1, q_2	Direction cosines of two vectors in calculation of ψ	deg
R	Relative efficiency of the canyon system in trapping solar radiation when compared to a horizontal area	
r	Radius vector of the sun	
S_r	Rayleigh scattering coefficient	
S_w	Scattering coefficient for water vapour	
S_x	Climatological variable in the turbulent transfer (Equation 1.2)	
T_o, T_1	Instantaneous air temperatures in the canyon, averaged over the canyon cross-section and separated by a distance L	K
T_2	Instantaneous air temperature averaged over the canyon top	K
$\bar{T}_o, \bar{T}_1, \bar{T}_2$	Time-average of instantaneous temperatures T_o, T_1 and T_2 respectively	K

SYMBOL	DESCRIPTION	TYPICAL UNITS
T_o', T_1', T_2'	Instantaneous temperature departures of T_o, T_1, T_2 from $\bar{T}_o, \bar{T}_1, \bar{T}_2$ respectively	K
$\bar{T}$	Mean air temperature	K
T_s	Mean surface temperature in the canyon	K
T_z	Subsurface temperature	K
T_w, T_g	Surface temperatures of the canyon walls and ground respectively	K
t	Unit of time	s
u_o, u_1	Instantaneous wind velocities in the canyon, averaged over the canyon cross-section and separated by a distance L	$m\ s^{-1}$
$\bar{u}_o, \bar{u}_1$	Time-average of instantaneous horizontal velocities u_o and u_1, respectively	$m\ s^{-1}$
u_o', u_1'	Instantaneous velocity departures of u_o and u_1 from $\bar{u}_o$ and $\bar{u}_1$ respectively	
V	Canyon-air volume	m^{-3}
VF	View factor for a surface	

SYMBOL	DESCRIPTION	TYPICAL UNITS
VF_e, VF_w, VF_s	East wall, west wall and sky view-factors for points along the canyon surfaces	
VF_{i-J}	View factor for the irradiated ith surface as seen by the jth surface	m
W	Canyon width	m
w	Instantaneous vertical velocity averaged over the canyon top (A_2)	$m\ s^{-1}$
$\bar{w}$	Time-average of vertical velocity w	$m\ s^{-1}$
w'	Instantaneous departure of w from $\bar{w}$	$m\ s^{-1}$
X	Distance between sensing element and base of the vertical surface in view factor calculation	m
X_m, X_A	Fraction of the canyon ground that is in shadow in the morning and afternoon, respectively	
Y	Height of vertical surface in view factor calculation	m
Z'	Zenith angle of the Sun	deg

SYMBOL	DESCRIPTION	TYPICAL UNITS
z	Unit of height or depth	m
α	Albedo of a surface	
$\alpha_e, \alpha_w, \alpha_g$	Individual albedos for the east, west and ground surfaces of the canyon respectively	
α_t	Albedo of the canyon system (averaged across the canyon top)	
α'	Reflectivity for long-wave radiation	
β'	Bowen's ratio	
β'_t	Bowen's ratio for the canyon top	
Δ	Finite difference approximation	
ε	Emissivity of a surface	
Θ	Potential temperature	K
Θ'	Arctan (Y/X)	deg

SYMBOL	DESCRIPTION	TYPICAL UNITS
κ	Thermal diffusivity of a surface	$m^2 s^{-1}$
λ	Slope of L^* vs K^* relation	
$\bar{\mu}$	Mean thermal admittance of the three canyon surfaces	$J\ m^{-2}\ K^{-1}\ S^{-½}$
ρ	Air density	$kg\ m^{-3}$
ρ'	Density of a surface	$kq\ m^{-3}$
σ	Stefan-Boltzmann constant	$W\ m^{-2}\ K^{-4}$
ϕ_w	Absorption coefficient for water vapour	
ϕ'	Azimuth angle between the solar beam and canyon longitudinal direction	deg
τ_d	Transmission coefficient for aerosol absorption and scattering	
$\tau_{d'}$	Transmission coefficient for aerosol scattering or absorption	
ψ	Solar angle of incidence for the canyon walls	deg
$\Omega_e, \Omega_w, \Omega_g$	Solar irradiance from secondary reflections on the east, west and ground surfaces of the canyon respectively	$W\ m^{-2}$

ACKNOWLEDGEMENTS

I would like to gratefully acknowledge the encouragement, assistance and suggestions given to me by my supervisor, Dr. T. R. Oke.

I am also indebted to members of my committee and especially to Mr. M. Church of the Department of Geography, to Dr. S. Pond of the Institute of Oceanography, U.B.C., for their many helpful discussions, and to Dr. T. A. Black of the Soil Science Department, who provided laboratory calibration facilities.

The author is grateful to Mr. K. Nicol, and my brother, Mr. J. Nunez, who helped in the data collection; to Mr. A. Ramirez who did the drafting and to Miss S. Aizenman who typed the thesis.

This project was conducted in the grounds of Kraft Co. and Pine Tree Nut Co. and to them I am grateful for the use of their facilities.

This project was funded through National Research Council, and Atmospheric Environment Service grants to Dr. T. R. Oke.

CHAPTER 1

INTRODUCTION

A. APPROACHES TO FLUX ESTIMATION IN URBAN AREAS

Most work in urban climatology has been directed towards describing the time and space distributions of climatological parameters such as air temperature, water vapour, wind speed, and air pollutants (for reviews of this work see Kratzer, 1956; Peterson, 1969; and Oke, 1974). Although this has increased our knowledge of the climatic effects of urbanization, it has not resulted in a clear understanding of the mechanisms lying at the root of urban climatology. In particular it is necessary to further understand the behaviour of the fluxes transferring energy, mass and momentum between the atmosphere and the urban interface.

This study is centrally concerned with the urban interface energy balance, but it is important to point out that the energy fluxes cannot be divorced from interactions with the fluxes of mass and momentum. For example, the exchange of both short and long-wave radiation between the atmosphere and the surface is modified by the presence of pollutants; the partitioning of available energy is strongly influenced by the availability of evaporable water; and the efficiency of turbulent transport is partially controlled by the generation of forced convection.

In particular this study is concerned with the means whereby the sensible heat flux by turbulent transfer may be determined. Its importance in altering the thermal structure of the urban boundary layer is anticipated to be substantial (e.g., in controlling lapse rates and hence stability and pollution dispersion; in creation of the urban heat island; in estimating building and community heating requirements, etc.) but little detailed work is available.

Three classes of approach have been undertaken previously in attempting to estimate the magnitude of the urban sensible heat flux, namely numerical models, mixing depth models and measurement. The theoretical models are usually based upon the following equations:

$$Q^* + Q_E + Q_H + Q_G = 0 \tag{1.1}$$

$$\frac{\partial S_x}{\partial t} = C_x \frac{\partial}{\partial z}\left(K_x \frac{\partial S_x}{\partial z}\right) + \text{Advection} \tag{1.2}$$

$$\frac{\partial T_z}{\partial t} = k \frac{\partial^2 T_z}{\partial z^2} \tag{1.3}$$

where,

Q^* = net all-wave radiation,

Q_E = latent heat flux,

Q_H = sensible heat flux,

Q_G = sub surface heat flux,

S_x = climatological variable (temperature, water vapour, etc.),

C_x = constant,

K_x = eddy diffusivity for property (heat, water vapour),

T_z = subsurface temperature,

k = subsurface thermal conductivity,

t = time,

z = height.

Equations 1.1, 1.2 and 1.3 are the two-dimensional forms of the surface energy balance, atmospheric turbulent transfer and sub-surface heat flux equations respectively. As a first approximation the advective term is ignored. Equations 1.1, 1.2 give a closed set if K_x, k and the surface boundary conditions are known, whence the sensible heat flux (Q_H) is obtained from:

$$Q_H = -\rho c_p K_H \frac{\partial \bar{T}}{\partial z} \tag{1.4}$$

where

ρ = air density,

c_p = specific heat of air at constant pressure,

$\bar{T}$ = mean air temperature.

This approach was taken by Myrup (1969) in his pioneering numerical model of the urban heat island. The model was not intended for research purposes, and for simplification avoided inclusion of advection, stability correction of K_H, and initially assumed $Q_E = 0$ in the city. Furthermore, a constant flux layer was assumed so that the model was not time-dependent. Nevertheless, some interesting results were obtained which illustrated the character of the urban energy balance. In his model surface effects are particularly significant. The model results showed air and surface temperatures to be strongly related to the amount of transpiring surface. The model was later applied to Sacramento, Calif. (Myrup and Morgan, 1972) by dividing the city into small cells and using representative values of albedo, emissivity, thermal conductivity, fraction of transpiring surface and heat capacity for each cell. Roughness lengths were employed using the method of Lettau (1969). Following this analysis, the authors were able to calculate the spatial distribution of the different surface energy balance components in Sacramento. Unfortunately independent measurements of these terms were not available probably because of experimental difficulties to be discussed later on in this chapter. It is reasonable to assume that more realistic descriptions of the energy transfers could be had by incorporating:

(a) stability-dependent eddy diffusivities,
(b) radiative flux divergence,
(c) the momentum transfer equation,
(d) advection and the equation of continuity,
(e) realistic surface boundary fluxes.

Some early boundary layer models exist which incorporate some of these features. Estoque (1963) used (a), (b) and (c) in his work which also included a constant flux layer followed by a transition layer. The model was meant to apply over a rural surface. Similar models have been developed by Pandolfo *et al.*

(1963) and Wu (1965) among others. Tag (1969) applied the Estoque model to an urban area and calculated surface temperature warming. Term (d) can be used to study the urban circulation system in the absence of external winds (Delage and Taylor, 1970; Vukovich, 1971) as well as to study the modification of rural air as it crosses the urban area. These later models represent the most advanced approach to date, and in most cases incorporate terms (a) to (d) (Estoque and Bhumralkar, 1970; Pandolfo *et al.*, 1971; Wagner and Yu, 1972).

Although most of these models recreate in some form the observed features of the urban heat island, there is need of experimental programmes to verify their results (see, for example, Tag, 1969; Bornstein, 1972; McElroy, 1972a, 1972b). In many real situations, the inhomogeneity of the surface may render the calculations of the eddy diffusivities based on established wind profile theory, invalid. Furthermore, although the urban boundary layer has been shown to exist as a mean property (Clarke, 1969; Oke and East, 1971; Tyson *et al.*, 1972) it must incorporate large inhomogeneities at the surface due to the complex nature of the urban atmosphere interface in space. Thus even though the heat flux at any point on the surface may be well behaved, its estimation from boundary layer theory may be incorrect.

Surface inhomogeneities may also cause difficulties in the calculation of realistic fluxes at or near the interface because current turbulent transfer theory is not applicable. Therefore it seems that category (e) is at present neglected in these models, and there is need for contributions in this area. However, due to the complexity of the flow, it is doubtful if purely theoretical approaches could be useful, even in regular idealized block-arrays. Instead, the input must come from experimental programmes to study the energy flow in this complex environment.

The mixing depth models on the other hand assume that at some critical height the irregularities in the surface fluxes have been smoothed to provide an integrated spatial average. This concept is used by Summers (1965) and Leahey and Friend (1971) equate the development of a thermal boundary layer to the surface heat flux with assumptions regarding the form of the wind and temperature profiles. Such an approach might appear attractive in estimating gross urban surface fluxes given the appropriate input information. However, some of the theoretical objections raised previously, plus the expense of providing the necessary data, make this approach impractical.

The measurement approach to the evaluation of Q_H in urban areas usually involves the use of micrometeorological techniques such as the Bowen ratio, aerodynamic or eddy correlation methods. Oke *et al.* (1972) have pointed out the relative merits and deficiencies of these approaches in the urban environment. They conclude that the first two approaches involve assumptions unlikely to be realized in the urban situation, but that the eddy correlation approach holds promise. Initial work with such a system has verified this (Yap and Oke, 1974), but also suggests that it should be employed at a sufficient height that local spatial variability is smoothed out. If the surface energy balance is required, this introduces the possibility of errors associated with any height variation in Q_H.

Given these difficulties in determining Q_H in the surface energy balance of the city, a new approach is attempted here.

B. RESEARCH APPROACH

The essence of the approach employed in this study is that Q_H may be obtained as a residual in the simple surface energy balance equation (Equation 1.1) if all other terms are accurately measured or otherwise determined. Much of the value of such an approach rests on the careful identification of what constitutes a significant urban surface. There are probably no truly representative urban *surfaces* such as those identified as characteristic of rural and other horizontal natural terrain for experimental purposes. However, there may be some typical urban surface *units* consisting of a combination of surfaces (both horizontal and vertical) whose basic form is repeated throughout the urban area. Here we specifically identify the 'urban canyon' as an important basic unit of the urban structure. It consists of the combination of walls, and ground (street) and the air volume contained between two adjacent buildings (Figure 1.1).

Such a physical arrangement represents a three-dimensional distortion of the horizontal surface case, and is characterized by complex radiative and aerodynamic exchanges below roof-level. The urban canyon together with simpler roof surfaces forms the lower boundary for most of the urban boundary layer, at least in the central portion of most cities. Such a concept is similar to, but independent of, that employed by Terjung and Louie (1973, 1974) where they identify a "radiation neighborhood" as a typical unit capable of integration to provide a synthetic city system.

The canyon considered in this thesis is essentially a two-dimensional example in which the transfer of energy between the atmosphere and the canyon cross-section is not dependent on the longitudinal distance along the canyon. Thus a real canyon situation was found which was of sufficient length and which was characterized by homogeneity in its longitudinal axis. This characteristic does not exclude the presence of advection but only assures that the energy exchanges are similar in the greater part of the canyon.

The suitability of applying the unit canyon results to a larger urban area (and other canyons) will, of course, depend on the character of the energy balance terms at the interface.

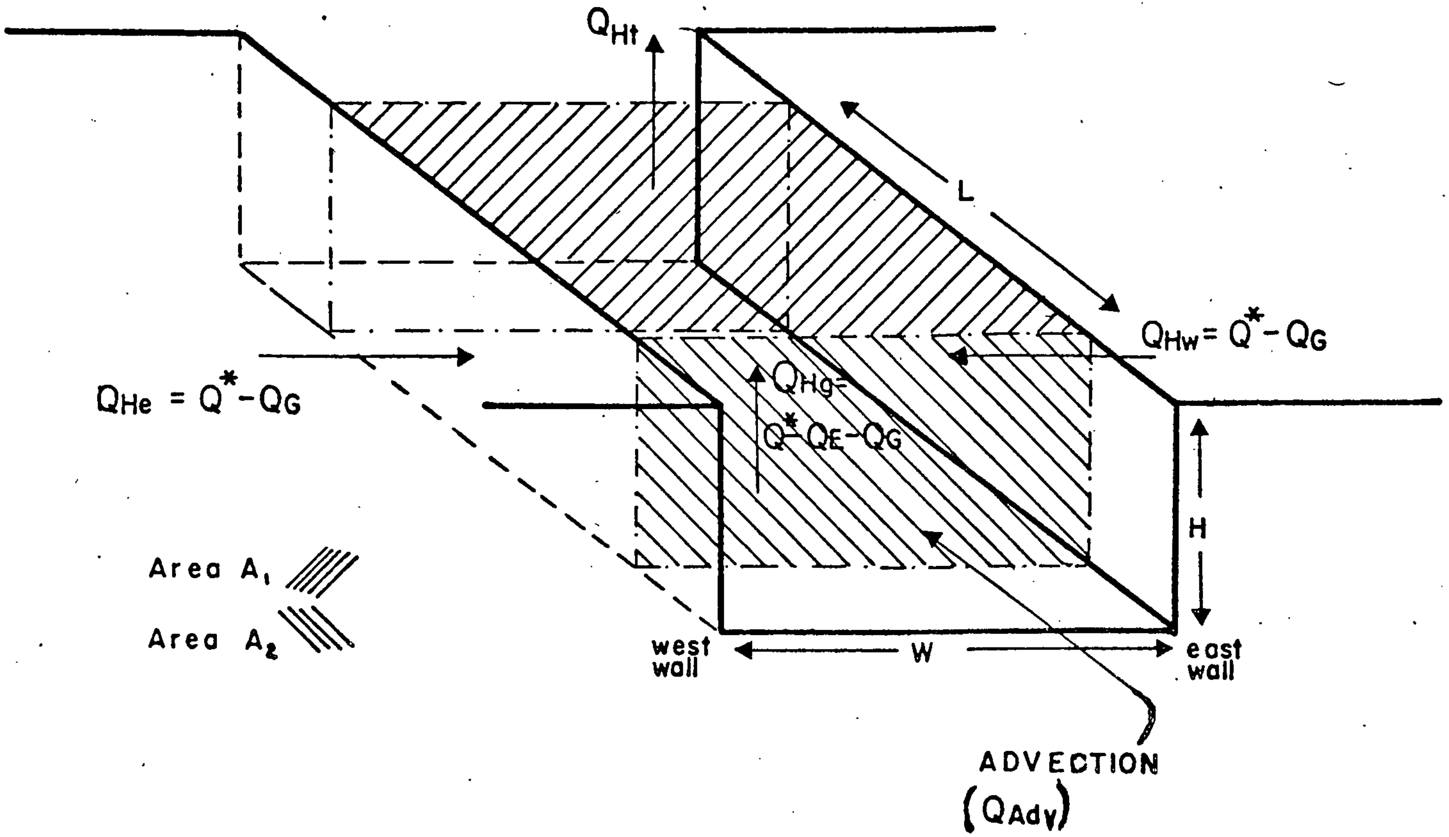

Fig. 1.1 Box model describing the flow of energy in the urban canyon.

If the radiation fluxes behave as well-defined functions of the physical properties of the canyon(e.g., dimensions, albedo, surface fabric) then these terms can be modelled in other canyon situations. Similarly if the horizontal transport of heat into, or out of, the canyon is small, then the implication is that the vertical exchange of heat is governed by processes occurring inside the canyon. Thus Q_H may be modelled in other canyon situations if it is shown to be a well-behaved function of the other energy balance terms.

This attempt at generalizing the canyon measurements implies that there must be some form of control on the external energy inputs to the canyon system (solar radiation and synoptic winds), otherwise the results will be biased and their applicability to other situations would be questionable. It was decided in this study to look at conditions which were as close to steady-state as possible: general large-scale subsidence weather characterized by clear skies, light winds and dry spells. These conditions are in themselves important since it is during these spells that air pollution and heat island anomalies have maximum effect (Summers, 1965).

Although the possibility of using the urban canyon as a modelling unit is considered here also, the central emphasis is upon examining the nature of the physical exchanges interacting within such a geometric configuration. The study of the urban canyon is important also for what it tells us about the climatic conditions within streets. For it is here that much of the biological activity of cities takes place (both animal and vegetative), and wherein some of the pollutants (particulate, gaseous, thermal and acoustic) are released. Equally it is where most of the studies of the climatic effects of urbanization have been conducted (e.g., automobile traverses of air temperature) but where the energetic basis for climatic interpretation is almost entirely lacking.

Assuming no phase changes of water in the air volume, the energy balance for the air volume contained in an urban canyon such as that in Figure 1.1 is given:

$$[Q_{Adv}] + (Q_{He} + Q_{Hw})\ H.L + Q_{Hg} \cdot W.L - Q_{Ht} \cdot W.L = \rho c_p \int_V \left(\frac{\partial \bar{T}}{\partial t} + \frac{\mathrm{div}\ Q^*}{\rho\ c_p} \right) dV \qquad (1.5)$$

where

$[Q_{Adv}]$ = advected heat due to horizontal transport,

Q_{He}, Q_{Hw}, Q_{Hg} = sensible heat flux to, or from, the east, west and ground surfaces respectively,

H, L, W = canyon height, length and width respectively,

Q_{Ht} = sensible heat flux through the canyon top,

$\rho c_p \int_V \frac{\partial \bar{T}}{\partial t}\ dV$ = rate of change of energy storage in the canyon-air volume V,

$\int_V \mathrm{div}\ Q^*\ dV$ = rate of change of energy storage due to net radiative divergence in the canyon-air volume.

The left-hand side of Equation 1.5 defines the net sensible heat input to the canyon-air volume. These terms therefore must be balanced on the right-hand side by the resulting change in the sensible energy storage (temperature) in the air volume plus (or minus) the net energy change due to radiative flux divergence. Under near calm conditions (commonly at night) the terms on the left-hand side will become small and the two terms on the right-hand side will provide the dominant interaction.

The divergence of net radiation in the canyon-air volume can be re-written as

$$\int_V \operatorname{div} Q^* dV = \sum_{i=1}^{6} Q_i^* A_i \tag{1.6}$$

where, Q_i^* defines the net radiant energy normal to the ith surface (A_i) of the canyon-air volume.

The Q_H fluxes for the canyon walls, if assumed to be impervious and dry, are given as:

$$Q_H = Q^* - Q_G \tag{1.7}$$

and for the canyon floor:

$$Q_H = Q^* - Q_G - Q_E \tag{1.8}$$

if some small amount of water is assumed to be available.

Given an appropriate sampling scheme over the canyon surfaces, all the terms in Equation 1.5 can thus be measured utilizing fairly standard meteorological instrumentation (e.g., flux plates, radiometers, a lysimeter and thermometers) with the exception of Q_{Ht}. This term then becomes solvable as the residual, and represents the flux of sensible heat to (or from) the urban boundary layer above the buildings. In combination with the sensible heat flux from the roof-tops this term is a fundamental lower boundary condition in the meso-scale energy balance of the city and its atmosphere.

The knowledge gained in evaluating the energy balance of the canyon-air volume via measurement provides help in establishing empirical relationships, and in testing theoretical models, which may then be applied to other canyon systems existing under similar constraints.

C. OBJECTIVES

The specific objectives of this study may be summarized as the following:

(i) to measure and interpret the nature of the energy balance terms (radiative, conductive and convective) at the interface of the component surfaces of an urban canyon,

(ii) to measure, compute and interpret the nature of heat fluxes (radiative and convective) involved in the energy balance of a canyon-air volume,

(iii) to generalize the results of (i) and (ii) towards their future incorporation into a modelling scheme describing the behaviour of Q_H at the urban/atmosphere interface.

CHAPTER 2

SITE, INSTRUMENTATION AND DATA ACQUISITION

A. GEOGRAPHIC SITUATION

1. Vancouver Region and Climate

The experimental studies were conducted in Vancouver, B.C. (49°N latitude, 123° W longitude) which is located at the mouth of the Fraser River on the Lower Mainland of British Columbia (Figure 2.1). The City of Vancouver is mainly residential except for commercial centres, and pockets of mainly light industry. The total population of the Greater Vancouver region is approximately one million, with the highest density located near the Central Business District (C.B.D.).

The macro-climatology of the Vancouver Region is characterized by wet, mild winters and dry, warm summers. The winter is dominated by the passage of Pacific disturbances caught up in the flow of the Westerlies. In the summer the northward extension of the Pacific Sub-Tropical High Pressure area brings generally cloudless skies and lighter winds, and the tendency for the development of important meso-scale climates. Detailed accounts of the climate of the region are given by Harry (1955), Harry and Wright (1967) and Hare and Thomas (1974).

The observations in this study were restricted to the summer months, and to days with cloudless skies and light winds.

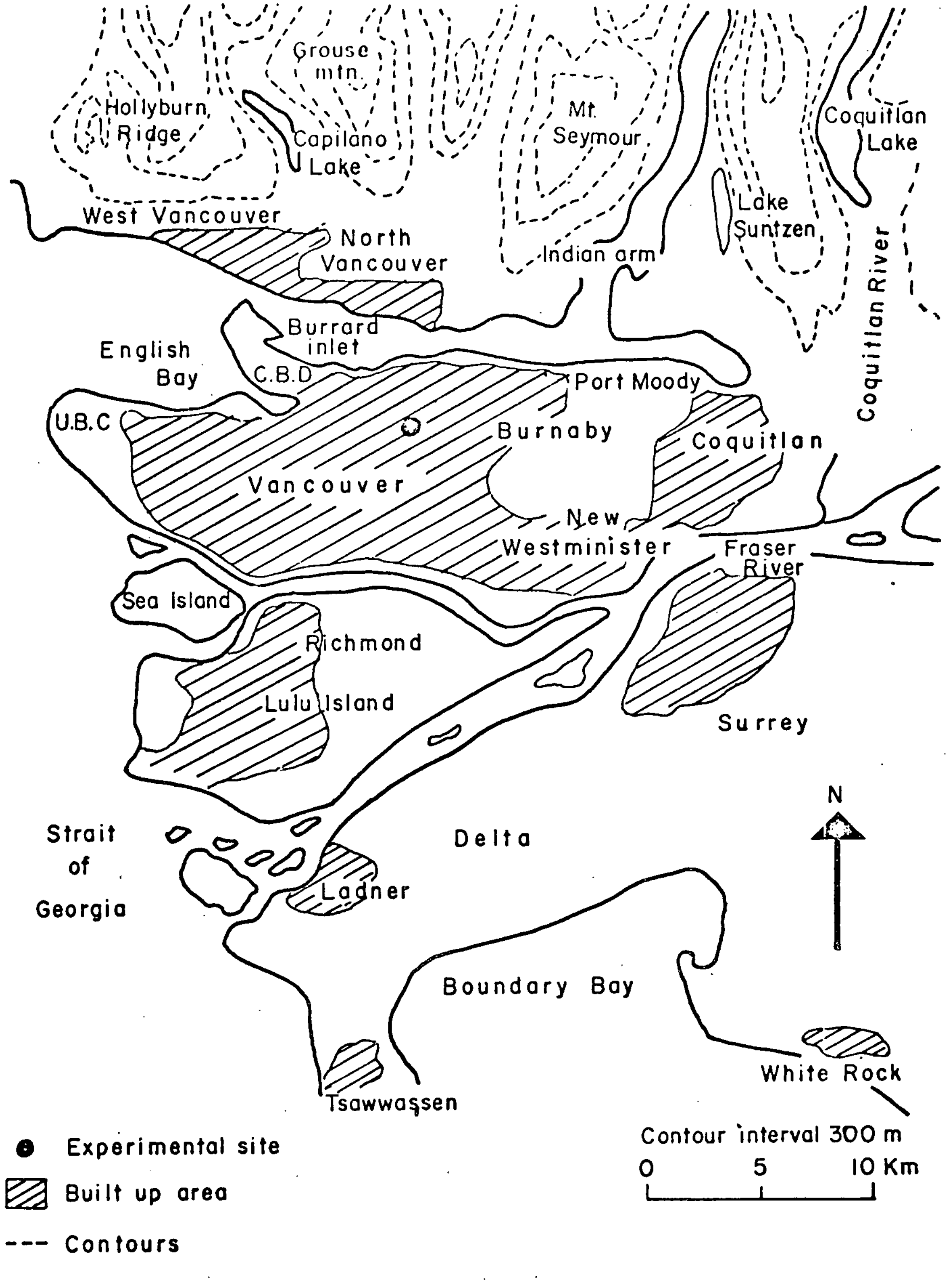

Fig. 2.1 The Greater Vancouver area.

Under such conditions the experimental site location (Figure 2.1) is likely to encounter a number of meso-scale phenomena. In particular, the wind regime is characterized by east-west oriented local winds generated by land/sea thermal differences and probably augmented by a mountain/valley circulation (Emslie, 1971). The diurnal wind-shift is very marked during this period. The meso-scale heat island of Vancouver is also well developed under anticyclonic weather, commonly resulting in urban/rural temperature differences of 5 degrees Celsius, and maximum differences of greater than 11 degrees Celsius on especially calm and clear nights (Oke, 1972). The heat island also shows a diurnal cycle with the maximum magnitude occurring 3-4h after sunset (Oke and Maxwell, 1974). An example of the heat island configuration is given in Figure 2.2 (Oke, 1974, personal communication). This shows the experimental site to be well within the heat island, but is not located in an area of sharp temperature gradient. Note also that the distribution of particulate matter from a study by Emslie and Salterthwaite (1966) shows some similarity with the heat island pattern (Figure 2.2). Spatial sampling of other pollutants is not sufficient to make similar comparisons, but discussion of available information is contained in B.C. Research Council (1970) and Lynch and Emslie (1972).

2. Urban Canyon Experimental Site

To fulfill the requirements of an urban canyon as out-

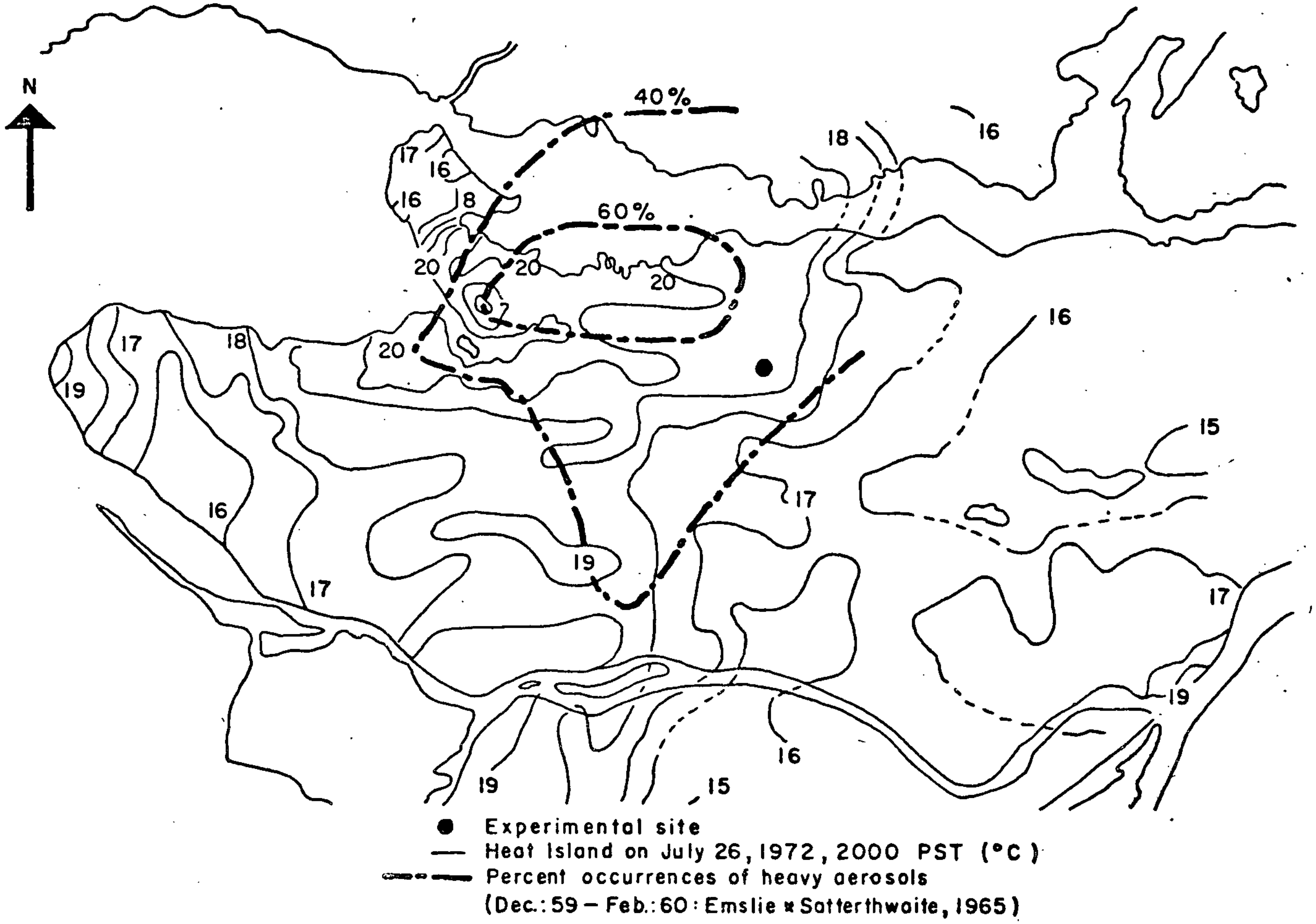

Fig. 2.2 Typical heat island configuration and air pollution distribution.

lined in Chapter 1, the following set of site criteria were deemed desirable on theoretical or purely practical grounds:

(a) canyon length ≥50 m,

(b) width: height ratio between 1:0.5 and 1:6,

(c) homogeneity of canyon surface materials,

(d) uniformity of surrounding structures,

(e) no windows or obstructions along canyon sides,

(f) no shadows in the canyon cast by external objects,

(g) impermeable canyon surfaces,

(h) freedom from traffic,

(i) easy access.

The selection of a site which fulfilled all of these nine criteria proved very difficult. The site selected did not fully conform with criteria (e), (f) and (g) but was satisfactory in all other respects.

The experimental canyon is located in a residential/ light industrial zone, 3.5 km south of Burrard Inlet, and 6 km south-east of the C.B.D. (Figure 2.1). It is located in a slight topographic depression, with a 1 in 12.5 slope to the north, and a 1 in 19 slope to the south. The neighbourhood location of the site is shown in Figure 2.3 which also includes the percentage of each block area which is composed of impervious materials. The area to the north of the site is composed mainly of industrial buildings (food processing and warehousing), whereas to the south

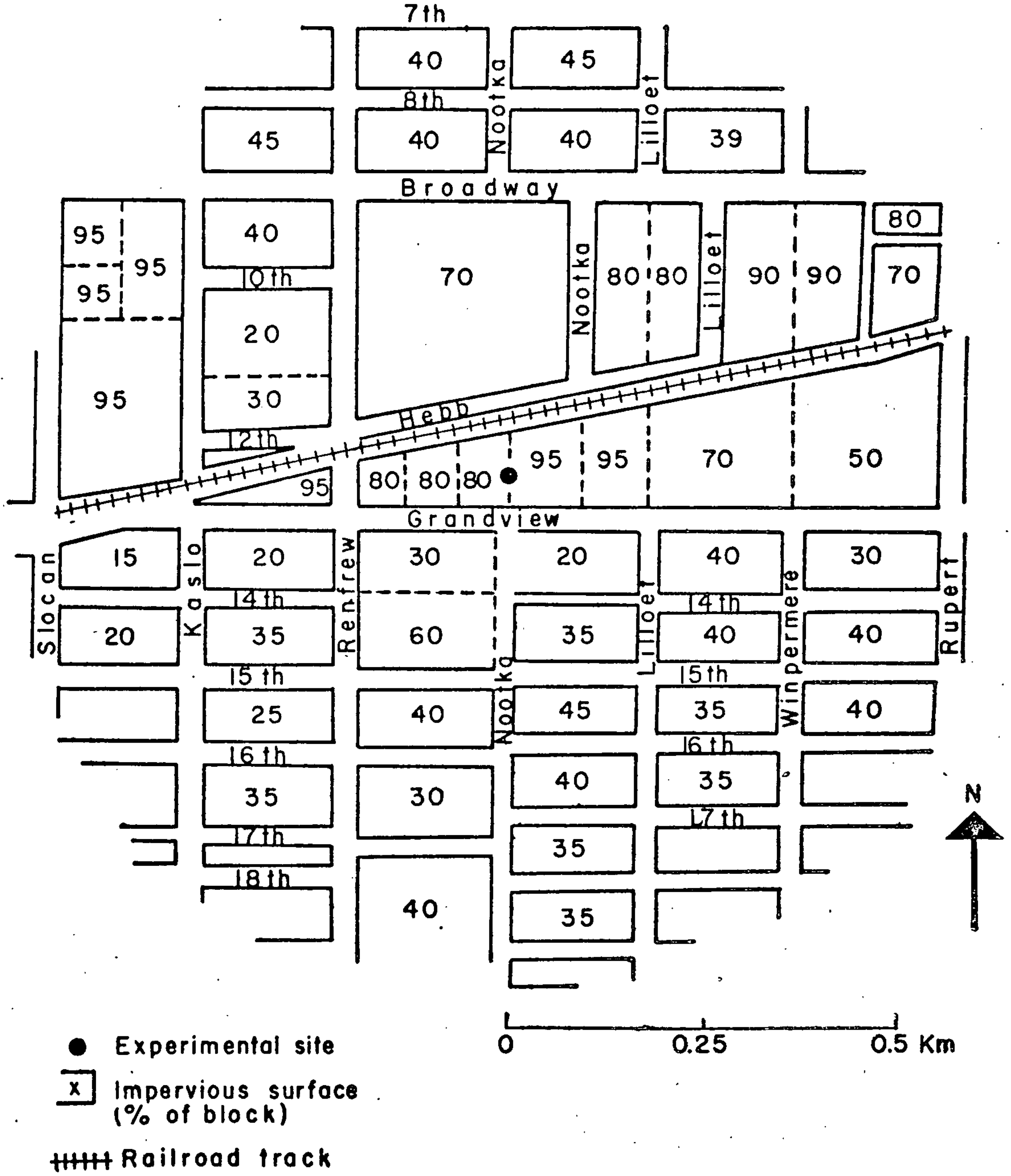

Fig. 2.3 Site plan of the experimental area.

the area is mainly residential. In the immediate surroundings most buildings were 7-8 m in height.

The canyon itself (Figure 2.4) is aligned north/south and is located between two large food packing and storage plants. They do not represent significant sources for anthropogenic heat (Q_F). The canyon dimensions are approximately 8 m in width, 6 m in height, and 79 m in length. The two walls were, however, of different heights [see Figure 2.5(a)], and this may be expected to cause results to depart in magnitude somewhat from those in a symmetrical canyon, but should not significantly affect the nature of the processes. Here it will be assumed that the results are the same as those occurring in a canyon with equal sides, but the magnitude of the expected differences will be discussed. The canyon walls are concrete, covered with several coats of flat, white paint. They are smooth except for some narrow structural columns (9 cm x 60 cm) which occur every 3 m along the east wall, and extend to within 50 cm of the top of the wall [Figure 2.5(a)]. The canyon floor consists of a 3 to 5 cm layer of gravel chips on a clay base. Unlike the walls therefore it does not strictly conform to criterion (g), and this was accounted for in the instrumental design. The roofs of both buildings are gravel-over-tar. There are some small areas of grass to the south, and bare ground and bushes to the north of the canyon buildings (Figure 2.4). Approximately 80-95 per cent of the horizontal area occupied by the two plants is covered by impervious surfaces.

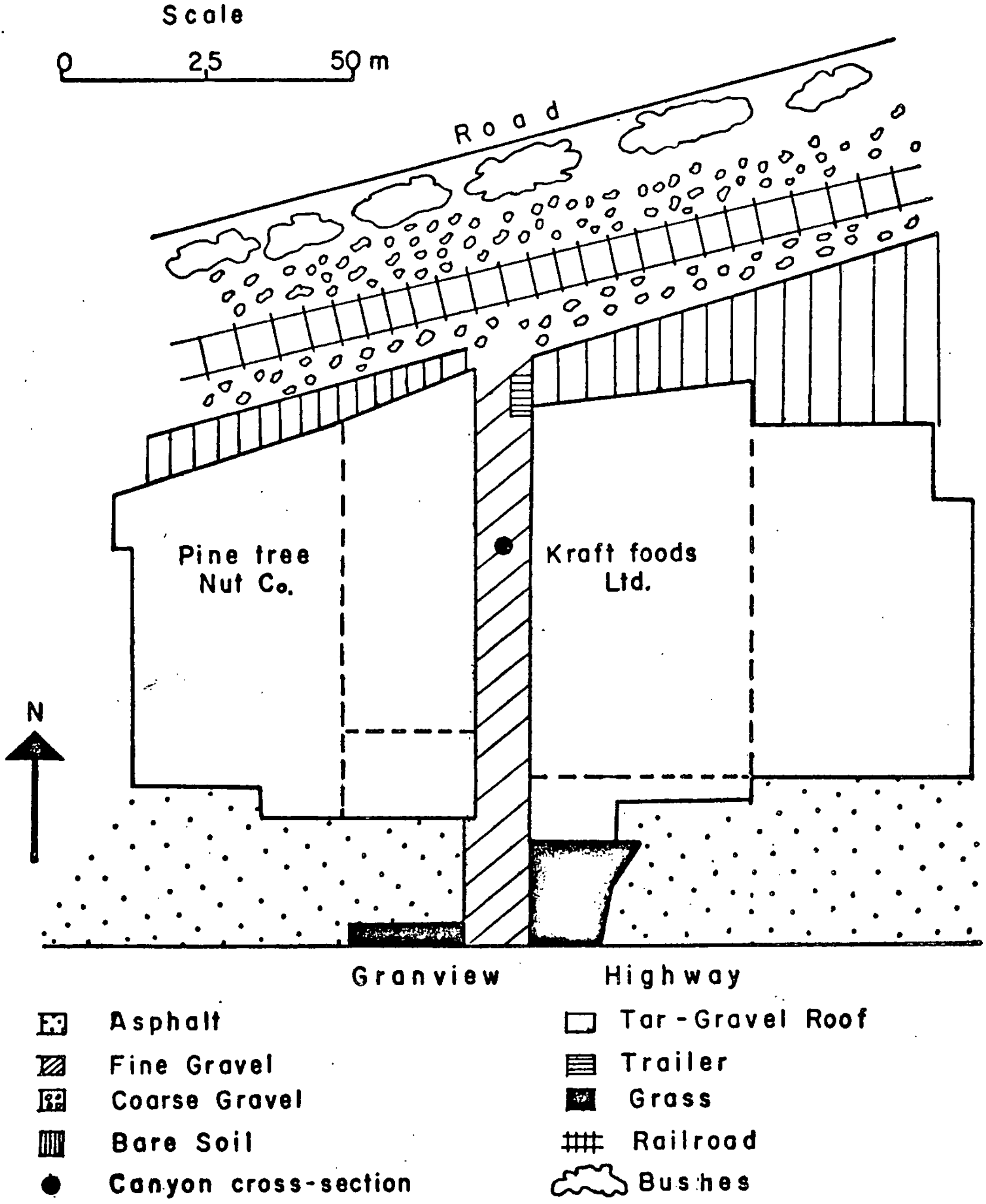

Fig. 2.4 Surface land use in the immediate canyon surroundings.

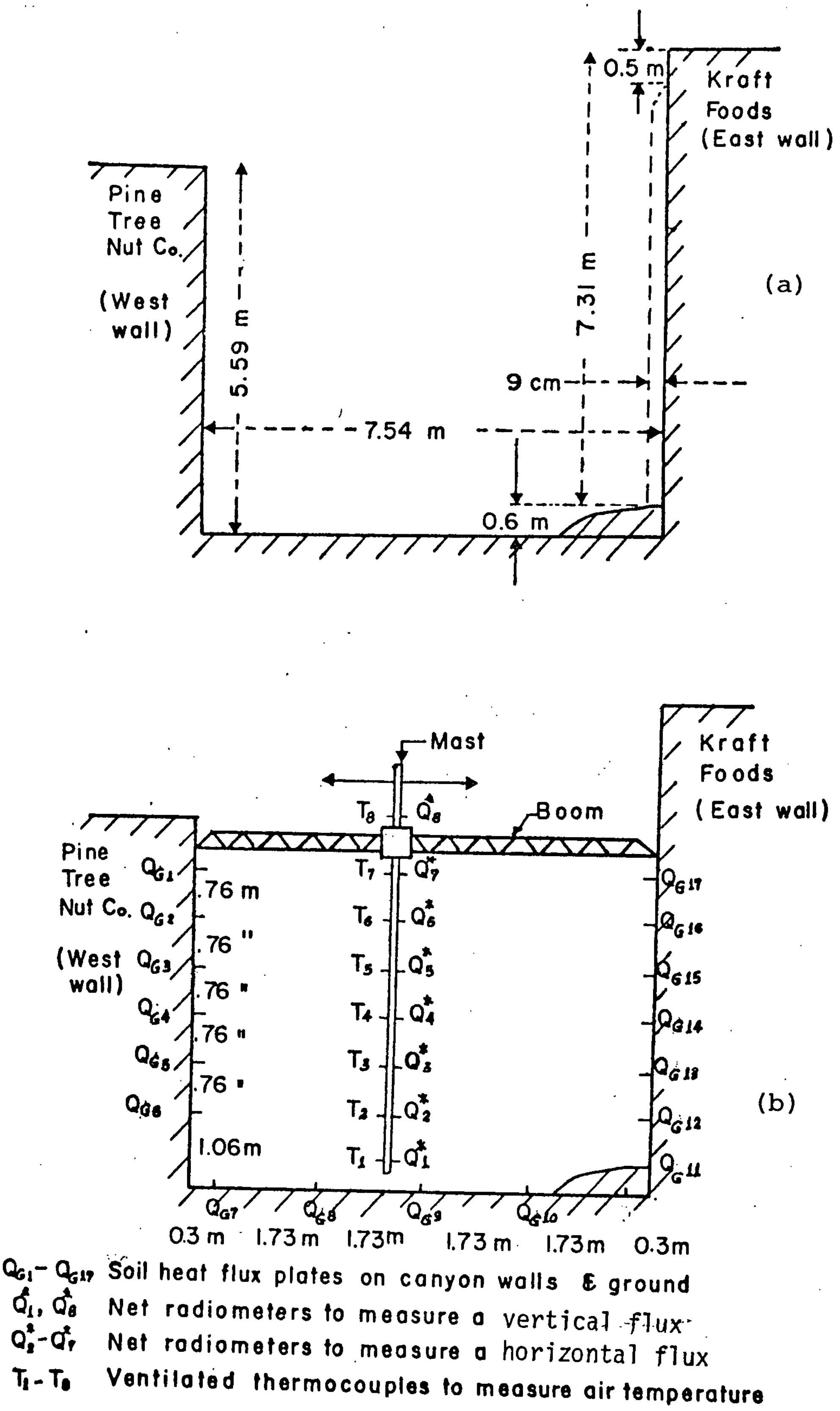

Fig. 2.5 Canyon cross-section:
(a) Dimensions
(b) Experimental Arrangement

There are ventilation ports on the roofs of both buildings, and a ventilator outlet on the south end of the east wall. None of these is anticipated to provide significant thermal effects in the canyon-air volume. Two superstructures on the west building did, however, cast shadows on the east wall during the late afternoon (1430-1700 PST) giving a disturbed shadow outline. Data during this period were omitted from analyses (see Chapter 3).

B. INSTRUMENTATION

1. Solar Radiation

Two types of pyranometers were used in the experimental work. For collecting data on a continuous basis a Kipp and Zonen solarimeter was used. This pyranometer is of the Moll-Gorczynski type, consisting of 14 constantan-manganin thermocouples joined in series to a blackened surface, and this is referenced to the body temperature of the instrument. The sensing surface is covered with two concentric hemispheric glass domes 2 mm thick designed to reduce the transfer of heat by convection between the sensitive surface and the outer dome. The glass domes have an effective wave length transparency in the range 0.3 to 2.0 microns. The instrument is fitted with a dessicant-filled cartridge which prevents moisture build-up in the instrument interior. The approximate output of the instrument is 1 mv for an incoming solar radiation of 93 W m^{-2}. The response-time of the instrument (represented by ninety-eight per cent of complete response to a step change) is achieved in 30 s. All pyranometers were calibrated at the Canadian National Radiation Laboratory.

Where spot readings were desired, the Kipp solarimeter proved impractical because of its bulkiness and weight (4.5 kg), and dome solarimeters (Lintronic Ltd., U.K.) were employed. These solarimeters are relatively light (80 g) and construction details are described by Monteith (1959). They consist of an eight-junction thermopile enclosed by a frosted glass dome, with an effective transparency range of 0.3 to 3.3 microns. The nominal calibration of the instrument is 1 mv for an incoming solar radiation of 28 W m^{-2}.

2. Net All-wave Radiation

Net radiometers used were of the Funk type (Model Sl, Swissteco Pty. Ltd., Australia). The thermopile consists of copper-plated constantan wires joined in-series between the upper and lower sensing elements. The domes are transparent to radiation with wavelengths in the range 0.3 to 100 microns, and thus the instrument is sensitive to both short-wave and long-wave radiation. In certain cases this presents a problem, since the calibration constant of the instrument might be different for short-wave and long-wave radiation. To minimize the difference it is customary to paint thin white strips across the blackened surface so as to increase the solar reflectance without changing the long-wave absorptivity. Because of this technique, the difference between the short and long-wave calibrations for all the instruments employed was $\leq$ 1.5 per cent. During the daytime, the calibration constants for short- and long-wave radiation were averaged and the resultant value applied to the data. The long-wave calibration was used for all night-time data. All net radiometers were calibrated at the Canadian National Radiation Laboratory. A typical calibration gives 1 mv for a net radiation flux of 28 W m^{-2}. The time constant of the instrument is 23 s.

The thin polyethylene domes were kept inflated by dry air pumped into the instrument. The air was dried by forcing it with a 4W 115V aquarium pump through an acrylic tube filled with silica gel. The radiometers are fitted with small port-holes concentric with the domes to allow ventilation of the outer part of the domes and thus prevent dew formation at night. This feature was not used in this study since it was noticed that no dew formed either on the instruments, or in the canyon during the night.

3. Air Temperature

The air temperature element used in this study was a copper-constantan thermocouple [Ceramocouple, Thermo-Electric (Canada) Ltd.] with a time constant of 0.25 s. These sensors are matched pairs of ISA T calibration, 24 AWG conductors, sealed in a 0.315 cm O.D. stainless steel sheath, and insulated with magnesium oxide. The sensor was housed in a 13 cm long shield made from polyvinyl chloride (PVC) tubing with an I.D.

of 3 cm. The outer walls of the tube were covered with aluminized Mylar to prevent radiation heating. Air was aspirated through the PVC tube by means of a 7W 115V fan. A 60 cm cross-arm of PVC tubing connected the fan to the thermocouple housing (Figure 2.7). The thermocouple reference temperature is incorporated into the data acquisition system (Section C).

4. Heat Storage

Soil heat flux plates (Science Associates Inc.) were used to measure the flow of heat into, and out of, the canyon surfaces. The sensor is a disc that measures 1.3 cm in diameter, and 1 mm in thickness. The upper and lower faces have a copper screen coating, and the filling material is a tellurium-silver alloy. A signal is generated by a thermopile which has alternate junctions on each metallic surface. The heat flow through the instrument (Q_G) is given by the conductivity of the instrument (k) multiplied by the temperature gradient across the faces ($\Delta T/\Delta z$).

$$Q_G = -k(\Delta T/\Delta z) \tag{2.1}$$

The plate output was typically about 0.1 mv for a heat flux of 120 W m^{-2}.

The measurement of canyon wall and floor heat fluxes is of central importance in this study, therefore considerable effort was spent in testing this instrument. The test results are given in the sub-surface heat flux chapter (Chapter 5).

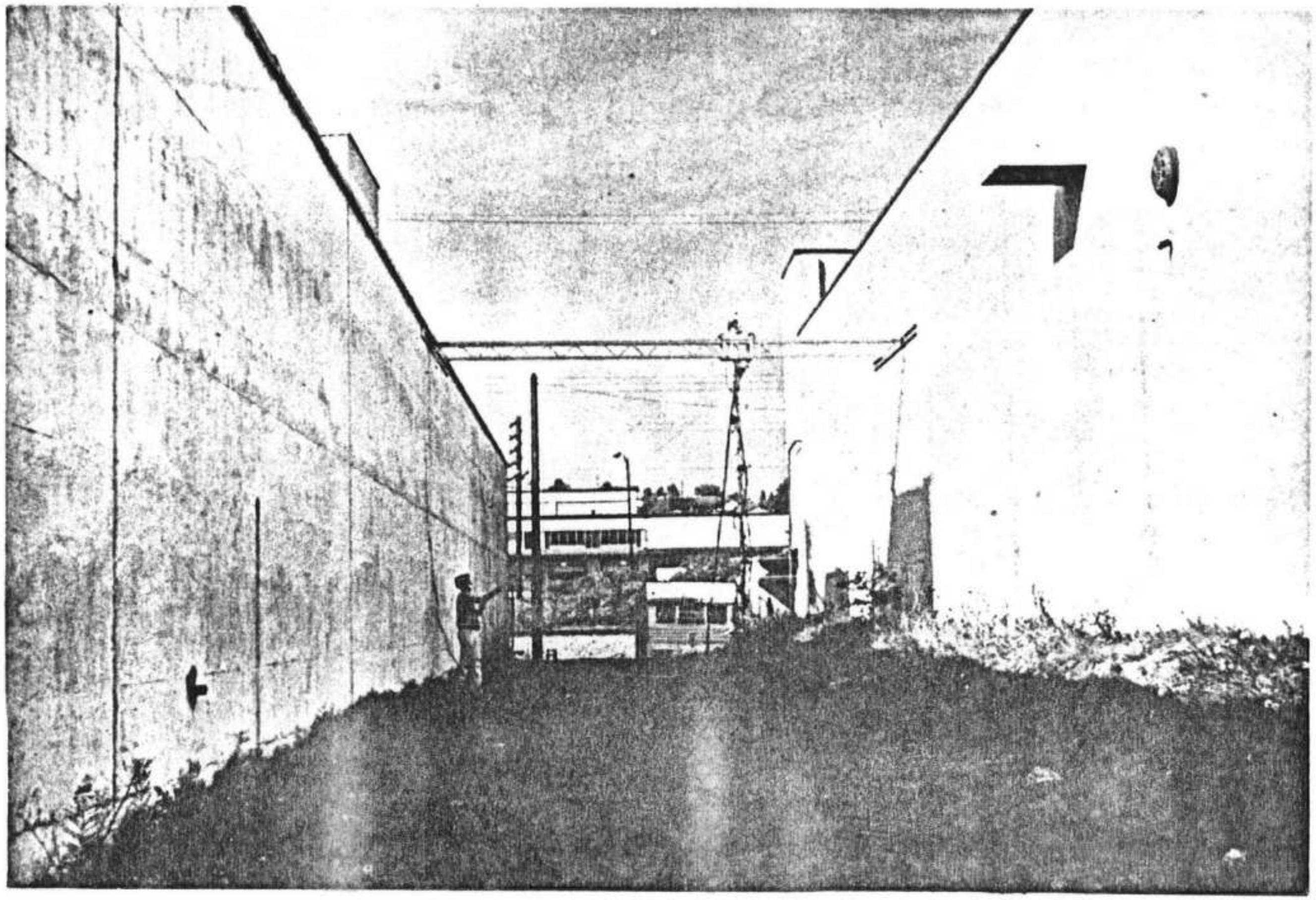

Fig. 2.6 Canyon cross-section viewed from the south end in the early afternoon. Note the boom and the mast arrangement being traversed, also the superstructure shadow on the east wall.

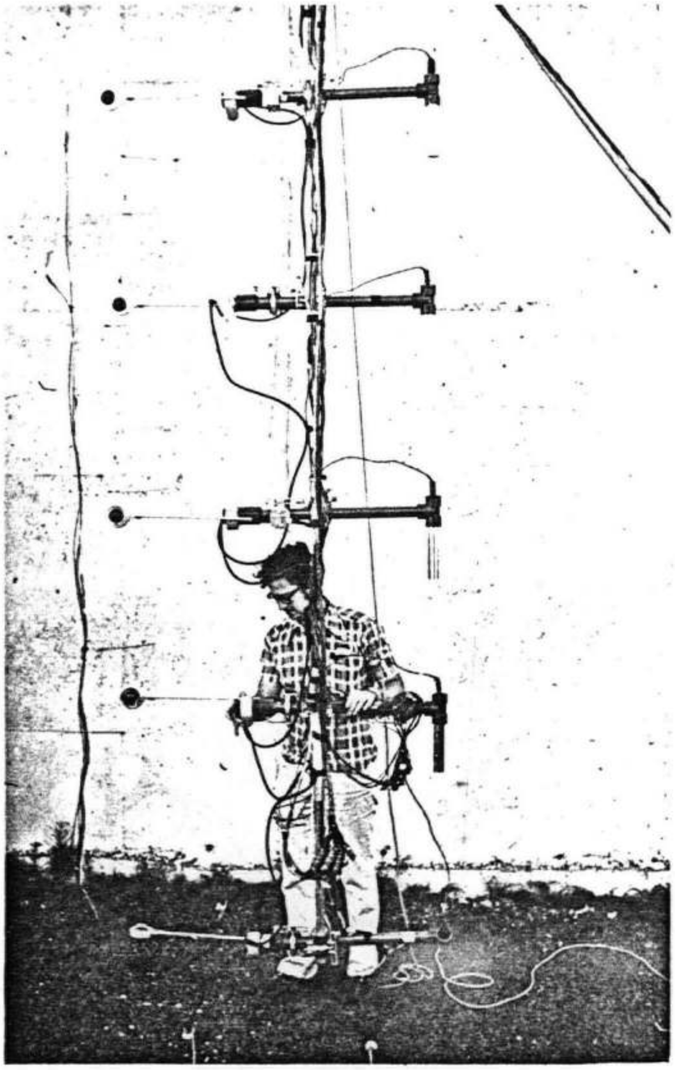

Fig. 2.7 The temperature and radiation mast and also the location of the heat flux plates on the wall. Note the difference in orientation of the lowest radiometer compared to the others.

5. Experimental Arrangement in the Canyon

Most of the experimental work was conducted at a canyon cross-section which was located 35 m from the north end of the canyon (Figure 2.4). At this position an aluminum boom was constructed across the canyon top [Figures 2.5(b) and 2.6). The boom formed a rigid trackway for a carriage with wheels which could be moved to any position across the canyon. A vertical mast was attached to the carriage, and it supported cross-arms at eight levels spaced at 0.76 m intervals upwards from the ground [Figure 2.5(b), 2.6 and 2.7]. To sample the cross-section the mast was moved to five positions across the canyon width [Figure 2.5(b)]. Thus, with instruments mounted on the cross-arms, one traverse across the canyon yielded a 5 x 8 matrix of data points.

The net radiometers and air temperature sensors were mounted on the eight cross-arms (Figure 2.7). The lowest, and highest radiometers were mounted in the usual horizontal position so as to measure the net radiant flux on a horizontal surface. The remaining six were arranged with their sensing elements parallel to the vertical walls, measuring the net radiant flux on a vertical surface. Thus following a traverse it was possible to determine the net radiant flow across the perimeter of the cross-section. The air temperature sensor shields faced downwards to minimize radiation errors.

Seventeen heat flux plates were embedded in the walls and floor of the canyon cross-section; six in each wall, and five across the floor [Figure 2.5(b)]. Holes 1 cm deep, and 1.5 cm in diameter, were drilled in the walls. The hole was filled to 0.5 cm with wet concrete, the plate installed, and the hole filled so as to be flush with the wall surface. After drying the area was sprayed lightly with white paint. The floor plates were installed 5 cm deep in the gravel (to avoid direct receipt of solar radiation), and at distances of 0.3, 1.8, 3.6, 5.5 and 7.3 m from the east wall. During one measurement phase each individual plate was monitored separately, but during the main energy balance runs the plates from each of the three component canyon surfaces (east wall, west wall and floor) were joined in-series. An additional heat flux plate was embedded at a depth of 0.5 cm in the tar-over-gravel roof of the west building.

The preceding instruments and experimental arrangement represent the main measurement array. On occasion, different instruments, or arrangements were employed. Where this occurred, it is mentioned within the results sections which follow in Chapters 3 to 6.

C. DATA ACQUISITION

A trailer (2.4 x 2.4 x 6.2 m) was located at the north end of the canyon (Figure 2.4) and housed all data acquisition equipment. The cables for the radiation and heat flux signals were 18 gauge copper arranged in 9 conductor pairs. Each pair and its drain wire were shielded with polyester, and a chrome-vinyl jacket provided overall protection. The temperature signals were carried by 20 gauge copper-constantan extension cable, shielded with aluminized mylar, and covered with vinyl.

The 8 temperature, 8 radiation and 4 soil heat flux plate signals were monitored on a data logging system (Digitrend 210, Doric Scientific). It is capable of accepting ten signals of range 0-10 mv, ten of range 0-100 mv, and 20 copper-constantan thermocouple outputs. The signals are measured using a dual-slope integration method. A reference temperature of 0°C for the copper-constantan thermocouples is an integral part of the system. A constant voltage check on the accuracy and reliability of the data logging system is also built-in. A high precision option was installed which allowed measurements to a temperature resolution of 0.1°C, and an accuracy of 1 μV. Absolute temperatures could be obtained to within ±0.3°C.

During the main part of the data collection, all channels from each location were monitored every three minutes during the day, and the data printed on paper tape. The data was transferred to computer cards; two cards representing one 3 min scanning sequence. During nighttime measurements the data from each location was monitored once every six minutes. All data were subsequently reduced to hourly averages.

D. OBSERVATION PERIOD

As mentioned previously, the study is confined to cloudless sky, light wind conditions, and in Vancouver this is consistently achieved only in the summer. The observation period was between May and October, 1973, and the daily sequence of some weather elements for this period is given in Figure 2.8. Temperatures were cooler than normal (except for September), but rainfall was substantially less than normal throughout. The schedule of field activities is given in Table 2.1.

TABLE 2.1

SCHEDULE OF FIELD ACTIVITIES IN 1973

PERIOD	ACTIVITY
April 29 - June 28	Calibration of soil heat flux plates at University of B.C.
July 9 - July 14	Canyon advection
July 16 - July 20	Net radiation flux divergence along canyon axis
July 26 - August 1	Canyon subsurface heat flux
August 8 - August 14	Canyon solar radiation
September 1 - October 12	Canyon energy balance

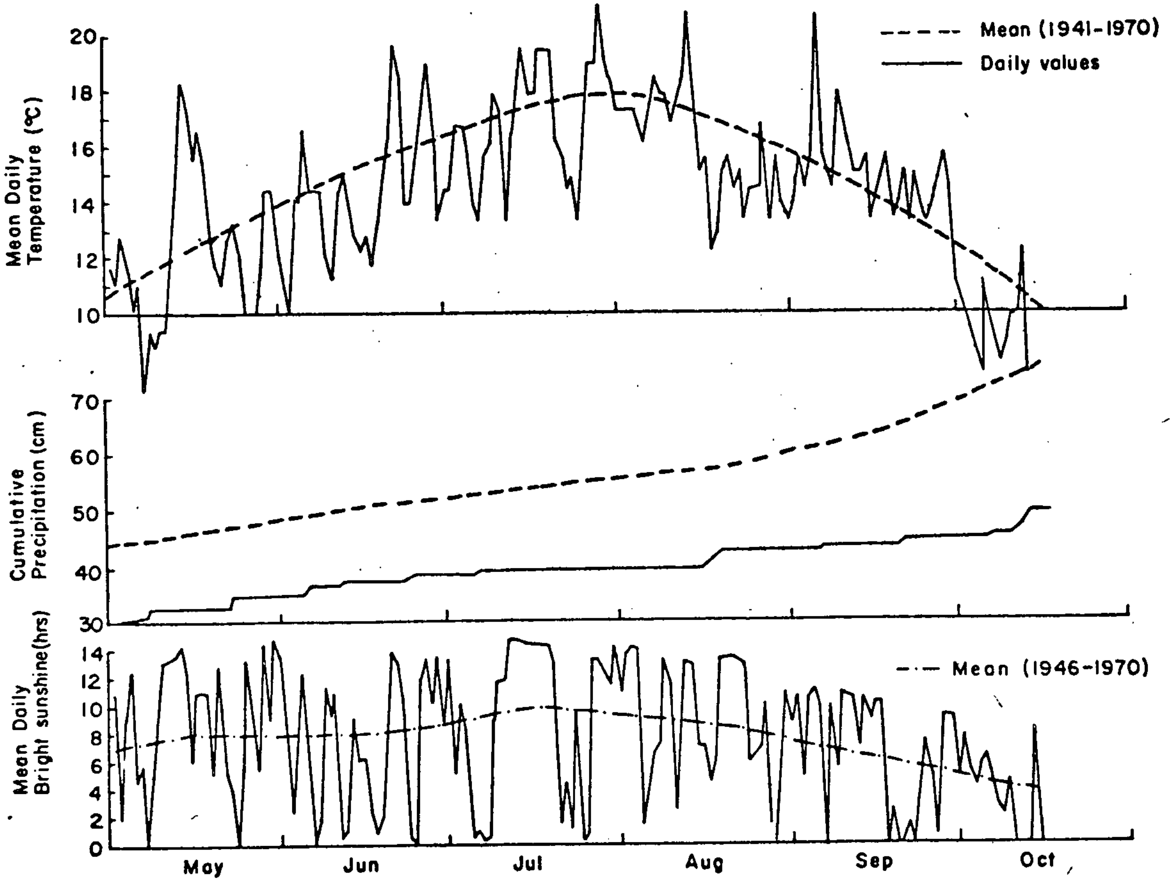

Fig. 2.8 Climatological trends for May-October, 1973, Vancouver International Airport

CHAPTER 3

SOLAR RADIATION EXCHANGES IN THE CANYON

A. INTRODUCTION

1. General

Most research on solar radiation in urban areas has been concerned with the attenuation due to increased, or changed, aerosol. This study, on the other hand, considers the incoming solar radiation at roof-top level and within the structure of the urban canyon. Thus there is no attempt to analyze the modification of the solar beam during its passage through the urban atmosphere, the emphasis here is upon its receipt, reflection, absorption and transformation in the canyon environment. It is therefore viewed as the most important input forcing function in the surface energy balance of the total canyon system via its component surfaces (walls and floor).

Previous work on the role of the surface in the exchange of solar radiation at the urban surface has been restricted to only a few observational studies, and fewer modelling attempts. Observations of the solar fluxes or the surface albedo have been undertaken from aerial platforms (Kung *et al.*, 1964; Barry and Chambers, 1966); from single urban surfaces such as a roof, parking lot, etc. (Bach and Patterson, 1969; Oguntoyinbo, 1970; Fuggle, 1971); and in only one case within the urban canyon (Tuller, 1973). These studies generally refer to gross aerial estimates of surface albedo, or very limited spot values, and therefore do not contribute significantly to an understanding of the details of radiative exchange at the complex urban surface. The modelling studies (Craig and Lowry, 1972; Terjung and Louie, 1973, 1974) involve calculating solar fluxes and albedos from theoretical solar distributions and assumed surface dimensions and radiative properties. They predict a canyon system albedo which is dependent upon the zenith angle of the Sun, and increased absorption in the canyon compared to a flat surface. These results are capable of testing by observation and will be referred to later.

This chapter describes the results of solar radiation measurements in the experimental canyon (Chapter 2). It considers the time dependent input of solar radiation to the individual canyon surfaces, the albedo of the surfaces and the total system, and the resultant absorption by the total canyon system. Such information is important in understanding the role of such a three-dimensional configuration in reflecting or trapping solar radiation, and in evaluating the performance of theoretical models in the prediction of solar exchanges under non-ideal conditions. The biological and architectural value of such information should also not be overlooked.

2. Experimental Arrangement

(a) Component surface fluxes. To measure the solar radiation normal to each component canyon surface the lightweight dome solarimeters (Chapter 2) were employed. Two solarimeters (back-to-back) were attached to the end of an aluminum pole. Spot measurements of the incoming and outgoing solar fluxes were made by holding the solarimeter sensing surface parallel to and about 0.5 m above the surface being investigated. The surface albedo (α) is then defined by:

$$\alpha = \frac{K\uparrow}{K\downarrow} \qquad (3.1)$$

where K↑, K↓ = outgoing and incoming solar radiation fluxes, respectively. Observations were made at heights of 1 and 3.3 m above ground for the east and west walls, at distances of 0.6, 3.8 and 7 m from the east wall for the canyon floor. The solarimeter outputs were measured on a portable DC microvoltmeter (Comark Electronics Ltd.) once every hour.

(b) Canyon top and floor fluxes. To measure the radiation fluxes at the top of the canyon, upward and downward facing Kipp and Zonen solarimeters (Chapter 2) were mounted at a height of 5.5 m on an arm extending horizontally from the movable carriage on the cross-canyon boom. Measurements were made at distances of 0.6, 1.8, 3.8, 5.6 and 7 m from the east wall. Assuming the albedo to be constant along the length of the canyon, which seems reasonable, the integrated albedo of the canyon system averaged across the top (α_t) is given by:

$$\alpha_t = \frac{\sum_{i=1}^{5} K\uparrow_i}{\sum_{i=1}^{5} K\downarrow_i} = \frac{K\uparrow_t}{K\downarrow_t} \qquad (3.2)$$

where

$K\uparrow_i$, $K\downarrow_i$ = individual measurements of $K\uparrow$ and $K\downarrow$, at the five locations across the canyon top,

$K\uparrow_t$, $K\downarrow_t$ = outgoing and incoming solar radiation of the canyon system averaged across the canyon top.

Another solarimeter was located over the roof of the west building to continuously monitor the solar radiation reflected. The roof albedo was calculated from Equation 3.1 using $K\downarrow_i$ from the boom results. In September both $K\downarrow$ and $K\uparrow$ were measured over the roof. All signals were recorded on a potentiometric strip-chart recorder (Model 194, Honeywell).

To simplify comparisons, the data for most of the results presented in this chapter are for the same four cloudless days (August 8, 9, 13 and 14,1973).

B. SOLAR RADIATION RESULTS

1. Solar Radiation Input ($K\downarrow$) to Component Surfaces

The incoming solar radiation flux for each component surface is shown in Figure 3.1. This shows that the regime for each canyon surface is characterized by one period of strong solar irradiance. The position and magnitude of the peak input

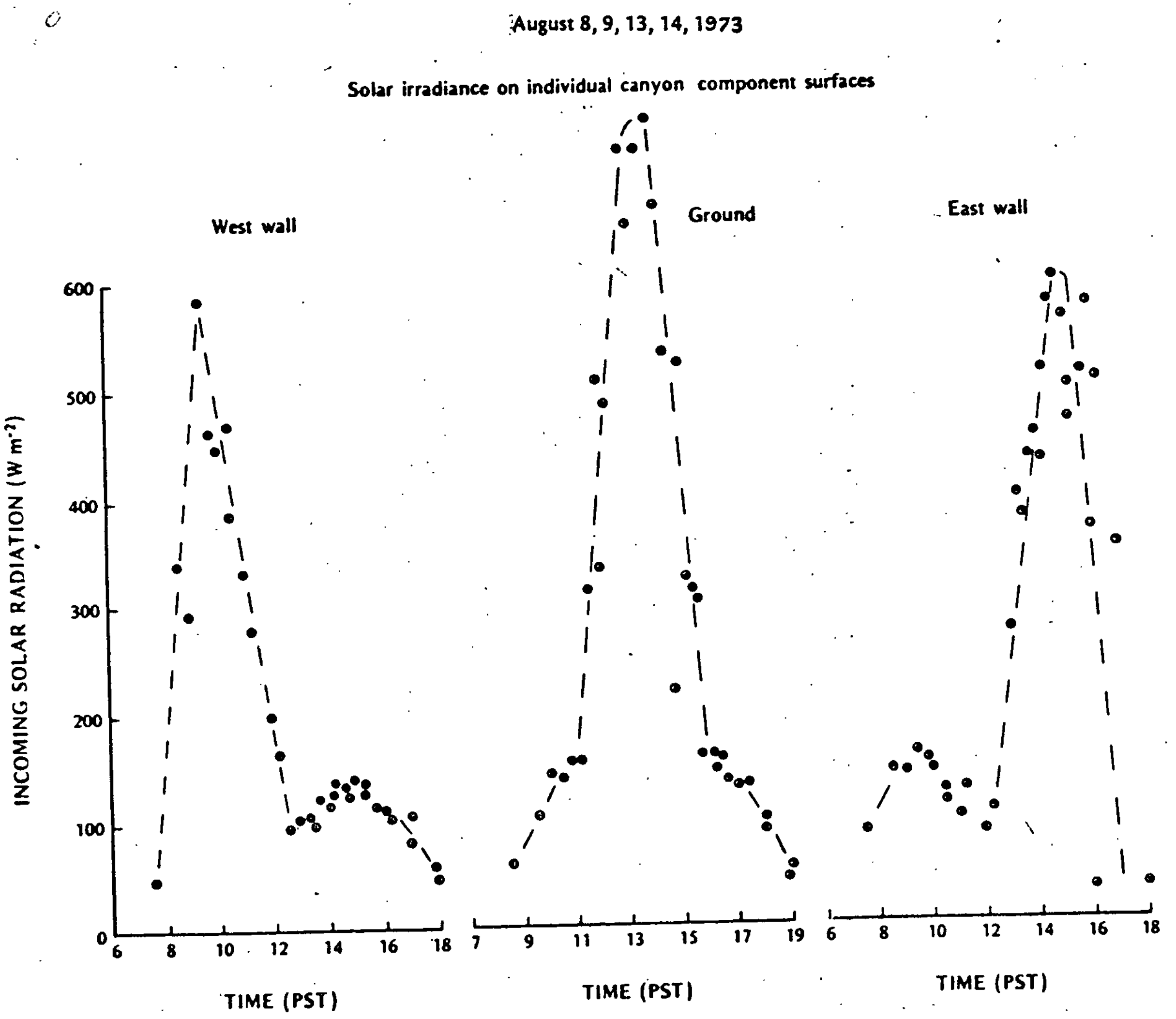

August 8, 9, 13, 14, 1973

Solar irradiance on individual canyon component surfaces

West wall

Ground

East wall

Fig. 3.1 Incoming solar radiation on the individual canyon surfaces.

for each surface is governed by the local angle of incidence of the direct solar beam for that surface orientation, and the intensity of the solar beam. Thus the maximum K↓ occurs at approximately 0930, 1330 and 1500 PST for the west wall, floor ane east wall locations respectively. The floor receives the highest input (≈750 W m^{-2}) near the time of solar noon, and the two walls receive approximately 150 W m^{-2} less at the time of their maximum receipt.

The two walls also exhibit an interesting secondary peak (1500 PST for the west wall, and 0930 PST for the east wall). These are probably a result of the increased diffuse reflection in the canyon since the timing of these secondary peaks corresponds to the times of maximum solar irradiance of the opposite wall. Note also that the effective day length for solar radiation is short for all surfaces (≈10 h) but that for approximately 4 h there is a relatively intense radiation climate. Each surface is active for a short time whilst the others are relatively passive.

The form of the solar radiation receipt for each component surface in Figure 3.1 is very basic to the energy balance of the canyon. It will be shown that the course of Q^*, Q_G and Q_H are intimately linked to the form of the solar input.

2. Albedos of the Canyon Component Surfaces and Roof.

The albedos of the component surfaces are given in Figure 3.2 as a function of the solar angle of incidence, defined relative to the individual surface's local orientation.

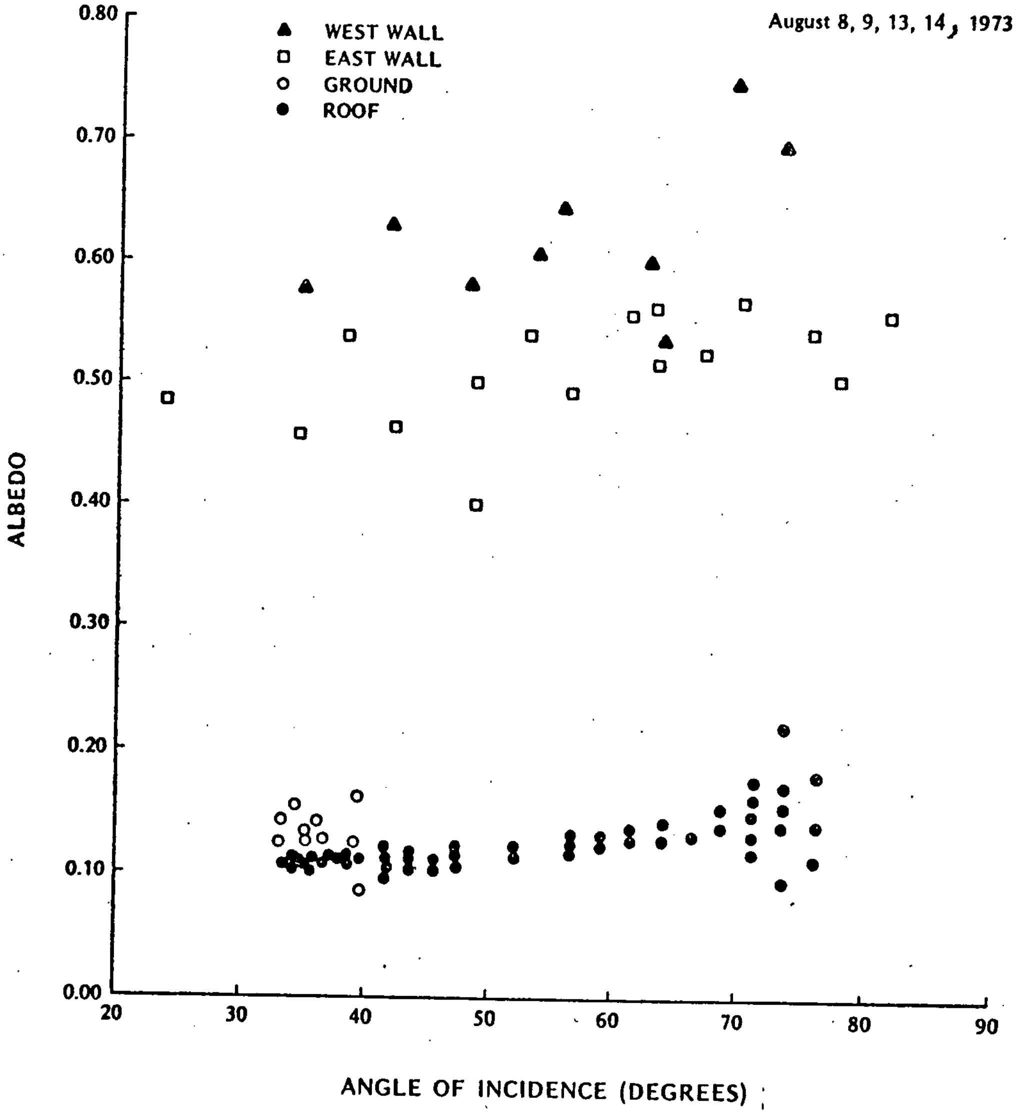

Fig. 3.2 Albedo of the individual canyon surfaces and roof.

Thus for the horizontal surfaces (ground and roof) this is synonymous with the Sun's zenith angle, but for the vertical surfaces (walls) it is a complicated function of the Sun's zenith angle and the azimuth angles of both the Sun and the surface.

The component surface albedos are grouped into two gross classes. The roof and floor albedos are generally low in comparison with most natural surfaces (0.10 - 0.20), whereas those of the walls are relatively high (0.45 - 0.75). Ignoring any dependence of the albedos on zenith angle (see below) the data in Figure 3.2 were averaged and the mean surface albedos were 0.62, 0.52, 0.13, and 0.13 for the west wall, east wall canyon floor and roof surfaces respectively. Clearly the confidence to be placed on these mean values is different for each surface.

Some natural surfaces exhibit a dependence of their albedo on the zenith angle of the Sun (e.g., for crops see Monteith and Szeicz, 1961; Davies and Buttimor, 1969; Nkemdirim, 1972; for water see Nunez *et al.*, 1972), but there is little information for building materials. Craig and Lowry (1972) assumed such a dependence for the materials in their theoretical canyon albedo model and therefore it is interesting to see if the data here confirm this.

The results in Figure 3.2 do not clearly demonstrate that the surface albedos are dependent on zenith angle. Visually, there is some suggestion of the wall and roof albedos slightly increasing at greater local zenith angles, but statistically these trends proved to possess little significance. The small range of canyon floor zenith angles allows little interpretation to be made. In summary therefore the data do not allow firm conclusions to be drawn. This is in part probably due to the spot measurement technique adopted. In the absence of this information it will be assumed that there is no zenith angle dependence, and the mean albedos will be used in calculations.

3. Albedo of the Canyon System

Although the component surface albedos do not show an obvious solar angle (or time) dependence, the albedo of the canyon system, α_t (as calculated from Equation 3.2) does show a marked variation (Figure 3.3). The variation shows α_t to peak at 0930 and 1500 PST, and to be a minimum at 1230 PST. The diurnal range being approximately 0.18.

The time-dependent changes of α_t are easily explained in terms of the roles of the component surfaces already discussed. The system albedo peaks correspond exactly with those of the two walls. Some of the diffuse reflection from the high albedo walls, at these times of their maximum irradiance, will be lost to the atmosphere thus increasing α_t. The time of minimum α_t corresponds to maximum irradiance of the floor whose albedo is the lowest of all the canyon component surfaces. By contrast the albedo of the essentially horizontal roof is also included in Figure 3.3 (sha-

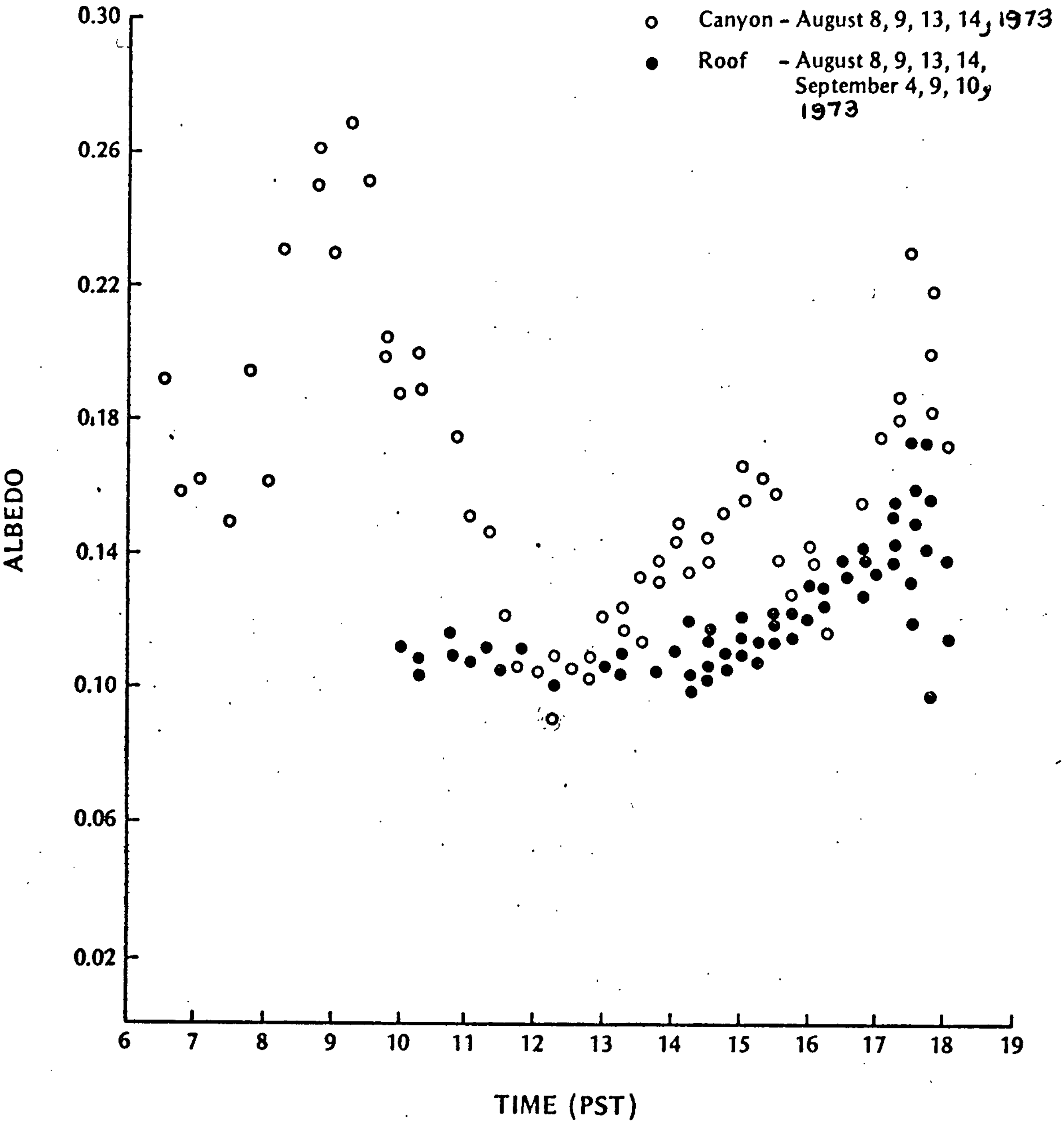

Fig. 3.3 Albedo of the canyon system and the roof. Open circles refer to mean fluxes measured across the canyon top.

dows prior to 1000 PST precluded early morning results) and suggests a much more regular diurnal pattern.

Explanation of the different magnitudes of the two α_t peaks is less simple, but the following three explanations are suggested. Firstly, the higher morning peak compared to that in the afternoon must in part be due to the higher albedo of the west wall (see Figure 3.2). Secondly, the complication of super-structure shadows in the afternoon on the east wall may reduce its reflectivity, but this should only decrease the value of α_t by a small amount (≈ 0.01). Thirdly,the differences in height between the two walls (Chapter 2) will result in asymmetry in $K{\downarrow}_t$ between the morning and afternoon. This will decrease the input of direct beam and diffuse sky radiation in the morning, and increase the diffuse in the afternoon due to the reflection into the canyon from the portion of the east wall which is above the theoretically defined canyon-top (i.e., above the boom). It is possible that the morning/afternoon change in the ratio of direct to diffuse beam solar radiation has an effect on the system albedo. The asymmetry of $K{\downarrow}_t$ is illustrated in Figure 3.4, where measured $K{\downarrow}_t$ is compared to the theoretical $K{\downarrow}_t$ obtained from the Houghton (1954) model as used by Nunez *et al.* (1971). Note, however, that because of the asymmetric α_t distribution the measured $K{\uparrow}_t$ does appear to be roughly symmetric about solar noon ($\sim$1200 PST).

The time-dependence of α_t implies that aerial sur-

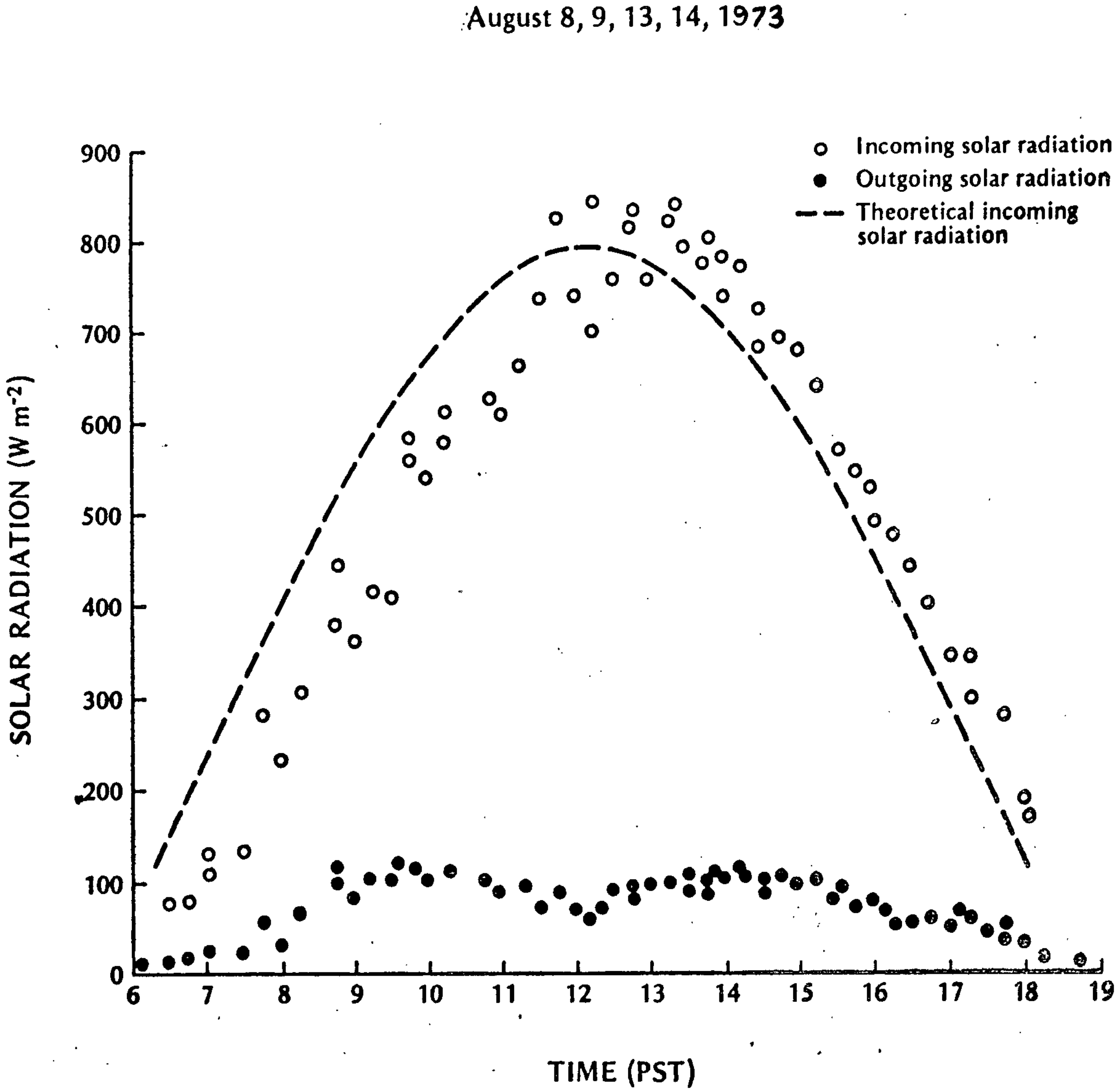

Fig. 3.4 Solar radiation fluxes averaged across the canyon cross-section.

veys of urban albedo must integrate their results over time as well as space. Equally it will be important to ascertain the roles of street orientation, and geometry.

4. Absorption by the Canyon System

The role of geometry in trapping solar radiation can be isolated by comparing the absorptivity of the canyon system $(1 - \alpha_t)$, with that of an equivalent horizontal area with the same percentage composition of surface albedos (i.e., this is equivalent to removing the canyon geometry by laying the walls flat but maintaining the areas and albedos of the component surfaces). Using the mean albedos of the floor and walls, and the canyon dimensions, we can define the albedo of an equivalent horizontal area $(\bar{\alpha})$ by:

$$\bar{\alpha} = \frac{0.13\ W + 0.52\ H + 0.62\ H}{2H + W} \qquad (3.3)$$

Since all the quantities are constant for the canyon $\bar{\alpha}$ is constant and equal to 0.393 for the experimental canyon, giving $(1 - \bar{\alpha}) = 0.607$. The factor which defines the relative trapping efficiency of the canyon geometry is the ratio of absorptivities (R) given by:

$$R = \frac{(1 - \alpha_t)}{(1 - \bar{\alpha})} \qquad (3.4)$$

Figure 3.5 shows how R varies with the zenith angle of the Sun. Clearly the geometry increases the absorption

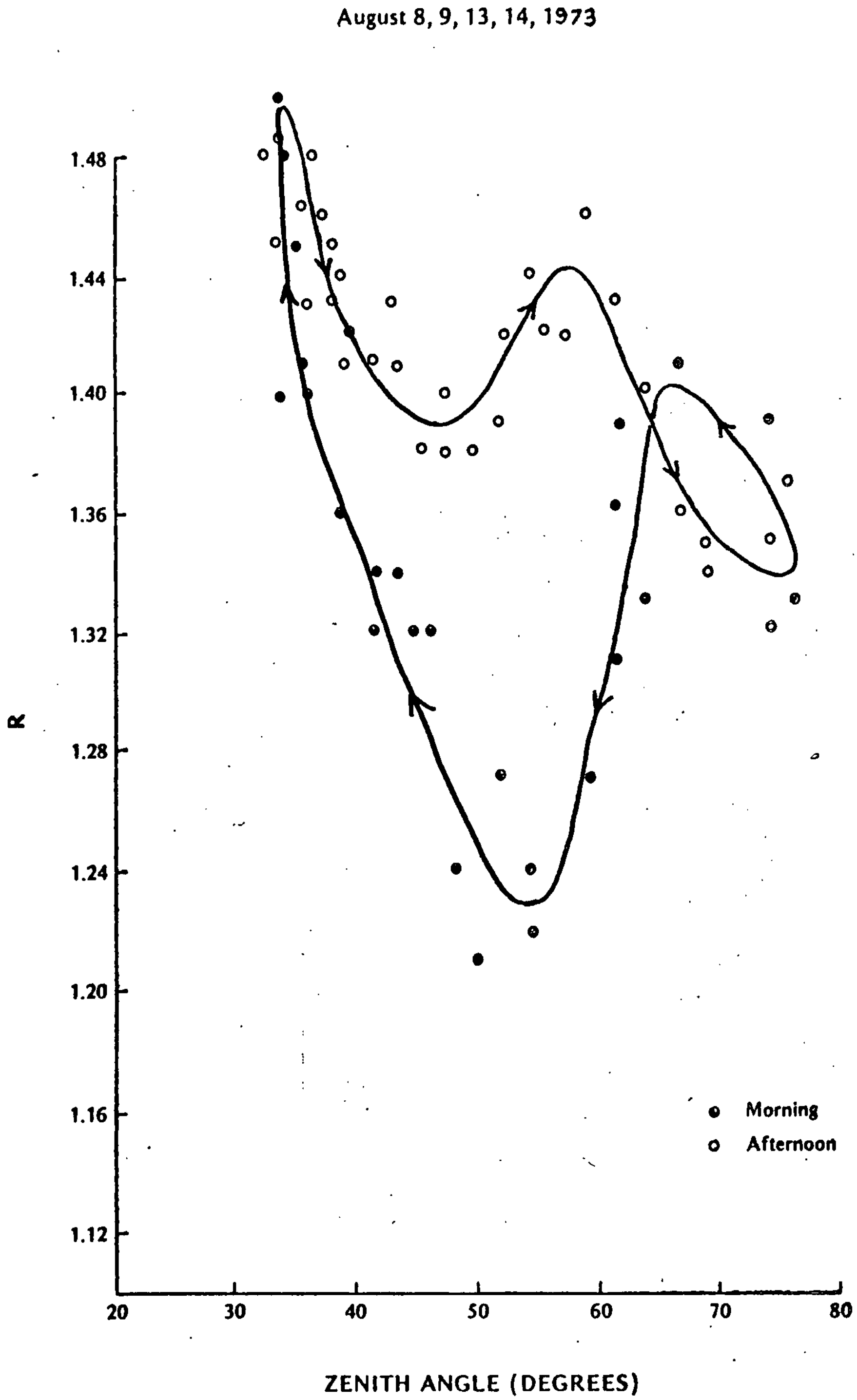

Fig. 3.5 Ratio of absorbed solar radiation in canyon system to an equivalent horizontal area vs. zenith angle.

efficiency by a minimum of 20 per cent to a maximum of 50 per cent at solar noon. The un-weighted mean daily value of R is 1.36, indicating that this canyon is about a third more efficient in trapping solar radiation than an equivalent horizontal surface.

The behaviour of R with zenith angle was considered by Terjung and Louie (1973) for the case of theoretical canyons having different height to width ratios, and a uniform albedo for all component surfaces. Their calculations show an increase in R with a decrease in zenith angle. The experimental results show a much more complex pattern which is attributable to the changing roles of the component surfaces and roof with time, and their very different albedos.

Finally, in this chapter we consider whether the two sets of experimental data (individual surface fluxes, and fluxes across the canyon top) are consistent in accounting for the solar radiation in the system. Thus we require that all the solar radiation entering the canyon volume balance with that leaving:

$$\begin{aligned} & K{\downarrow}_t.L.W. + \alpha_e K{\downarrow}_e.L.H + \alpha_g K{\downarrow}_g.L.W. + \alpha_w K{\downarrow}_w.L.H. \\ = \; & \alpha_t K{\downarrow}_t.W.L. + K{\downarrow}_e.L.H. + K{\downarrow}_w.L.H. + K{\downarrow}_g.L.W. \end{aligned}$$

or,

$$K^*_t = (H/W)(K^*_e + K^*_w) + K^*_g \qquad (3.5)$$

where K^* = net solar radiation, and the subscripts e, w, and g refer to the east wall, west wall and ground (canyon floor) surfaces respectively.

The results of substituting the experimental results in Equation 3.5 are shown with Figure 3.6. Apart from the discrepancy between 1400 and 1600 PST the agreement is good. Ignoring the data for this period, the daily mean solar absorption from the individual surfaces was 363 W m^{-2}, and that from the canyon top was 389 W m^{-2}. This agreement to within 7% is encouraging and helps to support the choice of instrumental techniques employed. The discrepancy between 1400 and 1600 PST is probably a result of an instrumental view factor problem during this time when the east wall has super-structure shadows upon it (Figure 2.6). Thus the spot measurement solarimeter close to the wall would register a much reduced flux, but the overhead solarimeter would 'see' a much larger area (including the non-shadowed wall further down canyon) and would register a much smaller effect. The shadow will also affect the fluxes of Q^* and Q_G measured on the east wall. Thus measurements for the east wall in this period are omitted in the chapters which follow.

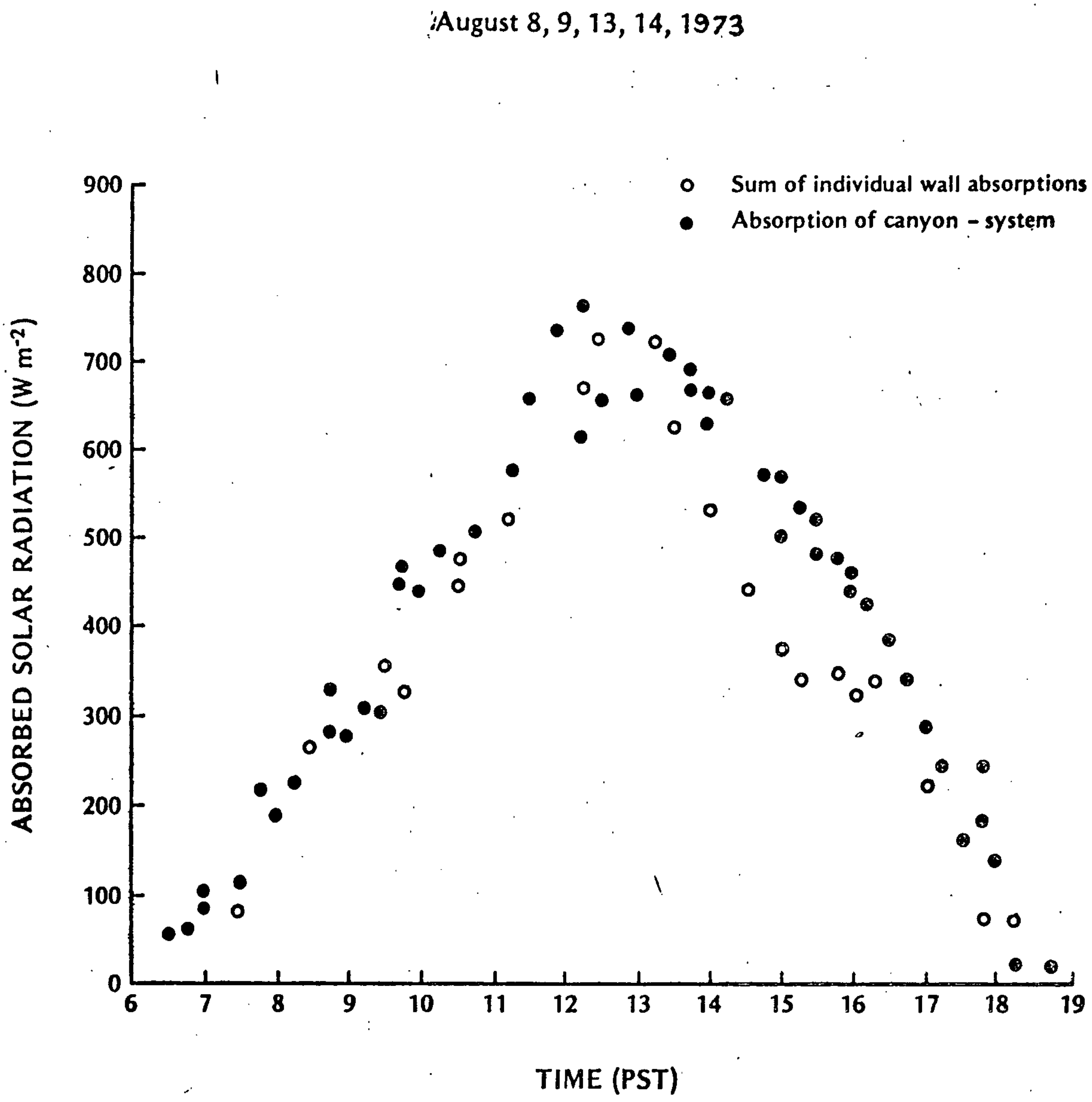

Fig. 3.6 Solar radiation absorption by the canyon.

CHAPTER 4

NET RADIATION IN THE CANYON

A. INTRODUCTION

The net all-wave radiation (Q^*) represents the effective energy source (or sink) driving the exchange of heat and water vapour between the surface and the atmosphere (Equation 1.1). The net radiation balance may be written:

$$\begin{aligned} Q^* &= K^* + L^* \\ &= K{\downarrow} - K{\uparrow} + L{\downarrow} - L{\uparrow} \qquad (4.1) \\ &= K{\downarrow}(1 - \alpha) + L{\downarrow}(1 - \alpha') - \varepsilon\sigma T_s^4 \end{aligned}$$

where

L^*, $L{\downarrow}$, $L{\uparrow}$ = net, incoming and outgoing long-wave radiation, respectively,

α' = surface reflectivity for long-wave radiation,

ε = surface emissivity,

σ = Stefan-Boltzmann constant (5.67×10^{-8} W m^{-2} K^{-4}),

T_s = surface temperature.

By day the solar radiation terms dominate in deciding the course of Q^*, and these have been described for the canyon situation in Chapter 3. In the absence of obstructions $L{\downarrow}$ is a function of the atmospheric emissivity and temperature structure, and $L{\uparrow}$

depends on the surface properties ε, α' and T_s. By night the balance is restricted to these long-wave exchanges.

There are few experimental studies of Q^* in cities. Available urban/rural daytime comparisons (Bach and Patterson, 1969, Probald, 1972) indicate that Q^* is slightly decreased in the city. By night, results (Oke and Fuggle, 1972; Rouse and McCutcheon, 1972) show the L^* loss to be slightly greater from cities because even though $L\downarrow$ is increased, $L\uparrow$ is even more enhanced.

This chapter firstly investigates the magnitude, and time and space variations of Q^* received by the component surfaces. Secondly, it considers the role of radiative flux divergence in the canyon-air volume, and thirdly, its relation to canyon cooling rates.

B. SURFACE NET RADIATION IN THE CANYON

1. Net Radiation of the Component Surface

The three-dimensional nature of the canyon dictates that Q^* for its component surfaces will be a complex function of many factors. The variability of the solar terms has been discussed, but the long-wave terms are equally complicated. In particular, the long-wave exchange will depend upon the temperature and emissivity of all media in its field of view, and for a canyon surface that will involve other canyon surfaces in addition to the sky. All points in the canyon will possess their own view factor (VF) with respect to all other radiating objects.

The form of the Q^* distributions in the canyon remained similar throughout the period of measurement and hence here we will confine analysis to the data from one day (September 10, 1973). Measurements were taken 0.3 m from each surface, these were at 1.06, 2.58 and 4.12 m above the floor for the wall data, and at three locations across the canyon for the floor data (0.30 m from each wall and in the centre).

The diurnal course of Q^* for positions on the canyon west wall are given in Figure 4.1. During the daytime the pattern is strongly related to $K\downarrow$ [Figure 3.1(a)]. As the diffuse beam input strengthens after 0530 PST the Q^* loss is decreased until the direct beam suddenly enters the canyon. At the time of maximum $K\downarrow$ at each location Q^* is also maximum. The peak input occurs at the highest location on the wall first, and with the greatest magnitude since the local angle of incidence is closest to the normal then and there. As the day progresses the local angle of incidence on the wall increases so that the magnitude of the peaks at lower levels is less, and the radiant input decreases towards noon. At approximately the time of maximum solar irradiance of the east wall [Figure 3.1(c)] there is a weak secondary peak Q^* on the west wall (Figure 4.1). The nocturnal situation is characterized by a net radiant loss at all locations. The loss is greatest at the highest levels which possess the largest sky view factor [see section B(3)]. The loss

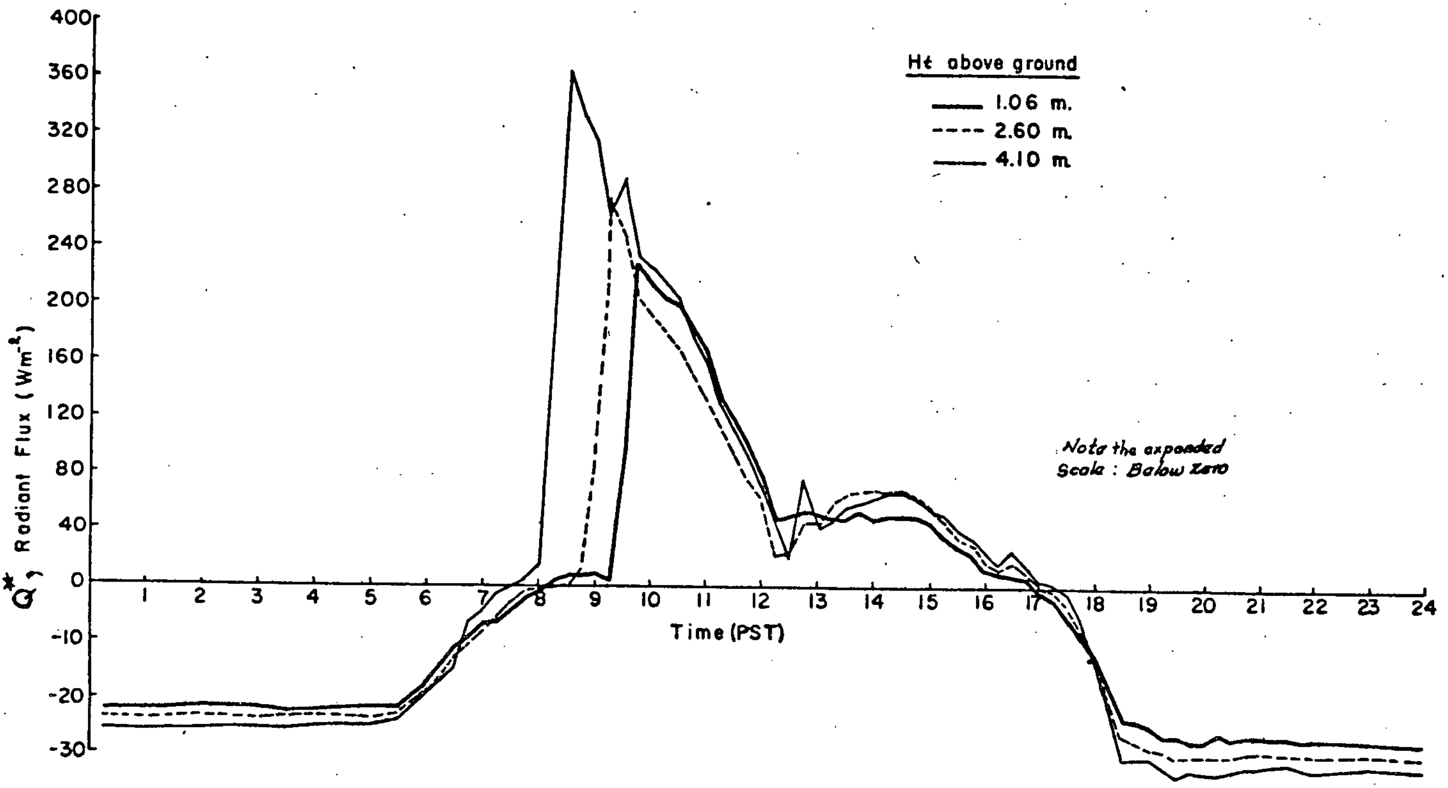

Fig. 4.1 Net all wave radiation incident on the west wall. (Q^*_W). September 10, 1973.

is greatest in the early evening when surface temperatures are at their warmest for the night.

The daytime pattern for the canyon floor is determined by its north-south orientation (Figure 4.2). As diffuse radiation fills the canyon Q^* increases slightly, but with direct irradiation (first at the west location, then at the centre and east) it rises sharply, and falls again equally sharply with the progression of the shadows. At night the relative long-wave losses at each location are in accord with their sky view factors, being greatest at the canyon centre, and least for base of the west wall [see Section B(3)].

The Q^* cycle for the east wall (Figure 4.3) is almost a mirror-image of that for the west wall, except that data are omitted at the time of the superstructure shadows in the afternoon. Note, however, that contrary to the west wall the magnitude of the Q^* peaks decreases with height. This is because in the afternoon the whole wall is irradiated by direct beam and then the shadow moves up the wall, whereas in the morning the shadow moves down the wall as deeper positions are irradiated.

For the afternoon case the topmost level on the east wall has been warmed for many hours before it receives its maximum $K\downarrow$. Thus it will have warmed-up and be emitting $L\uparrow$ more strongly, resulting in a lower Q^*.

2. Net Radiation of the Canyon System

The average net radiation over the canyon surfaces

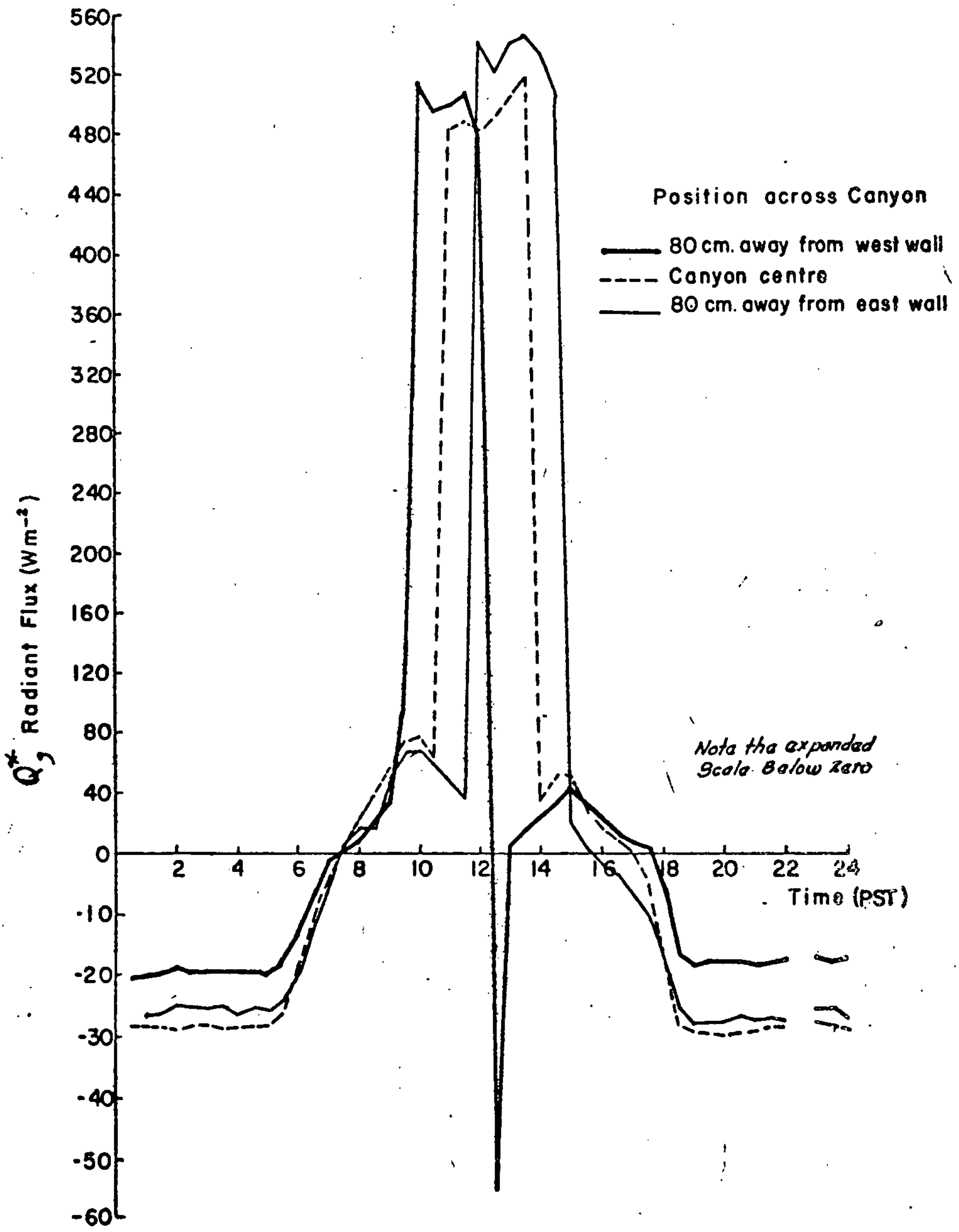

Fig. 4.2 Net all-wave radiation incident on the ground. (Q^*_g). September 10, 1973.

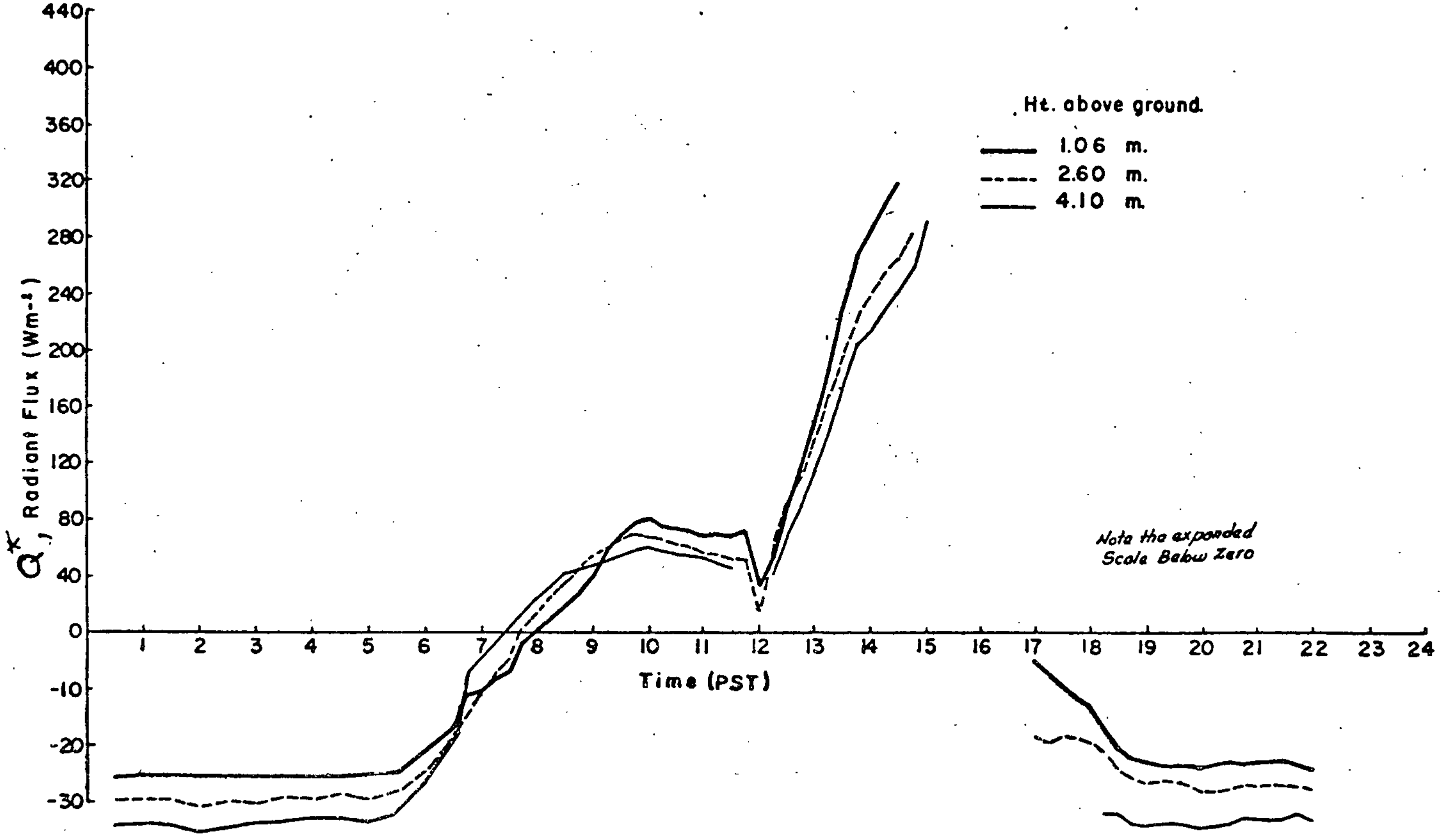

Fig. 4.3 Net all-wave radiation incident on the east wall. (Q_e^*). September 10, 1973.

($\bar{Q}^*$) is calculated using the canyon dimensions as weighting factors so that:

$$\bar{Q}^* = \frac{(Q_e^* \cdot H + Q_w^* \cdot H + Q_g^* \cdot W)L}{(2H + W)L} \tag{4.2}$$

where

Q_e^*, Q_w^*, Q_g^* = net all-wave radiation averaged over the east, west and floor surfaces of the canyon respectively,

and the dummy length L is included for clarity, thus units in the numerator are energy/unit time, and in the denominator are area. Figure 4.4 gives $\bar{Q}^*$ for the same day as Figures 4.1, 4.2 and 4.3. Note that unlike the Q^* regimes of the component surfaces, $\bar{Q}^*$ for the canyon system is a smooth bell-curve similar in form to that for an unobstructed horizontal surface.

It is important to realize that $\bar{Q}^*$ is the average *surface* value for the canyon and is not synonymous with the net radiation measured across the top of the canyon (Q_t^*), which is a spatially averaged value as seen from above the canyon. The two quantities are related:

$$Q_t^*(W.L) = \bar{Q}^*(2H + W)L + [Q^*] \tag{4.3}$$

where $[Q^*]$ = the net radiant energy storage in the canyon-air volume.

The first term on the right has units of energy/unit time, and when added to the volume storage gives the energy / unit time across

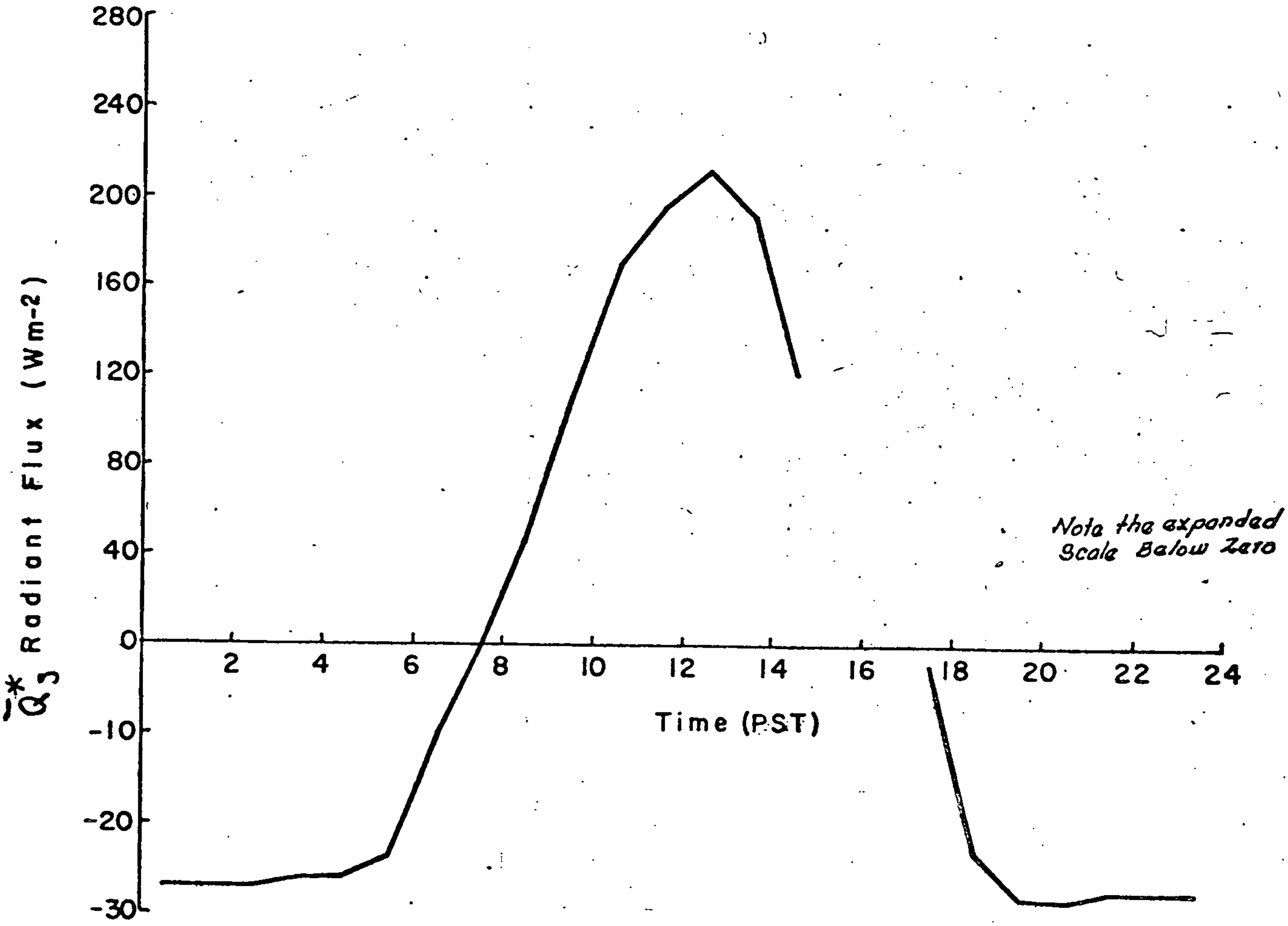

Fig. 4.4 Net all-wave radiation averaged over three ~~canyon surfaces. ($\bar{Q}$*), September 10, 1973.~~

the canyon top. If there is no storage (or divergence) in the air volume, Equation 4.3 reduces to:

$$Q_t^* = \bar{Q}^* \cdot \frac{(2H + W)}{W} \tag{4.4}$$

Thus Q_t^* and $\bar{Q}^*$ are related by a constant factor governed by the canyon dimensions.

As a first approximation in overall energy flux considerations it is probably acceptable to ignore $[Q^*]$ as in Equation 4.4. However, although small this term will be shown in Section C to be of central importance in explaining nocturnal air temperature cooling rates.

3. Net Long-wave Radiation in the Canyon at Night

The net long-wave radiation (L^*) measured anywhere in an urban area is complicated by the range of radiating surfaces which contribute to the balance at any one point. This is especially important when tall structures enter the field-of-view of a pyrradiometer at night. Under such circumstances $L\downarrow$ will be enhanced compared to an unobstructed sky because ε (and commonly T_s) are larger than for the atmosphere. The effectiveness of the night sky as a radiation sink for any location is therefore intimately connected to the sky view factor (VF_s) of that point.

The calculation of the view factor (VF) for locations in the canyon followed the method of Davies *et al.* (1970). The calculations refer to an infinitesimal surface element just above, and parallel to, a canyon surface. For a vertical wall of infinite length ($-\infty$ to $+\infty$), with the sensing element horizontal and in a place which includes the base of the wall:

$$VF = \tfrac{1}{2} \cdot \frac{\sin^2\theta' + \cos\theta' - 1}{\cos\theta'} \qquad (4.5)$$

where

θ = arctan (Y/X),

Y = wall height,

X = distance between sensing element and the base of the wall.

Equation 4.5 can be applied to obtain the sky view factor for surface elements along the two walls if we assume the walls to be of sufficient length that they approximate infinity. For a point on the east wall, at a height h above the ground Y = W and X = (H - h). For a point on the west wall the greater height of the east wall (H_e) must be considered, so that Y = W, but $X = (H_e - h)$.

Equation 4.5 does not apply to points along the ground, but the sky view factor for the ground can be obtained as the residual after calculating the view factors for the east and west walls (VF_e, VF_w) since:

$$VF_s + VF_e + VF_w = 1.0 \qquad (4.6)$$

This states that the entire field of view for a sensing element along the canyon floor is determined by the east and west walls, and the sky. This is only strictly true if the walls are of infinite length (i.e., the canyon ends do not contribute radiation to the sensing element near the ground), but will be taken as an approximation here.

Values of L^* measured at different locations near the walls, and canyon ground and across the canyon top are related to the sky view factor for each location in Figure 4.5. The data are for two nights. Two relationships appear to be evident. The first covers the results for the walls and canyon top. The relation is approximately linear, with increasing L^* at higher VF_s. The second applies to the canyon floor results which also exhibit a linear relation, with about the same slope, but displaced ≈12 W m^{-2} below the first line for the same view factor. This is explained by the fact that the canyon walls are warmer than the floor. An estimate of this difference may be made by assuming the floor relation can be extrapolated to zero view factor at which time all the radiation must come from the walls. Then:

$$L_g^* = \varepsilon\sigma(T_{w'}^4 - T_g^4) \simeq 4\varepsilon\sigma T_{w'}^3(T_{w'} - T_g) \qquad (4.7)$$

where

L_g^* = regression intercept = 3.4 W m^{-2} (Table 4.1),

ε = surface emissivity of walls and ground (assumed = 0.95),

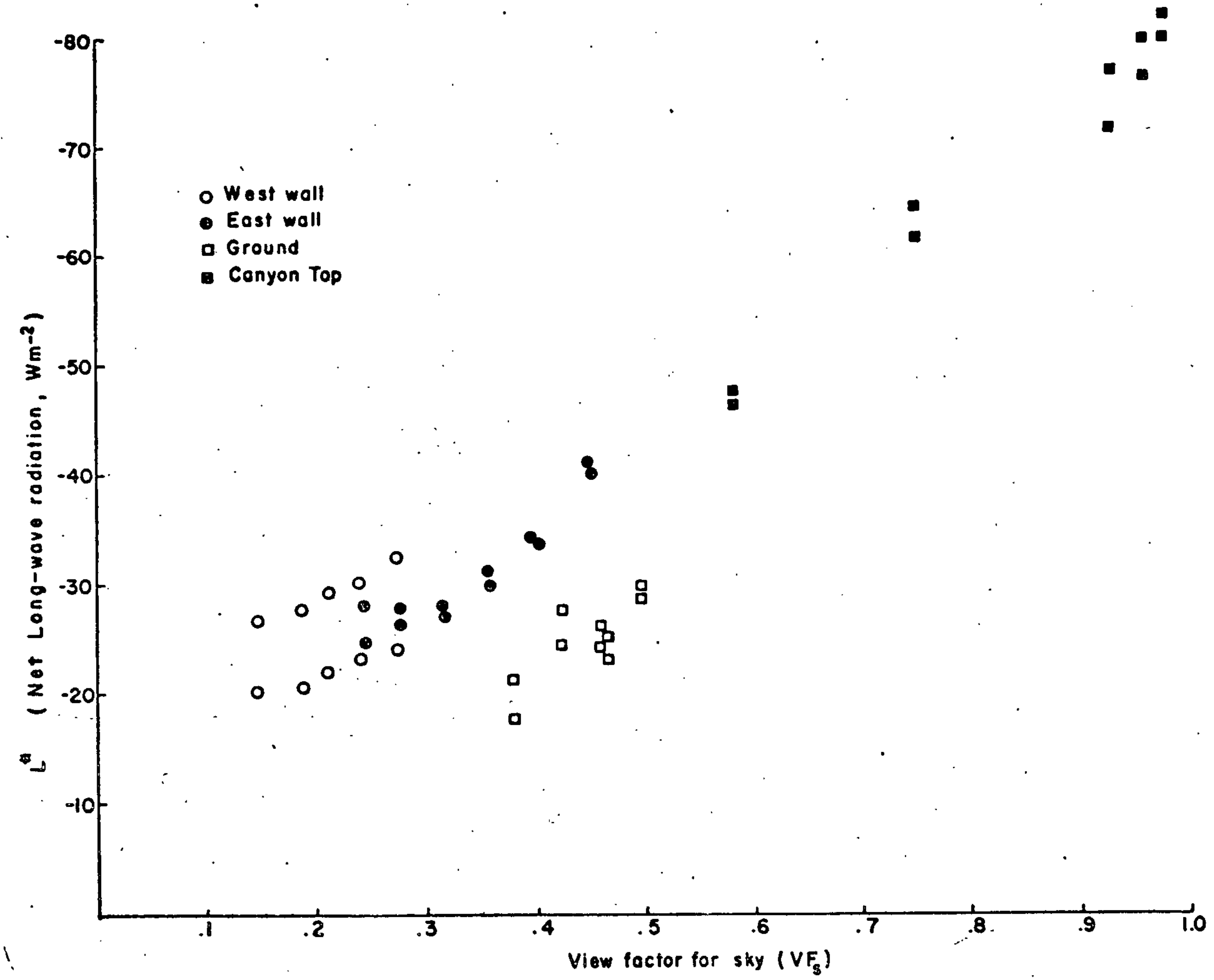

Fig. 4.5 The relationship between sky view factor (VF_s) and net long-wave radiation (L^*) at night. September 9, 10, 1973. All data collected at 2030 PST.

$T_{w'}$, T_g = mean wall and canyon floor temperatures respectively.

Assuming T_w is approximated by the mean air temperature in the canyon on these nights (289 K), the temperature difference between the walls and the floor is:

$$T_{w'} - T_g = \frac{L_g^*}{4\varepsilon\sigma T_{w'}^3} = 2.60°\text{C} \qquad (4.8)$$

Results from 0300 PST indicate that the linear relation between L^* and VF_s is maintained through the night with minor changes in slope and intercept (Table 4.1).

TABLE 4.1

RESULTS OF REGRESSION ANALYSIS BETWEEN L^* AND VF_s

($L^* = a + b.VF_s$)

DATA SET	TIME (PST)	a (W m^{-2})	b	r^2	S.E.$_{L^*}$ (W m^{-2})
ALL DATA	2030	-4.9	-71.2	-0.86	7.3
	0300	-7.2	-64.0	-0.85	6.7
ALL DATA (Less Floor)	2030	-8.8	-70.7	-0.98	3.4
	0300	-10.8	-63.5	-0.98	2.6
FLOOR ONLY	2030	3.4	-63.6	-0.61	2.3
	0300	7.9	-73.3	-0.79	1.7

It is likely that this type of relationship holds on most occasions with cloudless skies, light winds and a dry surface. This situation occurrs when the processes are largely governed by such properties as the surface thermal conductivity and the radiation geometry which remain essentially constant.

C. LONG-WAVE FLUX DIVERGENCE IN THE CANYON-AIR VOLUME

1. Introduction

Initial work in radiative flux divergence was by use of radiation charts or complex numerical methods (Elsasser, 1942; Elsasser and Culbertson, 1960; Brooks, 1950). These techniques were further refined for the case of the boundary layer (Deacon, 1950; Funk, 1960) and computer technology has allowed flux divergence (div Q^*) to be incorporated into boundary layer models (Zdunkowski and Track, 1971; Atwater, 1972).

Funk (1960) made the first direct measurement of div Q^* at a rural site using accurate radiometry. Funk's results, later verified by Gaevskaya *et al.* (1973) show that with light winds and cloudless skies the radiative cooling rate considerably exceeds the actual measured cooling rate. Fuggle (1971) shows similar results for an above-roof urban site. The discrepancy is attributed to the fact that the radiative cooling is in fact offset by turbulent warming. Gaevskaya *et al.* (1973) point out that the radiative and turbulent processes are simultaneous, non-linear and cannot be simply added to achieve total cooling. This is further supported by the results of Timanovskaya and Farapanova (1967) who independently measured the radiative and sensible heat divergences.

Under calm conditions we might expect that the radiative divergence will dominate, and may approximate the actual cooling rate. Rider and Robinson (1951) found that on calm clear nights, the radiation divergence approached zero in the mean. The urban canyon is likely to be a good location since airflows sometimes almost becomes stagnant between the radiating elements. Thus div Q^* was studied in the canyon at night to observe its magnitude and direction, and to compare the radiative cooling rates $(\Delta T/\Delta t)_r$ with the actual cooling $(\Delta T/\Delta t)_{meas}$. In studying div Q^* it must be remembered that the canyon is not homogeneous in the lengthwise direction. Thus it is necessary to investigate both this horizontal divergence, and that in the canyon cross-section, resulting in canyon-air volume divergence.

2. Longitudinal Flux Divergence in the Canyon

Longitudinal flux divergence along the canyon length was investigated with the aid of two net radiometers whose longwave calibrations agreed to within 1 per cent. They were mounted at 3 m above the floor on two masts separated by a horizontal distance of 7.6 m and were located on either side of the main experimental cross-section. The radiometer receiving surfaces were oriented normal to the lengthwise direction, and their difference was taken to be the horizontal divergence. The radiometer signals were monitored every 10 min, and the data averaged over a 1 h period during the period from 1600 PST on July 17, to 0700 PST on July 20, 1973. Only the nocturnal data are considered here.

The overall longitudinal radiation divergence in the canyon-air volume $[Q^*]_H$ is given by:

$$[Q^*]_H = (Q_S^* - Q_N^*)W.H. \qquad (4.9)$$

where

Q_S^*, Q_N^* = the net all-wave radiation at the south and north ends of the canyon, respectively,

and the square brackets indicate volume averages. It is assumed that Q_S^* and Q_N^* are average values of Q^* for the south and north vertical cross-sections. Generally the radiometers indicated a net radiant cooling in the canyon. The possibility exists that this arises from different view factors for the two radiometers, but this is discounted on the grounds that the canyon has a uniform cross-section, and the distance to the canyon ends is considerable. The value of $[Q^*]_H$ obtained is interpreted to be due to the difference in thermal environment between the canyon and its surroundings.

The radiative temperature change per unit time in the canyon-air volume corresponding to the net change in storage $[Q^*]_H$ is given by:

$$\left(\frac{\Delta T}{\Delta t}\right)_r = \frac{[Q^*]_H}{\rho c_p . V} \qquad (4.10)$$

The resulting radiative cooling in the canyon-air volume for the three observation nights is given in Figure 4.6. Most of the cooling rates are in the range 0 to 1.0°C h^{-1} with a mean

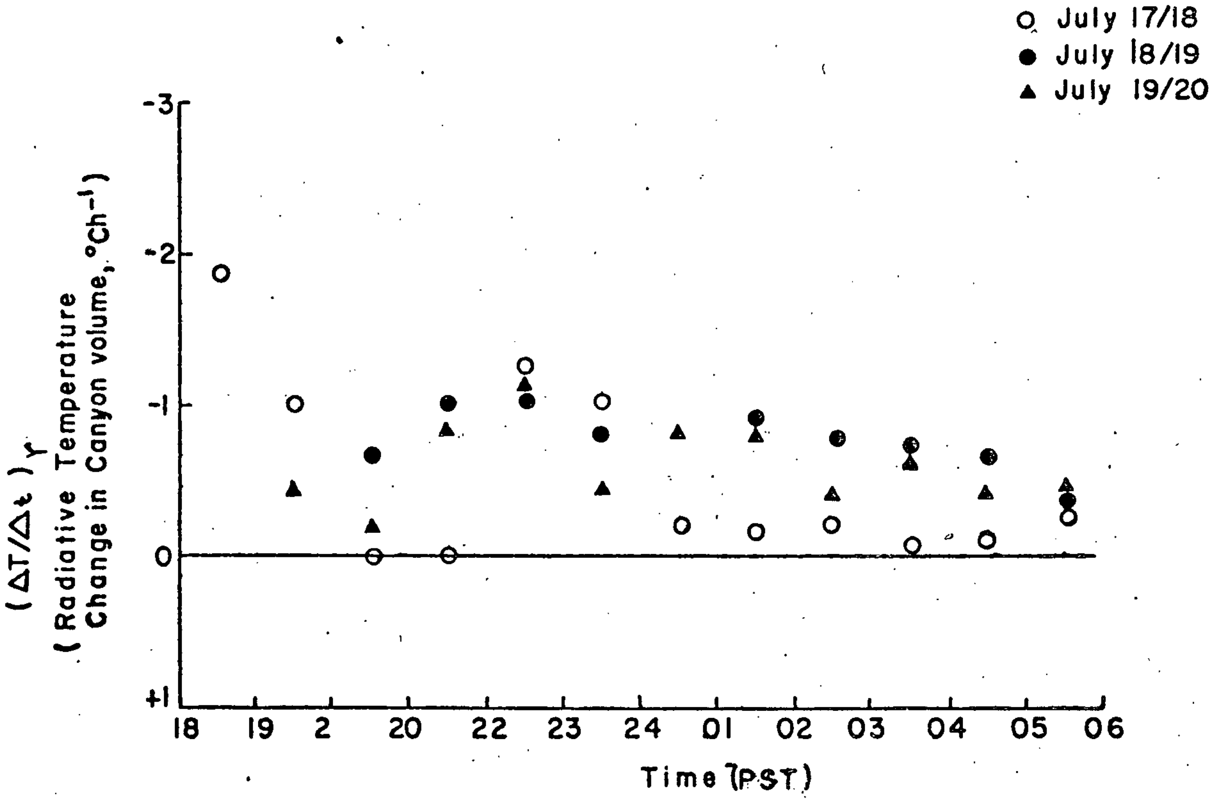

Fig. 4.6 Radiative energy storage in canyon volume due to lengthwise divergence $[Q^*]_H$

of 0.6°C h^{-1}. A regression line fitted to the data indicated a slight decrease in radiative cooling with time, but the slope was not highly significant. The results clearly show the existence of $[Q^*]_H$ in the urban canyon and therefore it must be considered in canyon-air cooling at night.

3. Flux Divergence in the Canyon Cross-Section

The radiative flux divergence for the canyon cross-section (i.e., the experimental section normal to the canyon axis) can be expressed in terms of a net storage in the air-volume:

$$[Q^*]_C = \{W.Q_g^* + H(Q_e^* + Q_w^*) - W.Q_t^*\}L \qquad (4.11)$$

Equation 4.11 can be evaluated using the mast and boom arrangement of radiometers described in Chapter 2. All of the Q^* terms on the right-hand side represent measurements around the perimeter of the cross-section. During nocturnal observations each of the five positions across the canyon cross-section was sampled once every 3 min before midnight and once every 6 min. after. The data were averaged over a 1 h period and $[Q^*]_C$ calculated. The sampling frequency is adequate to account for storage changes with time based on the work of Lee and Gille (1972). They show that air temperature changes in the atmosphere due to an oscillatory radiation field is a function of height so that high frequency fluctuations are damped within a few centimeters of the surface, leaving longer period waves to contribute at greater heights. Also Fuggle (1971) showed that high frequency fluctuations of div Q^* are an order of magnitude less than the steady-state value.

Figure 4.7 shows the variation of the radiative temperature change (using $[Q^*]_C$ in Equation 4.10) with time on four cloudless nights with light winds, 2 of which are incomplete data sets. In the early evening there is considerable scatter, probably as a result of temperature fluctuations associated with intermittent turbulence as the daytime winds subside to the nocturnal calm. Following sunset at approximately 1730 PST radiative cooling is strong (1.5 - 3.0°C h^{-1}), but as the night progresses this gradually decreases until about midnight following which radiative warming occurs. This is a very interesting pattern quite unlike most other environments reported, but its explanation is not clear. The possibility of measurement error due to dew deposition (increasing $L\downarrow$) is very unlikely because the instruments were checked visually whilst in operation and no dew was observed, and as the results in Chapter 6 will show, the canyon is characterized by evaporation throughout these nights. Assuming the warming is real its explanation must be related to the temperature structure.

In general most theory and measurements find radiative warming close to the ground by day (lapse conditions), and radiative cooling by night (inversion), but it is possible to find accounts of warming close to the ground at night. Fleagle

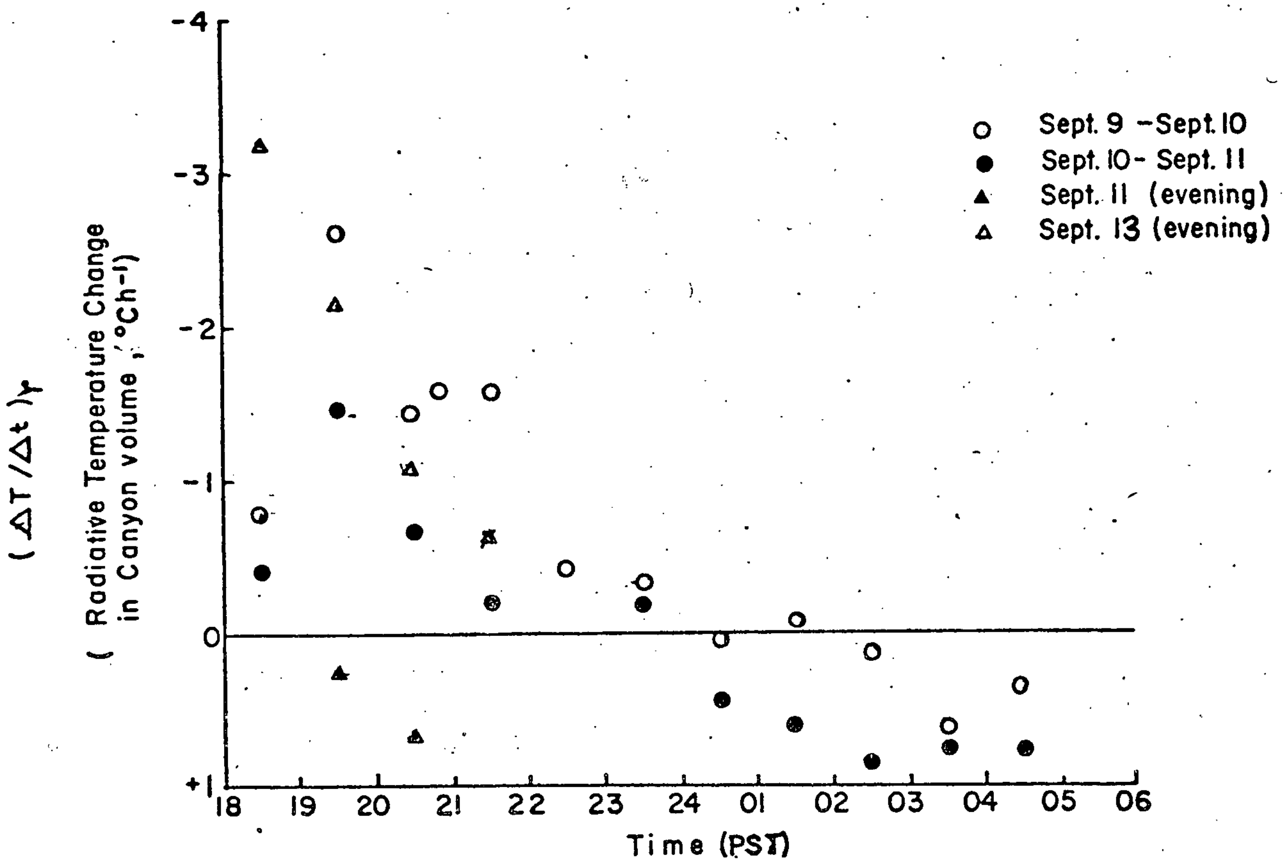

Fig. 4.7 Radiative energy storage in canyon volume due to cross-sectional divergence $[Q^*]_C$

(1965) and Kondo (1971) both note this close to the ground from theoretical considerations, and Lieske and Stroschein (1967) corroborate this from div Q^* measurements over an arctic snow surface.

In the three-dimensional canyon situation radiative warming occurs when the sum Q^* entering the volume is greater than the sum Q^* leaving the canyon top. This might occur if the canyon-air volume were warmer than the air above the canyon top and surrounding roofs. Unfortunately, no temperature data linking the canyon and the air layer above were observed in this study. It does seem realistic, however, to postulate that the roofs cool more than the canyon from view factor considerations (Figure 4.5).

D. RADIATIVE AND ACTUAL COOLING IN THE CANYON-AIR VOLUME

As mentioned it is not normal to expect actual measured cooling rates to agree with computed radiative rates, because the procedure neglects turbulent heat transfer as a process in producing air temperature change. However, for the case of stagnant air in a canyon it may not be unreasonable to expect agreement, and this possibility is tested here. Measured temperature change $(\Delta T/\Delta t)_{meas}$ was obtained by spatially averaging the mean hourly air temperatures across the canyon cross-section, and radiative change was computed using $[Q^*]_C$ in Equation 4.10. Data was available for the nights of September 9-11 and 13, 1973.

Figure 4.8(a) shows the agreement between $(\Delta T/\Delta t)_r$ and $(\Delta T/\Delta t)_{meas}$. Large scatter is obtained at high cooling rates which tend to occur in the early evening and may be related to unsettled winds at this time (see also Figure 4.7). Because the variance is not evenly distributed a regression analysis was not attempted. However, when the data prior to 2030 PST are eliminated a more defined relation is obtained [Figure 4.9(a)]. The least squares fit to the data indicates that $(\Delta T/\Delta t)_r$ is approximately twice as large as $(\Delta T/\Delta t)_{meas}$, and the relationship is significant at the 1% level.

These relations do not, however, account for $[Q^*]_H$. If we assume the rates given in Figure 4.6 are applicable to the September data then an overall canyon-air volume flux divergence $[Q^*] = [Q^*]_H + [Q^*]_C$ is obtained. Although this approach oversimplifies the situation it is the only practical means available here. Figures 4.8(b) and 4.9(b) show how the total radiative temperature change (using $[Q^*]$ in Equation 4.10). agrees with the measured cooling for all the data, and for data after 2030 PST respectively. Again the latter relation is best and significant at the 1% level. The slope of the relation in Figure 4.9(b) is 2.27 and this is considerably smaller than the 3.5 reported by Funk (1960) for a rural site, and 3.0 given by Fuggle (1971) for an above-roof urban site. These differences are probably related to such site physical properties as atmos-

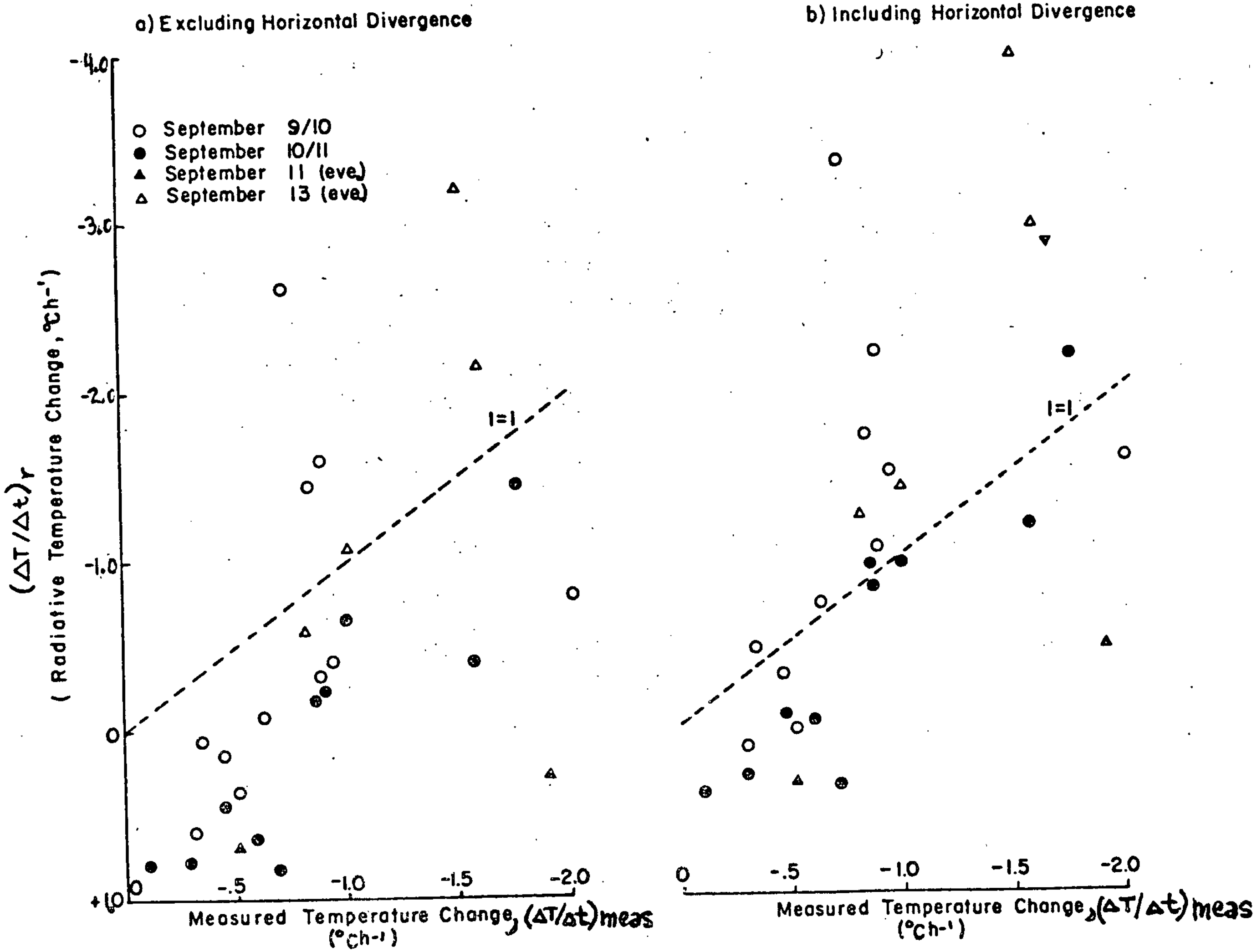

Fig. 4.8 Radiative vs. measured temperature change for all data.

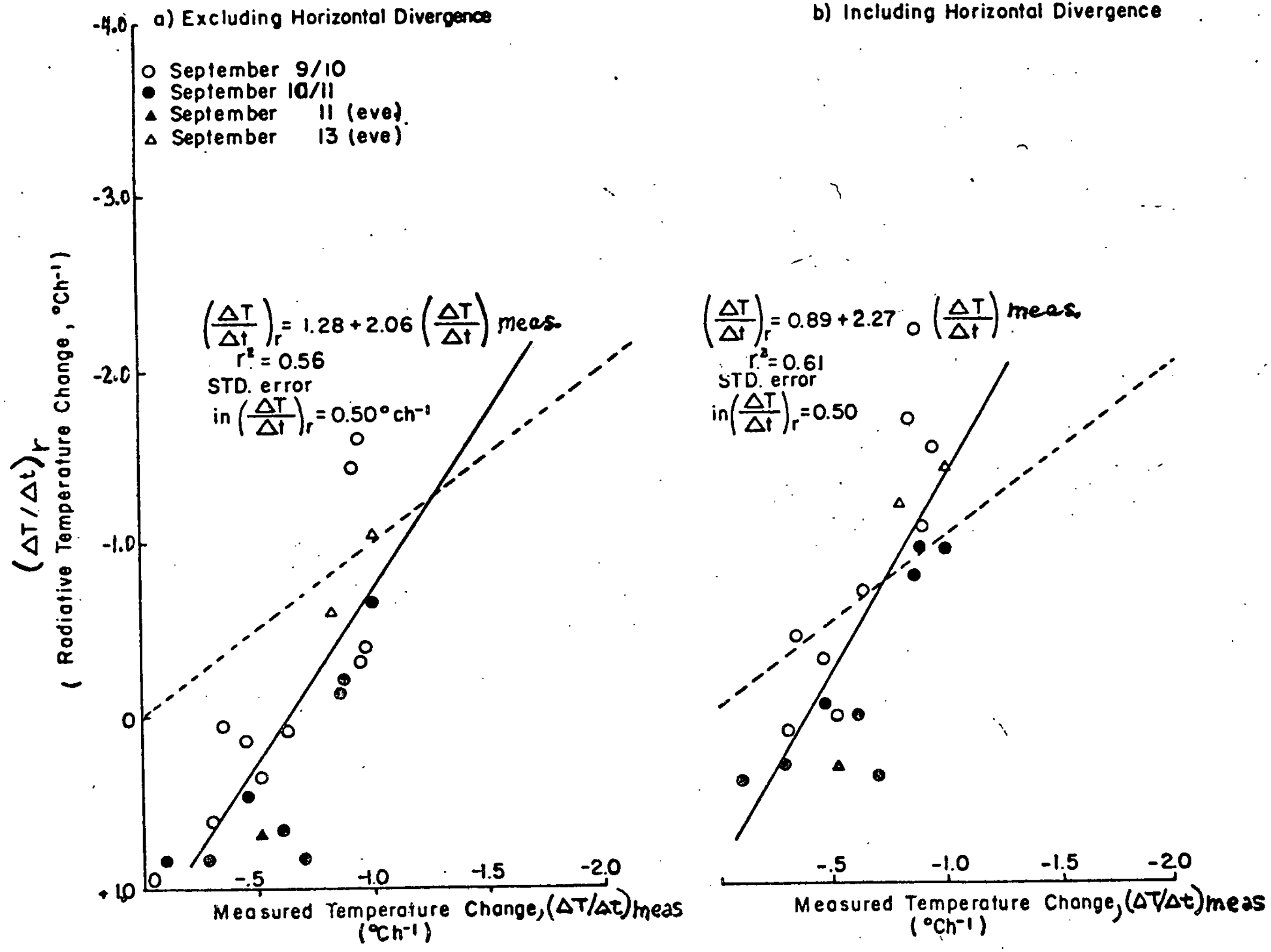

Fig. 4.9 Radiative vs. measured temperature change for data collected after 2030 PST.

pheric emissivity, sky view factor, aerodynamic roughness and vertical temperature structure. The results bear out the hypothesis that in a sheltered urban canyon the agreement between $(\Delta T/\Delta t)_r$ and $(\Delta T/\Delta t)_{meas}$ is improved. This is further supported by Figure 4.10(a) which compares the radiative, and actual cooling following sunset. Initially radiative cooling is stronger than the measured, but 5h after sunset the trend reverses due to the flux convergence noted in Figure 4.7. The cumulative agreement is excellent since by 9h after sunset the difference is only 0.5°C. At any time during the cooling period the maximum discrepancy is approximately 1.2°C.

Although radiative flux divergence gives useful insights into the physical processes controlling nocturnal cooling, its usefulness as a predictive or forecasting tool is limited, especially in an urban canyon where a theoretical framework has yet to be formulated. A much more common approach is to relate air cooling to surface cooling via an analysis presented by Brunt (1941). The Brunt formula is a solution of the surface energy balance equation for conditions when advection, and appreciable sensible or latent heat transfer may be neglected. This occurs under cloudless, light wind conditions and then the L^* loss must be balanced by an upward flow of heat from the underlying medium. Further, if L^* is assumed to be constant with time (for the canyon see Figures 4.1 to 4.4 at night) and the initial subsurface temperature profile is assumed isothermal, then the surface temperature decrease from sunset (ΔT_s) is given by:

$$\Delta T_s = - \frac{2L^*}{\pi^{\frac{1}{2}}(kC)^{\frac{1}{2}}} \cdot t^{\frac{1}{2}} \qquad (4.12)$$

where

t = time from sunset,

C = heat capacity of the underlying medium.

Similar but more complex formulae have been developed by Fleagle (1950), and Haltiner and Martin (1957) but they involved too many input parameters for use here. Kawamura (1965) showed that intra-urban air temperature differences were correlated with surface conductivity and heat capacity. Oke and Maxwell (1975) show that although Equation 4.12 fits rural data well, it is not as useful in describing the urban cooling in Montreal and Vancouver whose cooling appears to be linearly related to time.

Although Equation 4.12 was intended for horizontal surfaces it was tested here for use in describing cooling in the canyon, with appropriate modification. Firstly, the values for k and C were selected (Table 4.2). The canyon floor was assumed to be composed of 80% gravel (granite + air) and 20% sandy clay, and the gravel was found to contain 37% air by volume.

Secondly, it is not clear where L^* refers to in the case of the canyon. Two different values were used in Equation

4.12, one was an average L^* for the three canyon surfaces computed in the same manner as $\bar{Q}^*$ (Equation 4.2), the other was L^* for the canyon top computed as Q_t^* (Equation 4.4).

TABLE 4.2

VALUES OF THERMAL CONDUCTIVITY (k), HEAT CAPACITY (C), THERMAL ADMITTANCE (μ) FOR CANYON MATERIALS

MATERIAL	k $(W\ m^{-1}\ K^{-1})$	C $(J\ m^{-3} K^{-1})$	$\mu^\dagger$ $(J\ m^{-2}\ K^{-1}\ s^{-1/2})$	SOURCE
CONCRETE	1.60	2.09×10^6	1.83×10^3	I.H.V.E. (1969)
GRANITE	2.80	2.15×10^6	2.45×10^3	List (1965)
SANDY CLAY	0.92	2.47×10^6	1.51×10^3	List (1965)
AIR	0.02	1.20×10^3	4.89	List (1965)
CANYON AVERAGE	1.60	1.88×10^6	1.73×10^3	Calculated

$^\dagger \mu = (kC)^{1/2}$

The results of the Brunt calculations are compared with the average measured canyon cooling [calculated as in Figure 4.10 (a)] in Figure 4.10(b). Clearly the Brunt curve using the average surface L^* value is unsatisfactory but that using L^* for the canyon top is a good deal closer to the measured results, such that a slight adjustment in the μ value would produce good

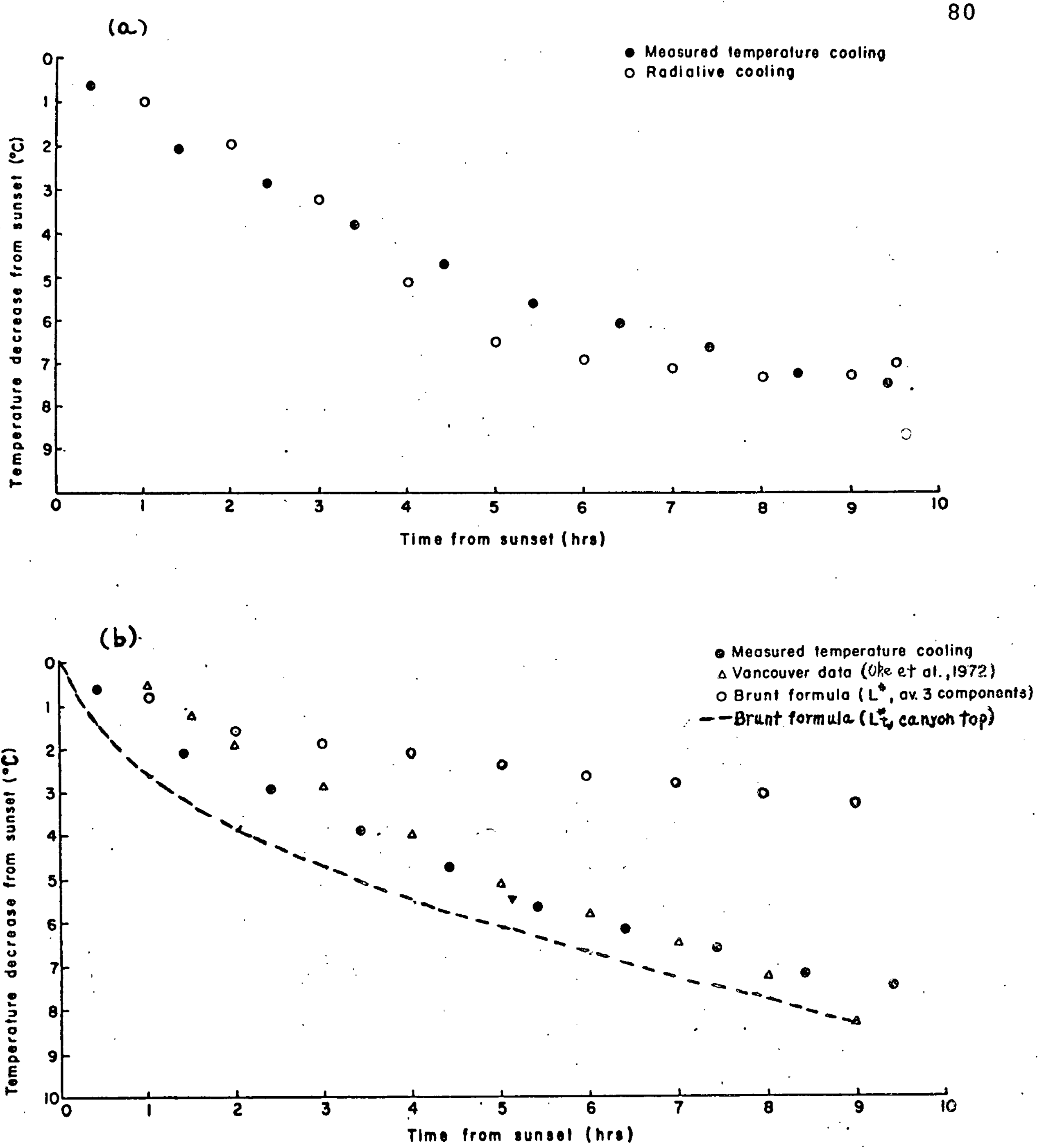

Fig. 4.10 Temperature decrease after sunset in the canyon using data for September 9, 10, 11 and 13: (a) compared with total radiative cooling in the canyon averaged over the same period; (b) compared with the Brunt cooling rate.

agreement. In the first few hours after sunset the Brunt curve represents too high a cooling rate but later it almost parallels the measurements. It may be that increased turbulence in the early evening retards the canyon cooling, or it may be that initially the surface cools more rapidly than the air. Alternatively it may be that the sensible heat loss from the top of the canyon is restricted in the early evening until the warmer canyon air possesses enough buoyancy to interact with the air layer above.

Results from Oke and Maxwell (1975) are also included in Figure 4.10(b). These data are spatially averaged temperatures observed during automobile traverses in central Vancouver on cloudless nights with very light winds. The results, therefore, also refer to in-canyon conditions and the agreement with the data here is remarkably good especially after about 3h after sunset.

The Brunt analysis provides a relatively simple way to model the heat island using appropriate surface properties for urban and rural areas, but it is restricted to the meteorological conditions outlined.

CHAPTER 5

SUBSURFACE HEAT FLUX IN THE CANYON

A. INTRODUCTION

The subsurface heat flux (Q_G) is considered to be an important term in urban climates. It is commonly regarded as a critical factor in the development of the nocturnal heat island (i.e., release of stored daytime heat from building materials), but there are no direct studies to verify such an assertion. In addition in the case of a 'dry' canyon an ability to apportion the appropriate amount of Q^* that is used or provided by Q_G automatically gives Q_H as a residual.

Given the thermal properties of the material (especially k and C), and the surface boundary conditions the subsurface heat flux could be derived theoretically (e.g., Carslaw and Jaeger, 1959). For the canyon, however, the surface boundary conditions are not all known and direct measurement of Q_G was undertaken.

This chapter examines the problems of measurement of Q_G in the canyon (including the calibration, behaviour and errors associated with heat flux plates), and the typical pattern of heat conduction in the canyon. In particular the patterns of Q_G are related to the complex input (or loss) of radiant energy in the canyon (as shown in Chapters 3 and 4).

B. CALIBRATION

The heat flux plates (described in Chapter 2) were supplied with factory calibrations. A check on this calibration was first conducted following the technique of Idso (1971, 1972). Details are provided in Appendix A. In outline the method involves the heat flux sensor being placed in front of a hot plate the heat output of which is continuously adjusted. Both sides of the sensor, and the hot plate are painted flat black, and the experiment is conducted in a controlled light and temperature environment. A plot of sensor output at known hot plate temperatures should yield a straight line, the slope of which is related to the sensor calibration.

A comparison between six of these laboratory calibrations and those supplied by the factory is given in Table 5.1. Clearly the laboratory technique gives lower sensor output calibrations, but the range of differences (6 - 25%) is unacceptably large. The repeatability of the laboratory calibration was found to be approximately 10% for a given plate. Random errors are unlikely to explain the observed factory/laboratory calibration differences which are therefore probably related to an error in one of the procedures.

A second independent check on the factory calibration was conducted following the scheme of Fuchs and Tanner (1968). This involves immersing the sensor in a substance of known thermal conductivity, and measuring the vertical temperature gradient across it. By employing a modification of Equation 2.1, the sensor output at known heat flux rates is obtained.

TABLE 5.1

COMPARISON OF HEAT FLUX PLATE CALIBRATIONS

PLATE NO.	FACTORY CALIBRATION ($\mu V/Wm^{-2}$)	LABORATORY CALIBRATION ($\mu V/Wm^{-2}$)	LAB./FACT. RATIO	% DIFFERENCE FROM FACTORY
1	0.71	0.63	0.89	11
2	0.86	0.65	0.75	24
3	0.71	0.67	0.94	6
4	0.69	0.57	0.83	17
5	0.75	0.64	0.86	13
6	0.79	0.59	0.74	25
Mean			0.84	16

Following Fuchs and Tanner a plate was placed in a box (0.53 x 0.53 x 0.18m) of dry beach sand. The plate was located at a depth of 5 cm and thermocouples were used to measure the vertical temperature differences between the 3 and 5 cm, and 5 and 7 cm depths. The sand heat flux (Q_G) was then assumed to be given by:

$$Q_G = k_s \{ (\frac{\Delta T_z}{\Delta z})_{3-5} + (\frac{\Delta T_z}{\Delta z})_{5-7} \} /2 \qquad (5.1)$$

where

k_s = thermal conductivity of sand (assumed value of 0.25 $Wm^{-1}K^{-1}$ after Fuchs and Tanner, 1968);

$(\frac{\Delta T_z}{\Delta z})_{x-y}$ = vertical temperature gradient between depths x and y.

Figure 5.1 gives the results of comparison between Q_G obtained from the gradient method (Equation 5.1) and from the heat flux plate (using both the factory and laboratory calibrations), for an experiment conducted out-of-doors. Some of the data scatter is probably attributable to the combined effects of the natural variability in the radiant input and convective activity, and the different response times of the thermocouples vis-a-vis the heat flux plate. The factory calibration underpredicts the flux (regression slope = 0.85), whereas the laboratory calibration slightly overpredicts (regression slope = 1.14). There is little to choose between the two approaches, but the factory values would appear better for the following reason.

Preliminary measurements up to 10 days prior to the results in Figure 5.1 suggest that the original sand was not entirely dry and thus the assumed value of k_s was incorrect. This drying appears to be almost complete by June 28 but any further slight changes would bring the factory results closer to the 1:1 line, but move the laboratory values further away. Knowing the plates were to be used in concrete in the canyon, it was decided to repeat the gradient approach experiment using a concrete block.

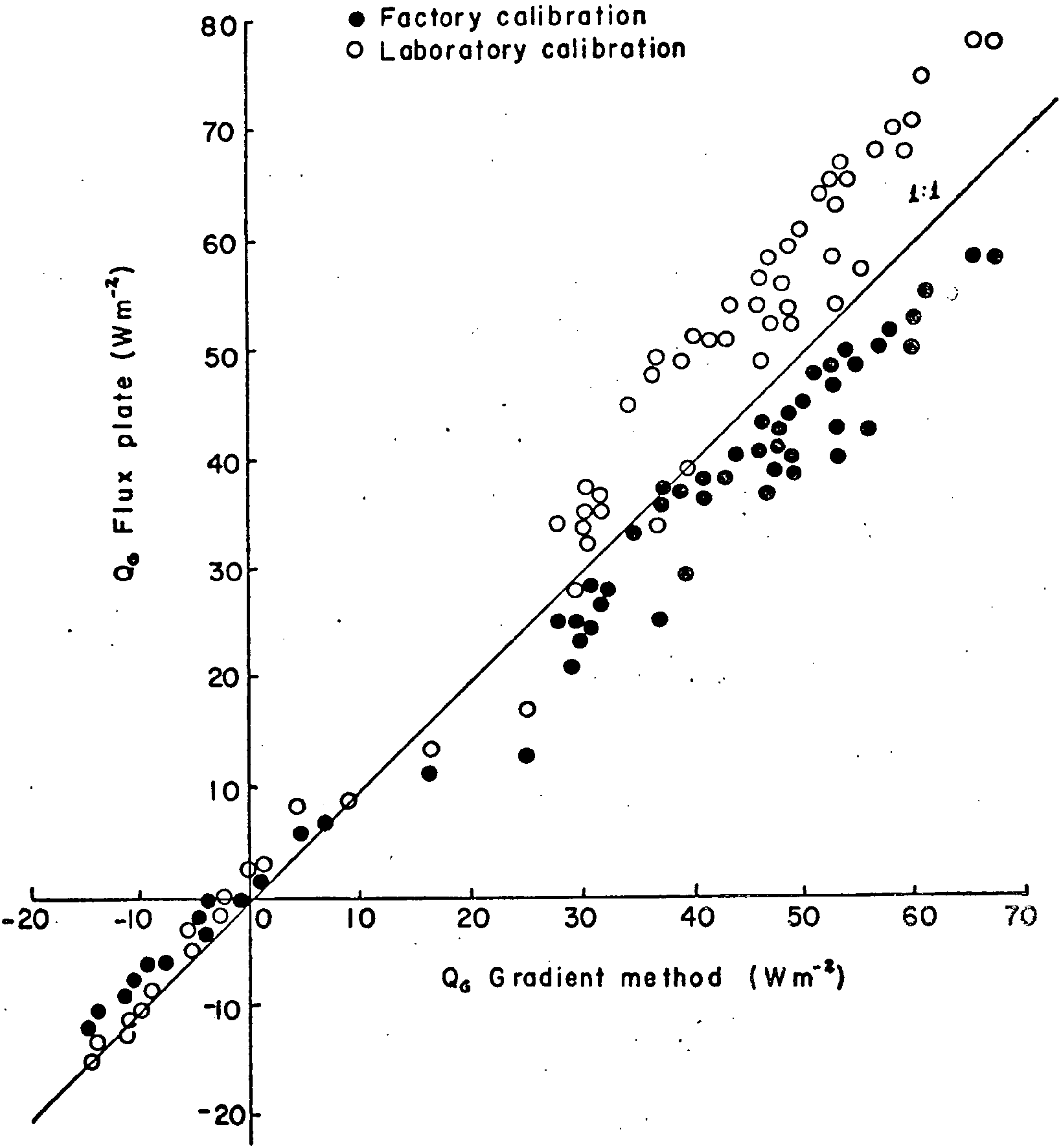

Fig. 5.1 Comparison of soil heat flux plate with gradient measurements (sand). June 27, 28, 1973.

C. CALIBRATION IN CONCRETE

To repeat the sand experiment using concrete requires a knowledge of the thermal conductivity of concrete (k_c). The value of k_c, however, shows a wide range of values (see I.H.V.E., 1969) therefore experimental determination was deemed necessary.

The value of k_c for the concrete block was determined using a thermal comparator (Powell, 1957; Ansori and Iqbal, 1971). The comparator consists of two phosphor-bronze spheres (0.4 cm diameter) mounted in balsa wood. One sphere protrudes slightly from the wood, the other remains slightly inset, and the differential temperature between them is measured by 36 AWG iron-constantan thermocouples. The procedure is to heat these units to approximately 70°C in an oven and allow the differential temperature to settle to zero. The comparator is removed and placed in contact with the sample which is at room temperature. Ansori and Iqbal (1971) then show that the spheres cool at different rates, and by conduction alone, and that the cooling is proportional to the root of the sample's conductivity. The conductivity of the sample can be measured if samples of other materials of known conductivity are available for comparison. In this case samples of ebonite, pyrex and quartz (thermal conductivities 0.19, 1.15 and 1.40 $Wm^{-1}K^{-1}$, respectively) were compared with a slab of concrete (18 x 13 x 2.5 cm) cut from the block used in the experiment. Figure 5.2 shows an example of the $k^{\frac{1}{2}}$ vs cooling plots. This experiment yielded $k_c = 0.85$ $Wm^{-1}k^{-1}$, and on the basis of other runs a mean value of $k_c = 0.90$ $Wm^{-1}K^{-1}$ was selected for use.

It is implicit in the theory of the heat flux plate that the plate conductivity be roughly equivalent to that of the medium in which it is immersed. Soil heat flux plates of the type used here normally have thermal conductivities within the range of most soils, 0.3 to 30.0 $Wm^{-1}K^{-1}$ (Fuchs and Tanner, 1968), and the concrete value lies within this range. Because the actual thermal conductivity of the plates were not available (either from the manufacturer, or from experiment) the heat flux output of the plates was directly compared with that from the gradient method outlined in the previous section.

Concrete was poured to form a block (0.42 x 0.42 x 0.15 m). This enclosed a heat flux plate at a depth of 5 cm and two temperature difference thermocouple pairs between 3 and 5 cm, and 5 and 7 cm as in the sand experiment. After allowing the concrete to dry, measurements were conducted out-of-doors to give simultaneous heat fluxes from the plate and the gradients using Equation 5.1, and k_c derived from the comparator experiment.

The results of this experiment are given in Figure 5.3. Clearly the comparison using the factory calibration is

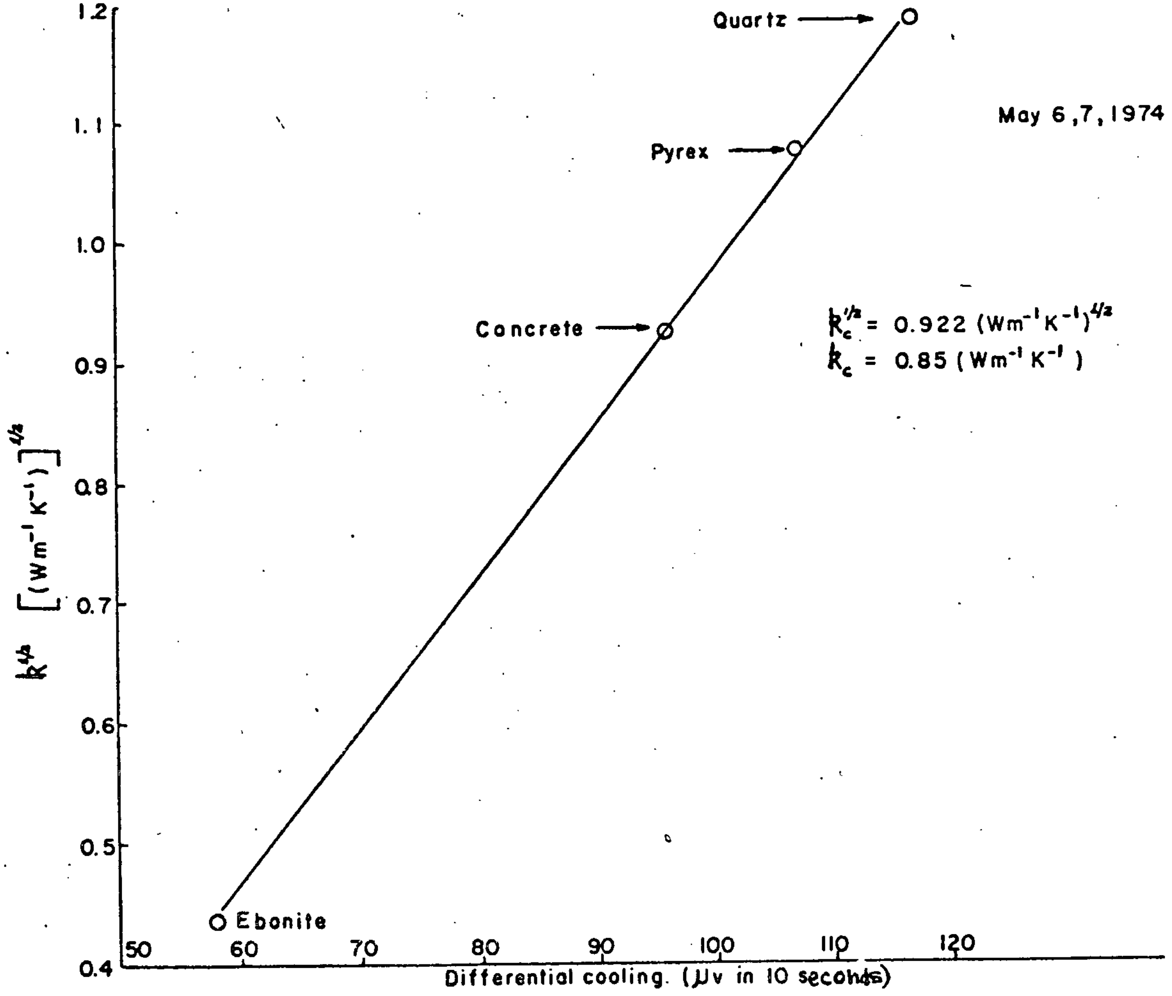

Fig. 5.2 Determination of the thermal conductivity of concrete.

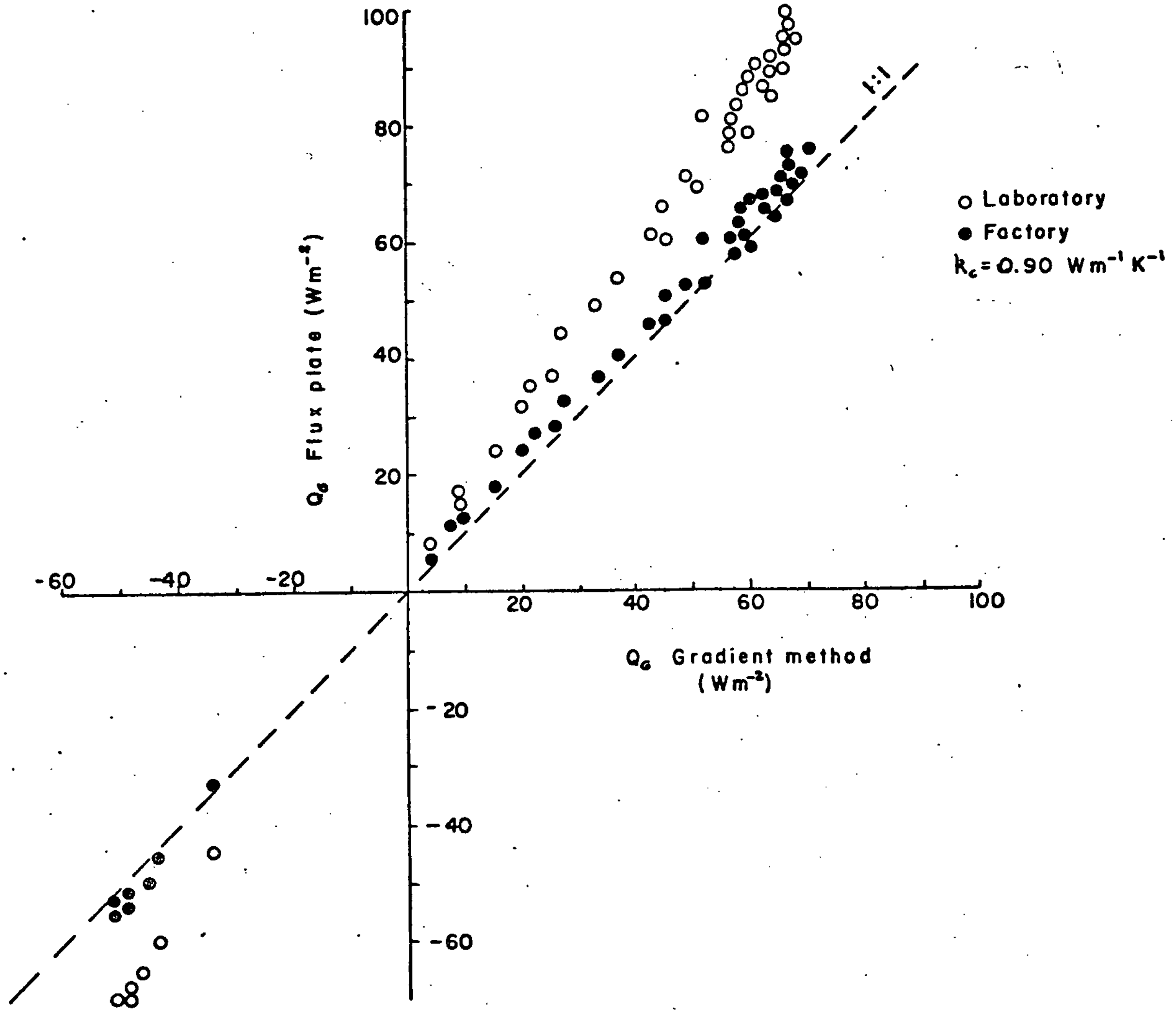

Fig. 5.3 Comparison of soil heat flux plate with gradient measurements (concrete). May 30, 31, and June 4, 1973.

superior, and this verifies the tentative conclusion reached in the preceding section. The agreement using the factory calibration is within 5%, and on this basis factory values were applied to all the canyon subsurface data.

D. SUBSURFACE FLUX DIVERGENCE

Heat flux plates inserted beneath the surface refer to heat fluxes at that depth and not those at the surface/atmosphere interface which are needed in the surface energy balance. It is therefore necessary to estimate this divergence to assess its importance. The vertical divergence in the heat flux Q_G is given by:

$$\frac{\partial Q_G}{\partial z} = C\frac{\partial T_z}{\partial t} \qquad (5.2)$$

Integration between the surface and a depth z gives:

$$Q_{G(o)} = Q_{G(z)} + C\int_o^z \frac{\partial T_z}{\partial t}\,dz \qquad (5.3)$$

where

$Q_{G(o)}$ = conductive heat flux at the interface;

$Q_{G(z)}$ = subsurface heat flux at depth z.

The second term on the right hand side of Equation 5.3 may be approximated:

$$C_o \int^z \frac{\partial T_z}{\partial t} dz \simeq C \frac{\Delta T_z}{\Delta t} \Delta z \qquad (5.4)$$

Flux divergence in building materials was first evaluated in the tar and gravel roof of the U.B.C. Geography Building. Equations 5.3 and 5.4 were used to estimate this divergence by measuring Q_G at 0.5 cm with a flux plate, $\Delta T_z/\Delta t$ at 0.25 cm with a thermocouple, and using $C = 3.17 \times 10^6 Jm^{-3}K^{-1}$ (Saal, Heukelom and Blokker, 1940; I.H.V.E. Guide, 1969). The results in Figure 5.4 show divergence to be least at night with a slight tendency for underestimation of the nocturnal upward flux using the plate alone. In the late morning there is an underestimation by the plate of the flux into the roof, reaching a maximum of 40 Wm^{-2}, or about 35% of $Q_{G(o)}$, at about 1000 PST. The divergence changes sign in the afternoon so that the plate alone will overestimate the flux when $Q_{G(o)}$ becomes negative. This hysteresis behaviour is consistent with soil results (Fuchs and Tanner, 1968; Fuchs and Hadas, 1972).

Table 5.2 presents a comparison of the maximum flux divergences for the roof, the canyon concrete walls, and the canyon floor. The canyon $\Delta T_z/\Delta t$ values are surface values measured with a Barnes Infra-red Thermometer (Model PRT 10, Barnes Engineering Ltd.), and are therefore larger than a layer average. Equally they were taken in extreme conditions when shading of a sunlit wall causes sudden cooling and therefore provide safe overestimates. The divergences in Table 5.2 refer to the layer from the surface to 0.5 cm (the depth of the plates).

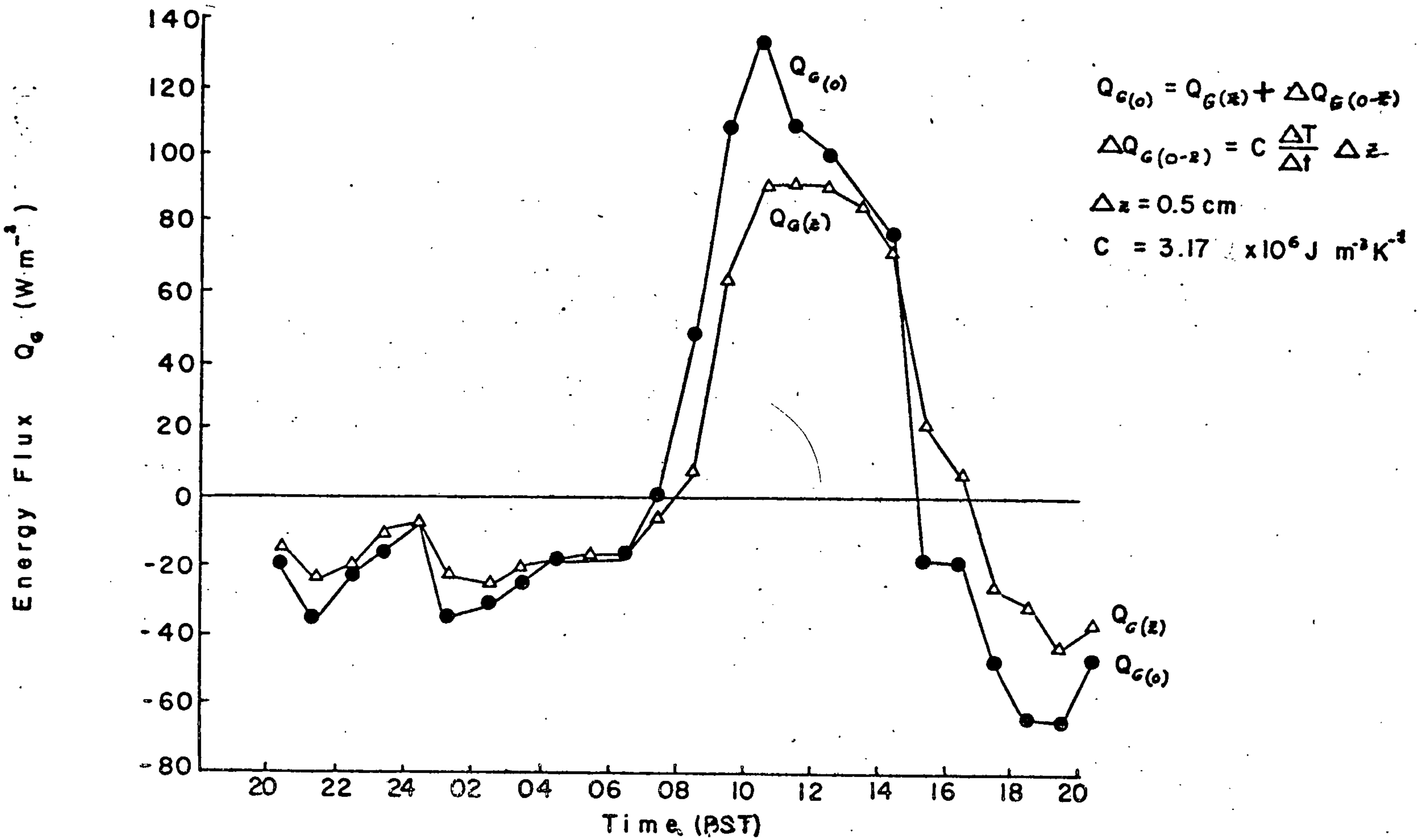

Fig. 5.4 Divergence experiment in Geography Building roof, U.B.C. September 5, 6, 1974.

TABLE 5.2

COMPARISON OF ROOF, WALL AND FLOOR MAXIMUM HEAT FLUX DIVERGENCES

SURFACE	C ($J\ m^{-3}K^{-1}$)	$\Delta T_z/\Delta t$ ($^oC\ s^{-1}$)	div $Q_{G(0-0.5)} = C(\Delta T_z/\Delta t)\Delta z$ ($W\ m^{-2}$)
Roof	3.17×10^6	25.2×10^{-4}	40
Canyon Walls	$2.09 \times 10^{6*}$	5.5×10^{-4}	6
Canyon Floor	$1.57 \times 10^{6*}$	44.6×10^{-4}	35

*From Table 4.2

In more uniform conditions the canyon $\Delta T_z/\Delta t$ measurements indicate that div $Q_{G(0-0.5)}$ will only be 12-20% of these maximum values and in energy terms can be considered small (i.e., walls 0.75 - 1.2 $W\ m^{-2}$; floor 4.4 - 7.0 $W\ m^{-2}$). Consequently, no corrections for flux divergence were applied to the canyon data.

E. SUBSURFACE HEAT FLUX IN THE CANYON

The nature of Q_G in the canyon was intensively studied in the period July 26 to August 1, 1973. This period was characterized by cloud-free conditions and light winds.

Observations were made every 10 min from each of the 17 heat flux plates in the canyon cross-section [Figure 2.5(b)]. The data were averaged to give half-hourly means. The diurnal pattern was consistent from day to day and therefore the results for one day (July 27) may be assumed typical.

Figure 5.5 shows the daytime variation of Q_G at two positions, for each of the three canyon surfaces on July 27. Obviously, the storage pattern in each component surface is strongly related to the pattern of Q^*, as comparison of Figures 4.1 - 4.3 and 5.5 will show. Common features of the daytime Q^* and Q_G regimes include the relative timing and magnitude of the peak fluxes at each location; the secondary peaks related to reflection of solar radiation from the two walls; and the relative lack of differentiation in flux magnitude when the surface is not in receipt of direct beam shortwave radiation.

The nocturnal results also show agreement with the Q^* (or L^*)pattern. In particular in the early evening the greatest storage release from both walls is from the locations with the largest sky view factor (i.e., the highest sensor level). The difference is much smaller in the late night period, presumably because the L^* losses are less when the heat reservoir is somewhat depleted. All locations in the canyon exhibit negative Q_G values at night (i.e., heat flow out of the buildings and ground). The upper level on the west wall also shows nega-

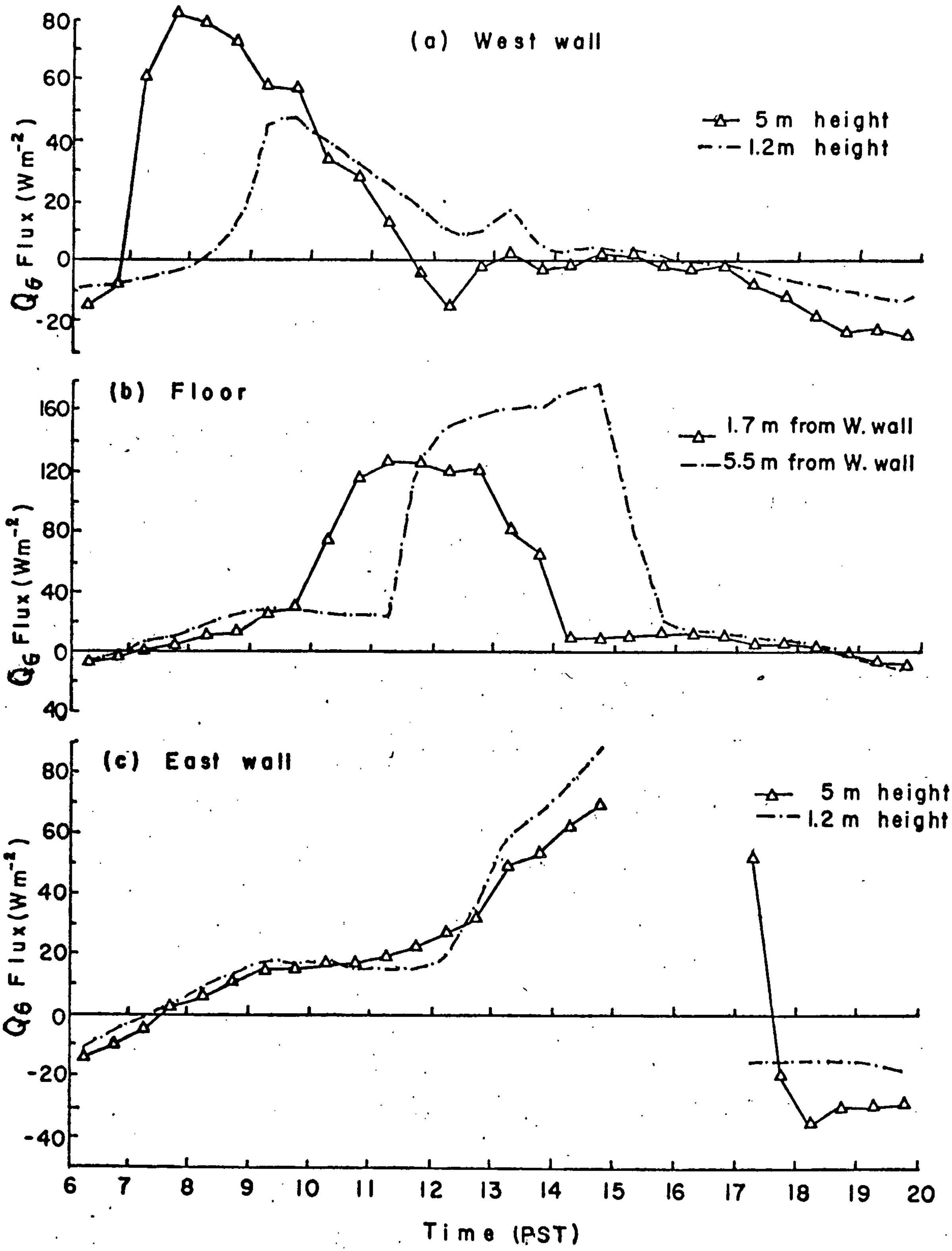

Fig. 5.5 Subsurface heat flux at fixed points in the canyon. July 27, 1973.

tive Q_G at midday, just after it becomes shaded. This behaviour is similar to that described by Yap and Oke (1974). Their qualitative explanation suggests that if a strongly heated surface is plunged into shade its rapid surface cooling reverses the temperature gradient in the topmost layer and results in an upward heat flux, even though Q^* may not be negative. The same explanation may explain the sharp reversal in the direction of Q_G at the upper sensor level on the east wall at about 1730 PST. It is also clear that Q_G for the ground at night is less than for the walls. This is opposite to expectations based on view factor considerations. It is possible that this is due to the fact that Q_G from the walls is enhanced by the release of anthropogenic heat (Q_F) from the buildings.

The spatially averaged fluxes for each surface (Q_{Gw}, Q_{Gg} and Q_{Ge}) are given in Figure 5.6(a). This clearly demonstrates that the importance of the individual components is restricted to separate times of the day, and also the dominant role played by the ground heat storage in absolute terms.

In a manner analogous to Equations 3.3 and 4.2, a spatially averaged $\bar{Q}_G$ over the three canyon surfaces is defined:

$$\bar{Q}_G = \frac{Q_{Gw} \cdot H + Q_{Gg} \cdot W + Q_{Ge} \cdot H}{2H + W} \quad (5.5)$$

The result is given in Figure 5.6(b), which is characterized by a smooth diurnal course, approximately symme-

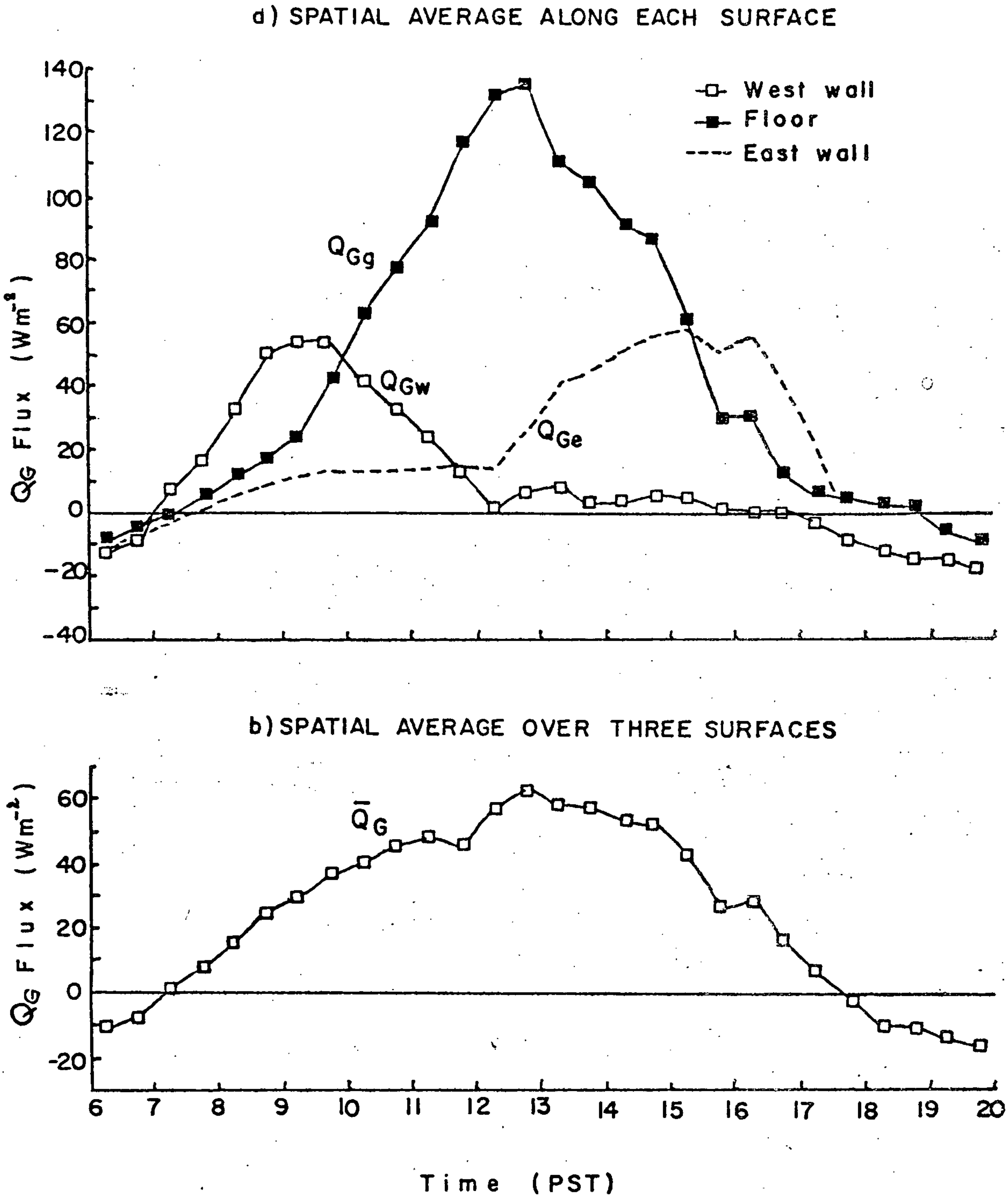

Fig. 5.6 Spatial average of the subsurface heat flux for July 27, 1973: (a) averaged along each canyon surface; (b) averaged over the three canyon surfaces.

trical about noon, even though the component surface roles are not. Also it is noted that the peak $\bar{Q}_G$ of 53 W m^{-2} is attained at about 1245 PST, close to solar noon (1315 PST). It is normal for Q_G to peak about 2 h ahead of Q^* for most unobstructed horizontal surfaces (Sellers, 1965). Although daily total calculations for the walls showed slight deficits, this was largely offset by a net gain in the floor and the ground. Thus for the whole system the daily total storage approximates zero.

CHAPTER 6

ENERGY BALANCE OF THE CANYON

A. INTRODUCTION

As noted in Chapter 1, solution of the energy balance of the canyon is an important objective of this study. The complexity of the urban/atmosphere interface has discouraged direct measurement of the energy balance until recently. There are a few pilot studies of the urban energy balance above roofs (e.g., Oke *et al.*, 1972; Yap, 1973; Yap and Oke, 1974) and over paved urban surfaces (Landsberg and Maisel, 1972), but none for the canyon environment.

The energy balance for most surfaces may be written as in Equation 1.1:

$$Q^{*} + Q_{H} + Q_{E} + Q_{G} = 0 \qquad (6.1)$$

We observe the sign convention that positive quantities contribute to interface warming, and negative ones to cooling. In this study Equation 6.1 was used for the energy balance of the canyon floor where Q^{*}, Q_E and Q_G were available from measurement, and Q_H was obtained as a residual. For the painted-concrete canyon walls Q_H was again determined as a residual in Equation 6.1 but Q_E was assumed to be zero. Anthropogenic heat terms will modify Q_G but will not introduce errors in the surface energy balance. The energy balance for each of the component surfaces is given in Section C of this chapter.

Whenever measurements remote from a finite surface are used to characterize the energy balances at the interface the possibility of energy advection from surrounding environments must be considered. Convergence or divergence of heat within the canyon from outside will mean that Equation 6.1 does not represent the surface balance correctly. Equally the energy balance of the canyon system defined across the top:

$$Q_t^* + Q_{Ht} + Q_{Et} + Q_{Gt} = 0 \qquad (6.2)$$

will not agree with measurement if energy is added to the canyon-air volume by advection from outside. To evaluate the role of advection in the canyon an experiment was conducted, and is reported in Section B ahead of the energy balance results. Finally, this chapter deals with the air cooling/warming rates in the canyon because these are the thermal climatic expression of the energy exchanges, and because they provide some indirect verification of the canyon air circulation.

B. ADVECTION - HORIZONTAL AND VERTICAL TRANSPORT OF HEAT BY MEAN MOTION

Here we will consider the problem of advective heat transport into (or out of) the canyon under two types of air flow. Initially we will consider the simplest condition where the wind is flowing parallel to the canyon sides (i.e., lengthwise) as illustrated in Figure 6.1(a). Later we will

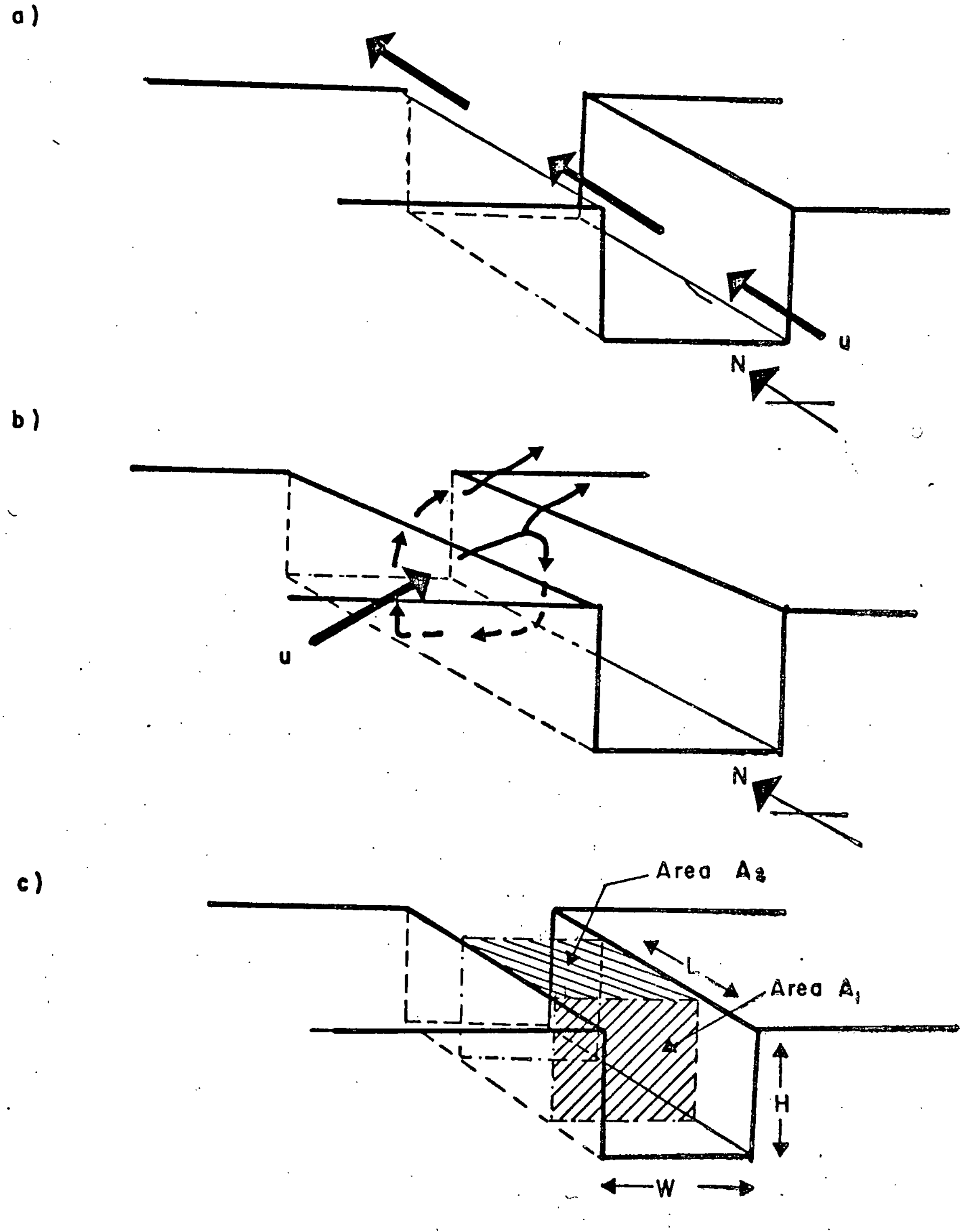

Fig. 6.1 Schematized air flow in the canyon.

consider the case of Figure 6.1(b) where the external wind strikes the canyon at some angle to the lengthwise axis. The dimensions and areas in the analysis which follows are given in Figure 6.1(c).

1. Flow Parallel to Canyon

Let u_o be the instantaneous wind velocity, averaged over the cross-sectional area A_1, for the parallel-flow case. Then the mean-horizontal heat transport through A_1 can be approximated by:

$$\begin{aligned} \rho c_p \, \overline{u_o T_o A_1} &= \rho c_p \overline{(\bar{u}_o + u_o')(\bar{T}_o + T_o')} A_1 \\ &= \rho c_p (\bar{u}_o \bar{T}_o + \overline{u_o' T_o'}) A_1 \qquad (6.3) \end{aligned}$$

where

$\bar{u}_o$ = time-averaged horizontal velocity,

u_o' = instantaneous velocity departure from the mean,

T_o = instantaneous air temperature,

$\bar{T}_o$ = time-averaged air temperature,

T_o' = instantaneous temperature departure from the mean .

and these results are assumed representative over the cross-section A_1. The first and second terms in Equation 6.3 represent the mean, and turbulent heat transport respectively. Similarly at some distance L downstream the mean transport through the canyon cross-section will be:

$$\rho c_p(\bar{u}_1\bar{T}_1 + \overline{u_1'T_1'})A_1 \tag{6.4}$$

and the mean heat flow through the canyon top (Q_{Ht}) is:

$$Q_{Ht} = \rho c_p(\overline{wT_2})A_2$$

$$= \rho c_p(\overline{w}\,\overline{T}_2 + \overline{w'T_2'})A_2 \tag{6.5}$$

where

w = instantaneous vertical velocity averaged over the area $A_2 = W.L$,

$\bar{w}$ = time-averaged vertical velocity,

w' = instantaneous vertical velocity departure from the mean,

$\bar{T}_2$ = time-averaged air temperature, and space-averaged over the canyon top area A_2,

T_2' = instantaneous departure from $\bar{T}_2$.

Denoting positive changes by the delta symbols, we have $\bar{u}_1 = \bar{u}_o - \bar{\Delta}u_o$ since any change in $\bar{u}$ inside the canyon must be due to friction with the walls. The sign of the change in $\bar{T}_o$ is not certain so that $\bar{T}_1 = \bar{T}_o \pm \Delta\bar{T}_o$. Substituting these relations in the energy balance of the canyon-air volume gives:

$$\rho c_p[\overline{u_o T_o A_1} - \overline{u_1 T_1} A_1 - \overline{wT_2} A_2] + \text{Source terms} + \text{Storage terms}$$

$$= \rho c_p[\pm\Delta\bar{T}_o(\bar{u}_o - \Delta\bar{u}_o)A_1 + \bar{T}_o\Delta\bar{u}_o A_1 + \overline{u_o'T_o'}A_1 - \overline{u_1'T_1'}A_1 - \bar{w}\bar{T}_2 A_2$$
$$- \overline{w'T_2'}A_2] + \text{Source terms} + \text{Storage terms} = 0 \qquad (6.6)$$

The signs of the turbulent transfer terms are arbitrary since the correlation between u_o' and T_o' is not known. The other terms are positive if they contribute to canyon-air warming.

We will now consider the role of the terms in Equation 6.6. Observations of the air temperature change in the canyon show that the heat storage term is negligible. We will also assume that the horizontal divergence of the turbulent transport terms $\overline{u_o'T_o'}$ is small and may be neglected. This assumption, however, remains untested for a canyon environment. With these assumptions Equations 6.6 reduces to:

$$\rho c_p[(\pm\Delta\bar{T}_o(\bar{u}_o - \Delta\bar{u}_o) + \bar{T}_o\Delta\bar{u}_o)A_1 - (\bar{w}\bar{T}_2 + \overline{w'T_2'})A_2] + \text{Source terms}$$
$$= 0 \qquad (6.7)$$

Under virtually calm conditions the mean flow terms are negligible, and the energy of the source terms is transported out of the canyon by vertical turbulence $\rho c_p(\overline{w'T_2'})A_2$ alone. This would be the ideal case where advection would be zero. Although the energy balance measurements in this study were restricted to very light winds, it was felt necessary to ascertain the magnitude of the first four terms in Equation 6.7 under the experimental conditions. To begin with, we will investigate the size of the first two terms, $\pm\rho c_p \Delta\bar{T}_o(\bar{u}_o - \Delta\bar{u}_o)A_1$; and then the third and fourth terms in combination, $\rho c_p(\bar{T}_o\Delta\bar{u}_o A_1 - \overline{wT}_2 A_2)$.

The terms $\pm\rho c_p \Delta\bar{T}_o(\bar{u}_o - \Delta\bar{u}_o)A_1$ represent the heat transport by the mean wind in combination with the mean horizontal temperature gradient. To evaluate this two instrumented masts were located at the mid-width of the canyon, separated by the length-wise distance L = 28 m, and with the most southerly mast 40 m from the canyon's south end. Sensitive anemometers (C. W. Thornthwaite Assoc.) and thermometers were exposed at 1.8 and 3.7 m above the canyon floor. The thermometers were shielded, and aspirated 26 AWG copper-constantan thermocouples joined to provide temperature differences between the two masts at the two heights. A Gill wind vane (R. M. Young Co.) was also installed between the two masts to measure the wind direction. All signals were monitored every two minutes on the data acquisition system (Chapter 2) and hourly averages calculated. The experiment was conducted during portions of four cloudless days.

Figure 6.2 presents the results for along-canyon winds (from different directions at different speeds). The value of $\bar{u}_o$ is the mean of two levels, and $\Delta\bar{T}_o$ is the mean of the two horizontal gradients. Thus it is assumed that these point measurements approximate the mean cross-section conditions. From what at first appears to be a confused scene, two conclusions

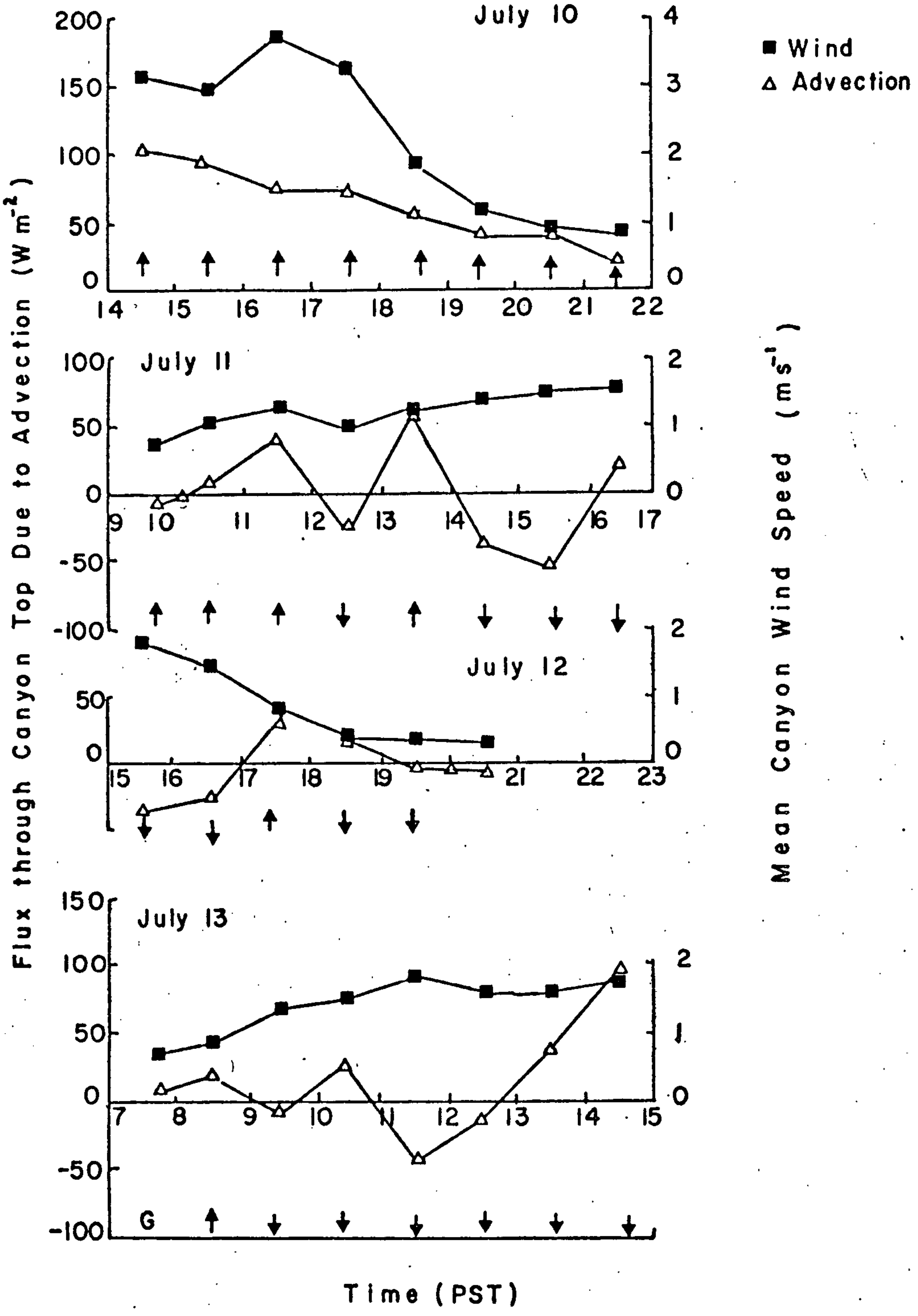

Fig. 6.2 Advection of heat into or out of the canyon $\rho c_p \Delta\bar{T}_o(\bar{u}_o - \Delta\bar{u}_o)A_1/A_2$. [Arrows indicate wind direction-up indicates wind from south].

emerge. Firstly, with winds consistently from one direction along the canyon, the advected energy term is a function of windspeed (e.g., July 10). Secondly, the sign of the advection term is directly related to the wind direction, southerly winds result in a net addition of energy to the canyon-air volume (warming) and northerly winds a net depletion (cooling). This means that the area to the south of the canyon (Grandview Highway) is generally warmer than the canyon, whereas the area to the north (railroad right-of-way) is cooler (see Figure 2.4).

Ignoring the sign of the advection it becomes clear thatthe absolute value of the net transport is related to the canyon wind speed (Figure 6.3). The form of the relation is not certain but an average trend is given by the eye-fit line. This indicates that on average for along-canyon winds of 2 m s^{-1} on cloudless summer days the net advection is about 70 W m^{-2}; and at 1 m s^{-1} the transport is approximately 15 W m^{-2}.

The term of $\rho c_p(\bar{T}_o \Delta\bar{u}_o A_1 - \bar{w}\bar{T}_2 A_2)$ arises from the frictional retardation of airflow along the canyon surfaces resulting in uplift. Components $\Delta\bar{u}_o$ and $\bar{w}$ are related by the equation of continuity for incompressible flow:

$$\bar{w} = \Delta\bar{u}_o \frac{A_1}{A_2} \qquad (6.8)$$

and substitution gives the expression for the mean heat transport as a result of frictional retardation:

$$\rho c_p A_1 \Delta\bar{u}_o (\bar{T}_o - \bar{T}_2) \qquad (6.9)$$

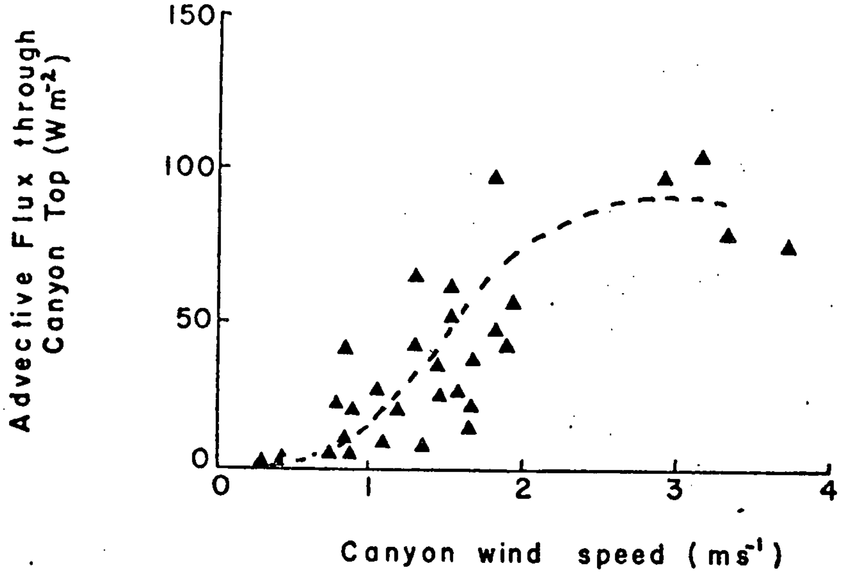

Fig. 6.3 Relation between horizontal advection in the canyon [$\rho c_p \Delta\bar{T}_o(\bar{u}_o - \Delta\bar{u}_o)A_1/A_2$] and mean canyon wind speed. July 10, 11, 12, 13, 1973.

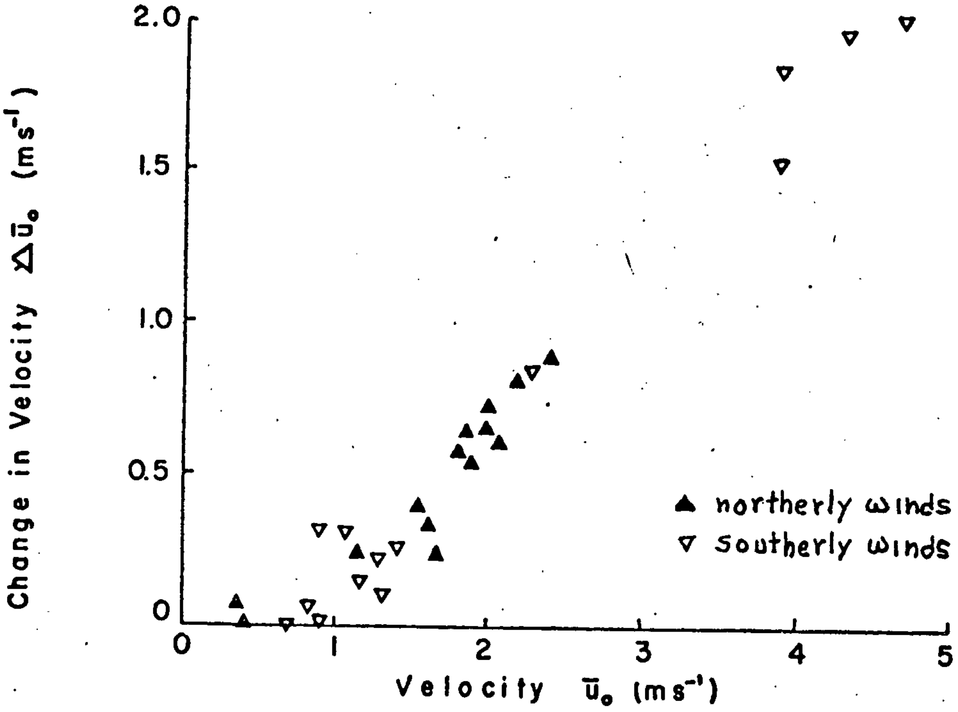

Fig. 6.4 Frictional loss of horizontal velocity in the canyon between two locations 28 m apart. July 10, 11, 12, 13, 1973.

If $\bar{T}_o > \bar{T}_2$ there will be advective warming, if $\bar{T}_o < \bar{T}_2$ cooling, and if $\Delta\bar{u}_o = 0$ advective transport is zero. The observed frictional loss $\Delta\bar{u}_o$ as a function of $\bar{u}_o$ is given in Figure 6.4, using the average data from the two masts and winds from both the north and south. From Equation 6.8 the maximum $\bar{u}_o$ value of 4.75 m s^{-1} corresponds to a vertical velocity, $\bar{w}$ of 1.28 m s^{-1}. No simultaneous $(\bar{T}_o - \bar{T}_2)$ measurements were observed. However, using the results from September with the full moveable mast temperature matrix, maximum $(\bar{T}_o - \bar{T}_2)$ values of 0.2°C were observed in the canyon. This would produce an inflated maximum advective warming of approximately 100 W m^{-2}. More typical values reduce this to about 25 W m^{-2}.

It is concluded that under light wind conditions the total advective transport with along-canyon winds is <100 W m^{-2}. This term will not be accounted for in the energy balances to follow, and must therefore be considered to be an error factor.

2. Flow Across the Canyon

In the case where the mean wind direction is at some angle to the canyon axis, a circulation similar to that shown in Figure 6.1(b) (e.g., Georgii, 1969; Wise 1971) may be expected. In this situation the mean vertical flow may be important in transporting the heat from the canyon into the overlying urban boundary layer. The mean flux across the canyon top will then conform to the following modification of Equation 6.5:

$$Q_{Ht} = \rho c_p \int_{A_2} (\bar{w}\bar{T}_2 + \overline{w'T'}_2) dA_2)/A_2 \qquad (6.10)$$

The existence of such a circulation was visually noted by observing tracers, and by measuring the sign and size of the vertical velocity with a Gill propeller anemometer (R. M. Young Co.). The results in Figure 6.5 are 15 min averages for three locations across the top of a canyon on a day with strong WNW winds. The results confirm that $\bar{w} \neq 0$ with downdrafts over the east wall, and updrafts over the west wall and centre, and thus we must expect the mean circulation term ($\bar{w}\bar{T}_2$) in Equation 6.10 to be operative. There is no reason to believe that under these circumstances the turbulent term $\overline{w'T'}_2$ is absent either, and therefore both measurements may operate to remove (or add) heat from the canyon volume.

When the meso-scale wind direction is normal to the along-canyon axis the horizontal advection illustrated in Figures 6.2 and 6.3 may be assumed to be absent, and the mean vertical circulation exchange expressed by Equation 6.10 will be the dominant non-radiative mode of heat exchange with the canyon surroundings. This form of 'advection' is not expected to be of net importance to the energy balance of the canyon-air volume. This is because unlike the horizontal advection case the air is not free to pass *through* the canyon, it can only enter and exit the

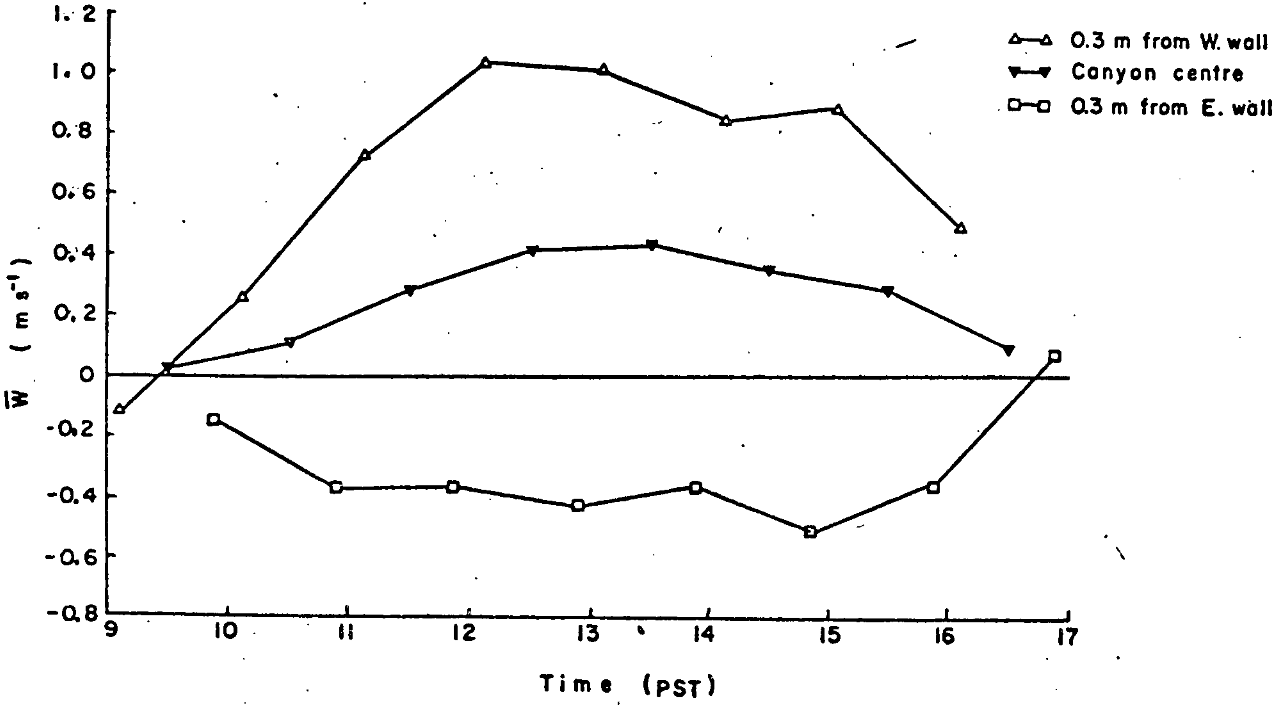

Fig. 6.5 Vertical wind velocities at three canyon locations. October 6, 1973. 15 minute averages. Wind from the west.

canyon via the area A_2 (canyon top). Any net input of energy (i.e., from the heated upwind roof) must result in either a net change in energy storage in the air volume, or a net change in the canyon surface energy balance. The former is not observed in our observations, and the latter although unlikely would be accounted for in the Q^* and Q_G measurements near the interface. Therefore Equation 6.10 will represent the total energy flux from the canyon-air volume that is escaping into the atmosphere during the day. A negative quantity implies a loss of energy while a positive value represents an energy gain by the air volume. In the absence of horizontal advection and radiative flux divergence, the above term equals the total sensible heat incoming or outgoing from the three canyon surfaces.

For the more general case of meso-scale winds at other angles of attack to the canyon the net heat exchange with the surroundings will involve some horizontal advection and some mean vertical circulation transport. This should result in a total 'advective' transport which will be approximately represented by the horizontal advection relation of Figure 6.3.

C. ENERGY BALANCE OF THE CANYON

1. Instrumentation

The energy balance instrumentation for Q^* and Q_G

at the canyon wall and floor surfaces was as in Chapters 4 and 5. Assuming the walls to be 'dry' during the observation period their balance is completed by assuming Q_H to be the balance residual. The gravel over clay floor, however, could be assumed to possess evaporable water even though the surface appeared relatively arid. Correspondingly a miniature weighable lysimeter was installed in the canyon.

The simple design principle followed that of Pasquill (1950). The lysimeter consists of two acrylic tubes (thickness 0.4 cm, length 16 cm), one able to fit inside the other (diameters 10 and 11 cm). The inner tube contains the undisturbed soil sample (closed at the base with a plastic bag cover), and the other tube is sunk in the ground to provide a neat housing and moisture shield. The inner tube is filled with soil by inserting it inside a standard golf hole-cutter, which is then used to core out the undisturbed sample.

The lysimeter was located in the centre of the canyon, and 0.5 m south of the flux plate line. Measurements were made every hour during the energy balance experiment. The inner tube and soil were removed and quickly weighed on a triple-beam balance (Fisher Scientific Co. Ltd.) and then replaced. The balance had a capacity of 2.61 kg, and a resolution of 0.1 g; this gave a resolution of about 10 W m^{-2} in the hourly Q_E estimates (excluding observer and other errors). The sample needed replacement following rain, and after a few days' use.

2. Surface Energy Balance of Component Surfaces

The intensive observation period for energy balance measurement was September 9-11, 1973. The weather was characterized by continuously cloudless skies, and weak winds (usually <2 m s^{-1} by day, and <1 m s^{-1} by night in the canyon). Figure 6.6 shows the three-day average hourly energy balance components for both walls and the canyon floor. Similar diurnal patterns of Q^* and Q_G for each surface have been described and analyzed in Chapters 4 and 5, thus here we will focus on the turbulent terms Q_H and Q_E, and the relative magnitude of the component terms.

For all three surfaces Q_H represents the dominant energy dissipation mode during the daytime. Thus at midday Q_H represents 0.70 - 0.80 Q^* for the dry walls, and 0.60 Q^* for the canyon floor. At night Q_H is very small for all surfaces, and thus for the two walls the nocturnal balance is approximately $Q^* = Q_G \simeq 50$ W m^{-2}. In general Q_H is positive at night (i.e., the canyon air is warmer than the walls and floor) but slightly negative values are evident for the west wall at times. This may be real, but is also probably within instrumental accuracy. The pattern of Q_E for the floor is reasonable giving slight evaporation through the night [again within the instrumental accuracy given in Section C(1)], and peak values ($\simeq$50 W m^{-2}) at midday. This would produce a Bowen ratio ($\beta' = Q_H/Q_E$) of approximately 5.5. Clearly in absolute energy terms the floor

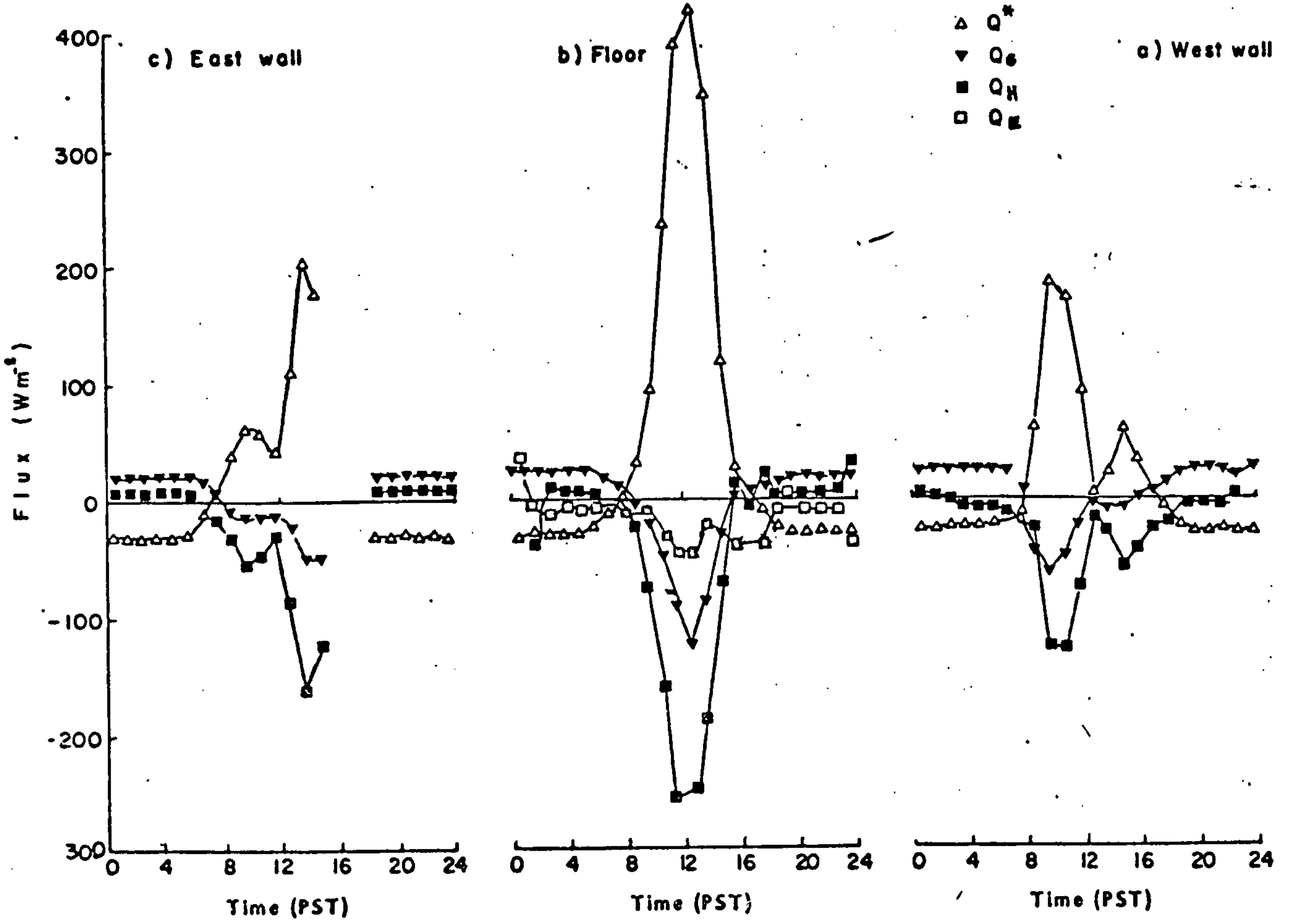

Fig. 6.6 3-day average energy balance components for individual canyon surfaces. September 9, 10, 11, 1973.

is by far the most important exchange surface in the canyon.

3. Energy Balance at the Canyon Top

The diurnal variation of the average energy balance components for the complete canyon system (as in Equation 6.2), are shown in Figure 6.7. Considering the windspeeds during the experimental period it is assumed that the maximum error involved in ignoring the advective terms is approximately 70 W m^{-2} by day, and 15 W m^{-2} by night (Figure 6.3). On most occasions they will be less than these values. It is also important to remember that Q_t^* is obtained from the three surfaces (see Equations 4.3 and 4.4) and is not a measured value. Differences between this quantity and measurement would be important in radiative cooling/warming calculations, but do not significantly affect the residual, Q_{Ht}.

The course of the composite balance components is remarkably smooth considering the differing phase relations for the individual surfaces (Figure 6.6). It is interesting to note that the peak Q_t^* value is 500 W m^{-2}, which is very similar to the 460 W m^{-2} measured over a flat gravel-over-tar roof in central Vancouver at the same time (Brown, personal communication). Equally the nocturnal Q^* loss values agree very closely at both sites, being approximately 70 W m^{-2}. The only significant difference between the two sites is that the times of $Q^* = 0$ occur about one hour later in the morning, and probably

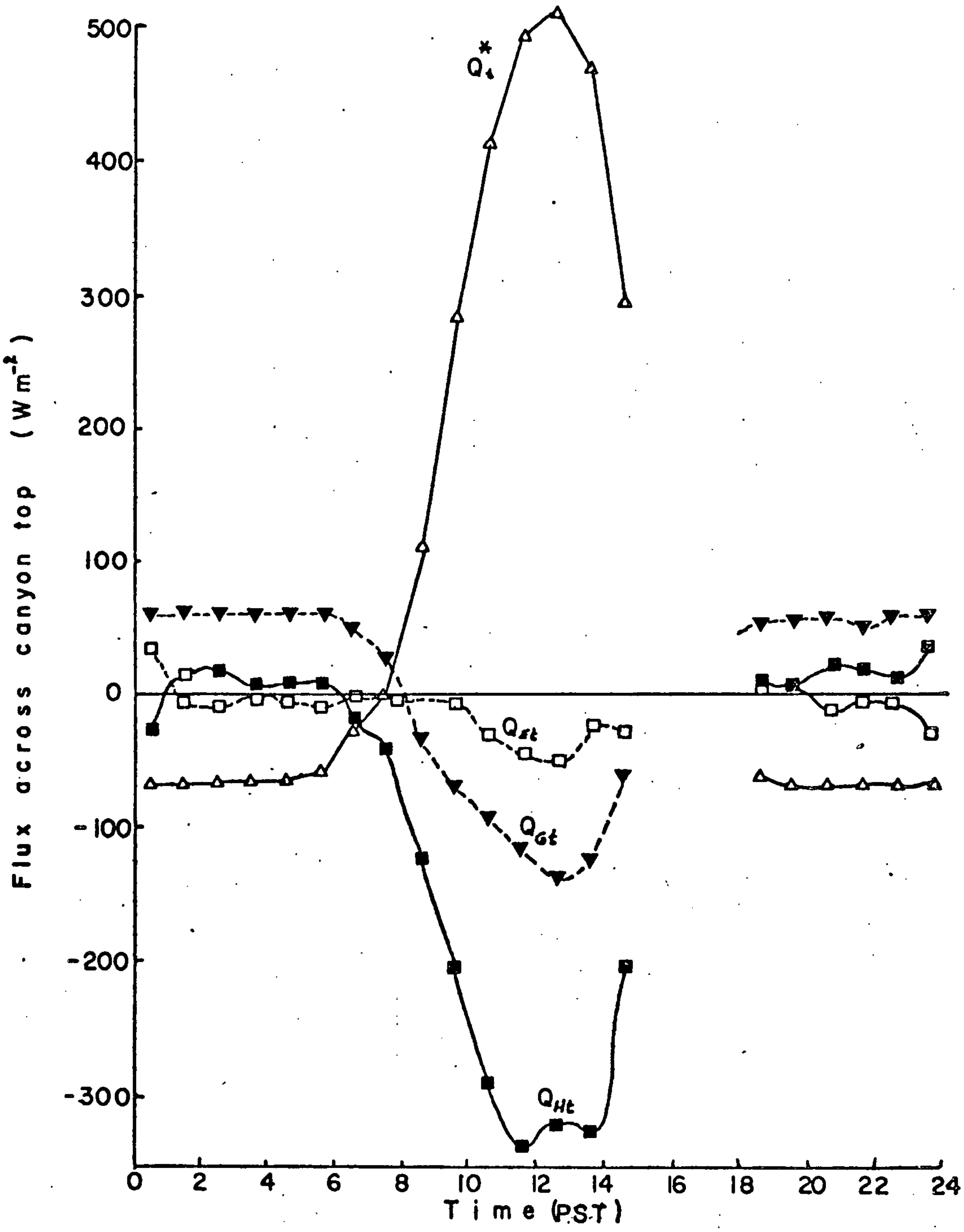

Fig. 6.7 3-day average energy balance components in the canyon. September 9, 10, 11, 1973.

one hour earlier in the evening, at the canyon site. This agreement between roof and canyon values may indicate that the spatial variability of Q^* in an urban area is not large when viewed from an aerial platform.

The relative roles of Q_{Gt}, Q_{Ht} and Q_{Et} show that by day the most important mechanism for heat loss from the canyon is that of sensible heat, and at the peak $Q_{Ht} = 0.66\ Q^*$. By comparison the latent heat transfer is small, so that $\beta_t' = 6.5$ at midday. The role of Q_{Gt} is certainly important in the overall balance so that at the peak $Q_{Gt} = 0.30\ Q^*$. The position of this peak storage is in phase with the net radiation, as noted for $\bar{Q}_G$ earlier in the summer [Figure 5.6(b)], and this is later than for horizontal surfaces (e.g., for flat roof values see Yap and Oke, 1974).

At night the turbulent terms Q_{Ht} and Q_{Et} are small (<25 W m^{-2}) and of opposite sign, thus their net effect is close to zero in the balance. The net loss of long-wave radiation is therefore balanced by drawing upon the subsurface heat storage. The absence of convective activity therefore highlights the conclusion drawn in Chapter 4 that radiative flux divergence is the main air cooling mechanism at night in the canyon under anticyclonic conditions.

There are no energy balance measurements for a canyon with which these results can be compared. To put them in the urban context, however, there are energy balance data for other parts of Vancouver. Yap (personal communication) provides data from above a flat gravel-over-tar roof in central Vancouver. With $Q^* = 500\ \mathrm{W\ m^{-2}}$ at midday on September 1, 1972, Q_H from eddy correlation measurements was about $250\ \mathrm{W\ m^{-2}}$ near the roof, and $200\ \mathrm{W\ m^{-2}}$ at higher levels which were interpreted as representing areal values rather than just for the roof. Perhaps more pertinent to this study, are measurements conducted at 50 m on a tower 4 km downwind of the canyon at the same time as the results in Figure 6.7. The eddy correlation measurements are expected to represent integrated urban Q_H fluxes. Although somewhat variable, the peak Q_H values were approximately $250\ \mathrm{W\ m^{-2}}$ during the period of the canyon experiment. (Brown, personal communication). Thus the canyon results probably represent close to an upper limit for Q_H values in the urban area as we might expect, since water is very restricted there compared to the total urban surface.

4. Canyon Air Cooling/Warming Rates

Canyon air cooling/warming rates were calculated as in Chapter 4, Section E from the hourly mean temperatures in the 7 x 5 matrix. The results for September 9, 1973 are given in Figure 6.8.

At 0800 PST the top of the west wall is in direct illumination and the strongest heating of the air occurs at the same location. Note, however, that the rates of change of

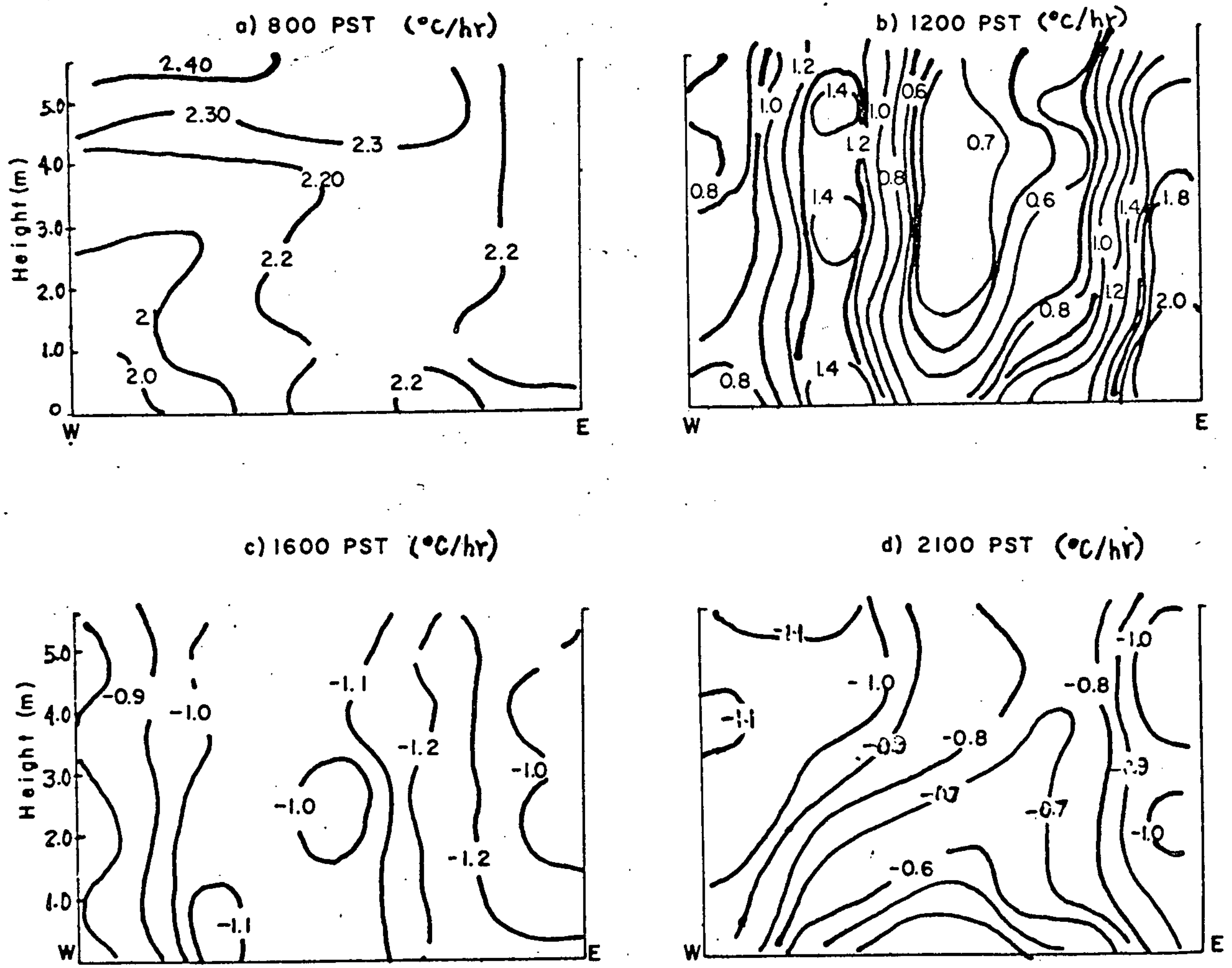

Fig. 6.8 Warming rates in the canyon. September 9, 1973.

air temperature have their highest numerical value of any time of the day in the morning. This may be because the canyon air is stable and is not readily exchanging heat with the exterior. By 1200 PST a very different situation has developed now that the sun is shining directly down the canyon. The strong changes of warming rate in the horizontal may be related to a mean vertical circulation. Such a circulation could arise from external wind effects, internal buoyancy effects, or a combination of these dynamic and thermal causes. By 1600 PST the whole canyon is cooling as it becomes shaded. The strongest cooling occurs on the east wall which has just changed from strong Q^* gain to a loss. The iso-lines of temperature change are still aligned vertically. At 2100 PST the canyon cooling appears to originate from the walls in agreement with theory. The smaller cooling near the floor is somewhat surprising on view factor grounds (see Figure 4.5). A full explanation is not apparent but may be related to the differing heat capacities of the walls and floor (see Table 5.2).

CHAPTER 7

MODELLING CONSIDERATIONS

A. INTRODUCTION

The preceding chapters present and interpret measurements of the energy exchanges and balances in the environment of one specific urban canyon. The purpose was to illuminate the nature of the physical processes operating in such a structure, and their role in establishing the thermal environment of the canyon. In the larger context of urban climatology the canyon is seen as a basic geometrical unit of the urban-atmosphere interface, so that these data may help to establish theoretical and empirical relationships of use in modelling other urban configurations, and possibly an integrated urban surface.

Because the modelling scheme must incorporate some of these empirical relations, the generality of the model is limited by the constraints of the experimental conditions. In particular the model which follows can refer only strictly to surface conditions in the mid-latitudes in summer with cloudless skies, weak airflow and locations where evaporating surfaces are absent. Although such limitations may appear very restrictive, in fact they largely represent conditions under which maximum heat islands and air pollution concentrations are observed, and under which many other models break down. The modelling scheme is directed towards the sensible heat flux which is important in the urban atmosphere because it directly alters the stability.

Figure 7.1 schematically depicts the sequence of steps involved in operationalizing the model proposed here. The theoretical, cloudless sky value of $K\downarrow$ above the surface is calculated in STAGE I. Given the building dimensions and the albedos of the component surfaces the value of K^* is obtained in STAGE II. Using an empirical relationship between K^* and Q^* (developed here) the radiation balance is determined in STAGE III. A similar relationship is employed to obtain Q_G from Q^* in STAGE IV, and thus finally by assuming latent (Q_E) and anthropogenic heat (Q_F) to be negligible, Q_H is obtained as a residual in the surface energy balance (Equation 6.1) in STAGE V.

The need to resort to empirical relationships between K^* and Q^*, and Q^* and Q_G is rooted in fundamental theoretical difficulties which are outlined later in this chapter. The assumption regarding Q_F is validated for the experimental site in summer by the work of Yap (1973) on the urban scale, and by the building characteristics (Chapter 2) on the micro-scale.

Given reasonable adherence to the constraints on this model, it may be possible to apply it not just to a single canyon, but to an array of block-like structures with dimensions and

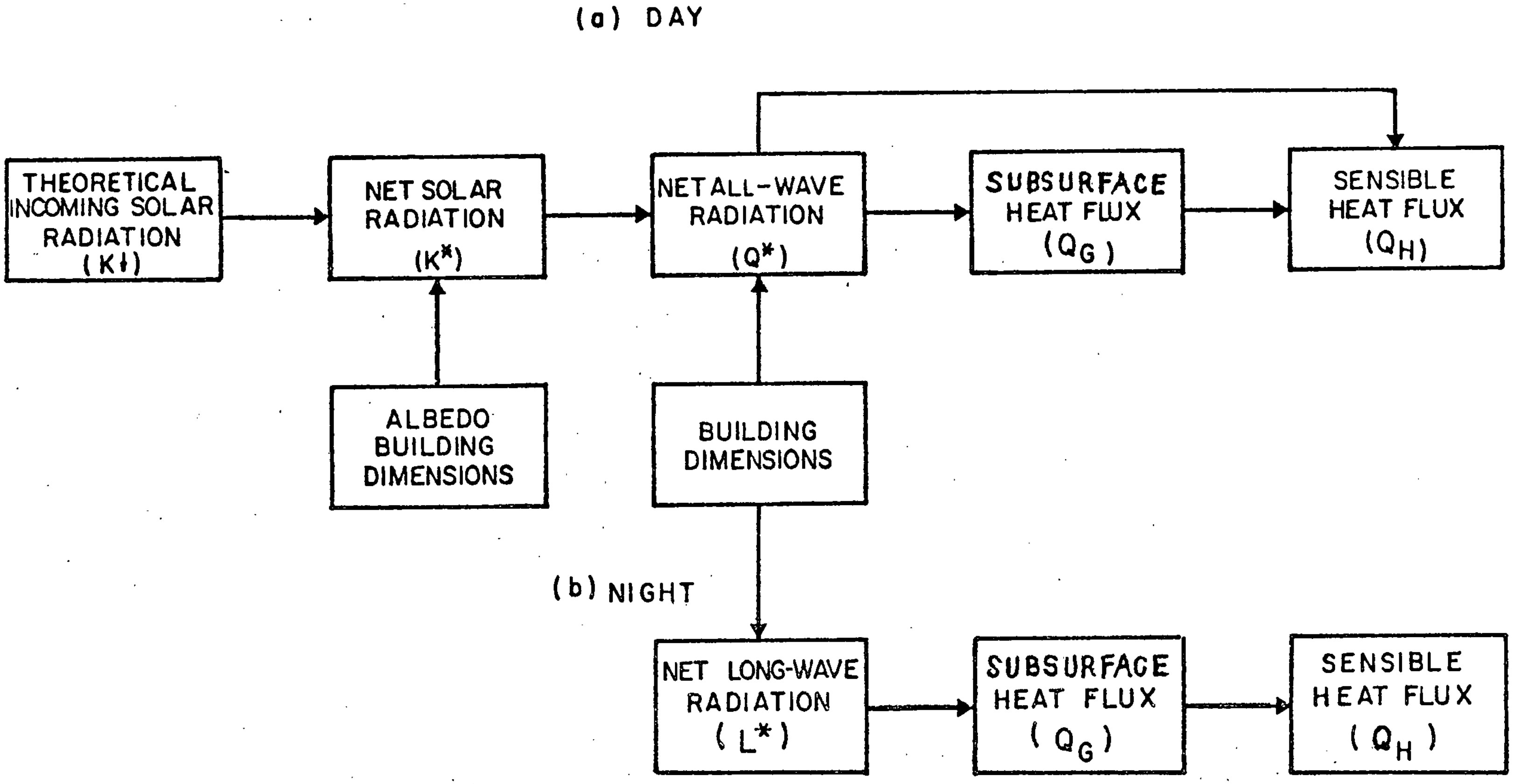

Fig. 7.1. Modelling scheme to obtain sensible heat flux: (a) day; (b) night.

orientation approaching an urban situation. For example, the model may provide a first approximation to the surface energy balance in an urban area characterized by lack of natural surfaces and uniformity in building type. In particular it may provide more realistic surface boundary conditions for dynamic models of the urban boundary layer.

The remainder of this chapter is organized according to the sequence of STAGES involved in the model (i.e., Figure 7.1).

B. STAGE I - CALCULATION OF K↓

The Houghton (1954) model for clear skies, as outlined in Nunez *et al.* (1971), was used to predict incoming solar radiation. In the model the extra-terrestrial radiation is depleted by water vapour absorption and scattering, atmospheric Rayleigh scattering, aerosol scattering and absorption. Houghton assumed that absorption occurs before scattering, and that one-half of the scattered radiation reaches the surface as the diffuse component. The final expression is:

$$K\downarrow = \frac{I_o}{(r^2)} \cdot \cos Z'[(1-\emptyset_w) \overset{\mathrm{I}}{\underset{\mathrm{II}}{\cdot}} (1-S_w) \cdot (1-S_r)\tau_d +$$

$$0.5\ \tau_{d'}(1-\emptyset_w)(1-(1-S_w) \cdot (1-S_r)\ \tau_{d'})] \qquad (7.1)$$

where

I_o = extra-terrestrial solar radiation intensity = 1355 W m^{-2},

r = radius vector of the Sun,

Z' = zenith angle of the Sun,

$\emptyset_w$ = absorption coefficient for water vapour,

S_w = scattering coefficient for water vapour,

S_r = Rayleigh scattering coefficient,

τ_d = transmission coefficient for aerosol absorption and scattering = $(.95)^m$, where m is the solar air mass,

$\tau_{d'}$= transmission coefficient for aerosol scattering or absorption = $(.975)^m$.

Term I represents the direct radiation received at the surface, and Term II the diffuse component. The aerosol transmission coefficient τ_d is a global average calculated by Houghton. Values for $\emptyset_w$, S_w, S_r were also obtained from curves given by Houghton (1954). Nunez *et al.* (1971) assumed that half of the aerosol depletion was due to aerosol scattering. Therefore $\tau_d \sim [\tau_{d'}]^2$. Nunez *et al.* (1971) confirm that this technique provides a good method for obtaining K↓ for a horizontal surface in different aerosol environments. A mean monthly precipitable water vapour of 1.80 cm was used in the calculation of $\emptyset_w$. This value was obtained from Hay (1971). Figure 7.2 shows the agreement between caculated K^* values (using K↓ from the Houghton model, and a mean measured albedo of 0.124), and those measured

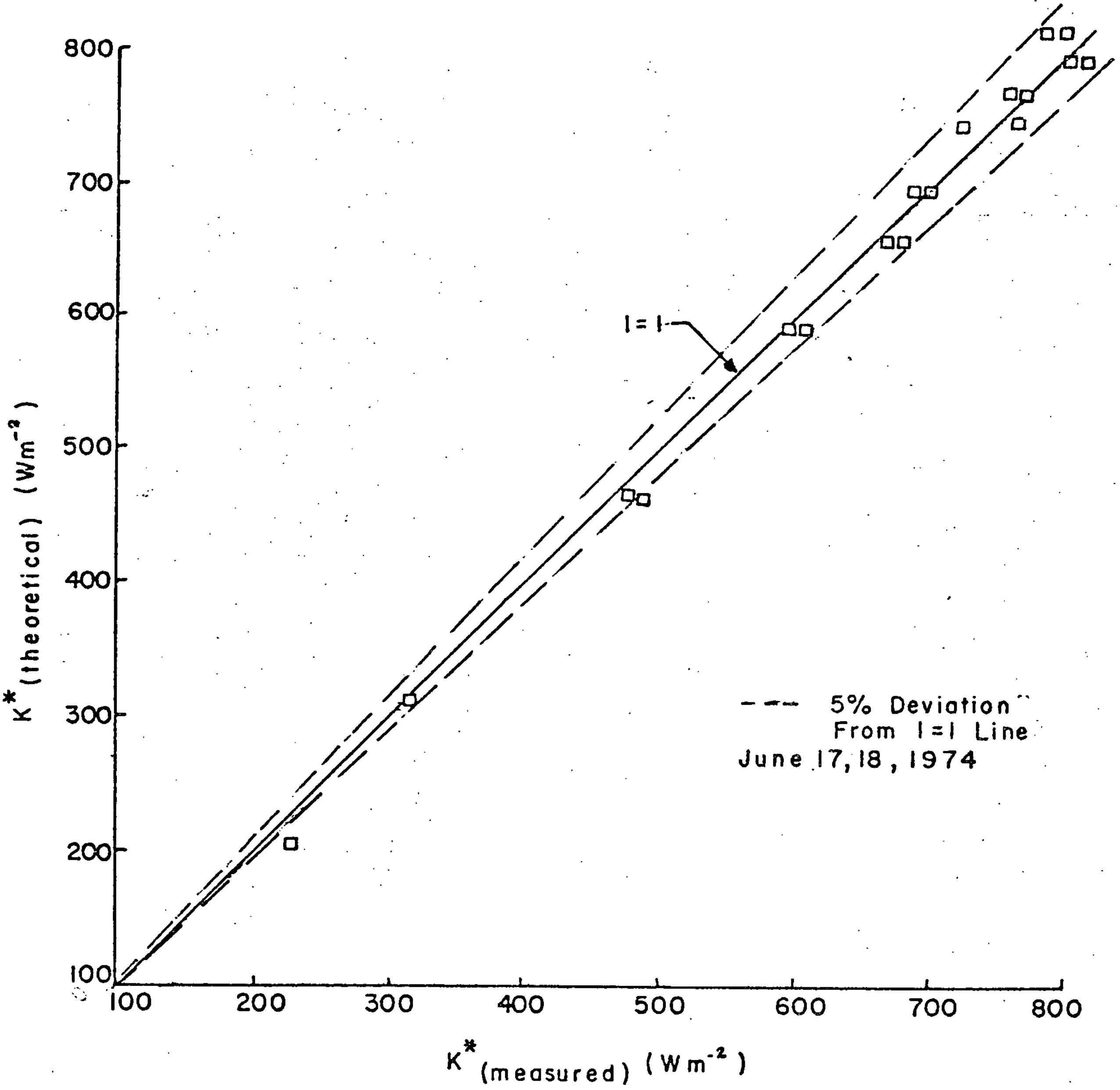

Fig. 7.2 Comparison of calculated and measured net solar radiation (K*) for the Geography Building roof, U.B.C.

over the roof of the Geography Department building at U.B.C. on June 17, 18, 1974. It is now required to devise a modelling scheme which allows similar predictions within a canyon geometry.

C. STAGE II - CALCULATION OF K^* IN THE CANYON

The approach utilized here first involves calculating the solar radiation incident on each of the canyon surfaces (both walls, and the floor). Given the albedo of these surfaces and the canyon dimensions it is then possible to calculate K_t^* from Equation 3.5:

$$K_t^* = (H/W)(K_e^* + K_w^*) + K_g^* \tag{7.2}$$

and also the albedo of the canyon system (α_t) from:

$$\alpha_t = \frac{K{\downarrow}_t - K_t^*}{K{\downarrow}_t} \tag{7.3}$$

where, $K{\downarrow}_t$ is the input from the Houghton calculations averaged across the canyon top. Since this particular experimental canyon has walls of uneven height, $K{\downarrow}_t$ will differ slightly from the Houghton calculation.

The K_t^* model given in Equation 7.2 involves the following assumptions:

(i) diffuse radiation from the sky is distributed over the canyon surfaces according to their surface areas,

(ii) the canyon surfaces are Lambertian and therefore reflect the solar radiation in a diffuse fashion,

(iii) the canyon is of sufficient length such that the surfaces may be considered of infinite extent in view factor calculations,

(iv) there is no loss of solar energy lengthwise from the canyon,

(v) there is no absorption of solar energy in the canyon-air volume.

As an example, the solar radiation incident on each of the three canyon surfaces ($K{\downarrow}_w$, $K{\downarrow}_g$ and $K{\downarrow}_e$) for the early morning is given by:

$$\begin{aligned} K{\downarrow}_w &= (I' \cdot \cos \psi)P + D_w + \Omega_w \\ K{\downarrow}_g &= D_g + \alpha_w \cdot (I' \cos \psi) \cdot VF_{w-g} + \Omega_g \qquad (7.4) \\ K{\downarrow}_e &= D_e + \alpha_w \cdot (I' \cos \psi) \cdot VF_{w-e} + \Omega_e \end{aligned}$$

where

I' = incoming direct radiation after depletion by Rayleigh scattering, water vapour and aerosols, (Houghton model),

ψ = angle of incidence for the canyon walls,

P = per cent of the canyon walls in sunlight,

Ω_e, Ω_w, Ω_g = solar irradiance from secondary reflections on the east, west and ground surfaces,

D_e, D_w, D_g = diffuse radiation incident on the east, west and ground surfaces,

VF_{i-j} = view factor for the irradiated ith surface as seen by the jth surface.

The diffuse radiation from the sky (D) incident on each wall is calculated using the principle of conservation of radiant energy. Denoting F_1 and F_2 as the fraction of the incoming diffuse radiation incident on the walls and ground respectively, we obtain:

$$D \cdot W \cdot L = (D \cdot F_1 \cdot H \cdot L) + (D \cdot F_1 \cdot H \cdot L) + (D \cdot F_2 \cdot W \cdot L) \tag{7.5}$$

The first and second terms on the right-hand side refer to the diffuse radiation incident on the two canyon walls (F_1 is assumed by symmetry to be equal on the two canyon walls). The third term refers to D on the canyon ground. Simplifying,

$$F_1(2H/W) + F_2 = 1 \tag{7.6}$$

and thus an infinite number of solutions exist for F_1 and F_2. The isotropy of the diffuse radiation would best be represented if $F_1 = F_2$, If this is the case F_1 would equal $1/(1 + 2H/W)$ which equals 0.403. Therefore $D_e = D_w = D_g = 0.403D$.

The view factor for each irradiated canyon surface as seen by an opposite canyon surface is calculated as follows. For each point (i) along the receiving surface, the view factor is obtained using Equations 4.5 or 4.6 depending on whether the surfaces are perpendicular or parallel. The mean radiation received on the first surface from the irradiated second surface $K\downarrow'$ is:

$$K{\downarrow}' = I' \cos\psi \cdot \alpha \frac{\sum_{i=1}^{n} VF_{2-i}}{n} = I' \cos\psi \cdot \alpha\, \overline{VF_{2-1}} \qquad (7.7)$$

and the sum is performed over the n receiving points along surface 1. The view factors change with the irradiance of the wall. It is important to realize that this analysis only applies to the irradiated portion of the canyon surface. Other surfaces do not reflect solar energy other than that from the irradiated walls. The outgoing radiation from the sunlit wall was allowed to be reflected a maximum of three times in the canyon since the third order term calculations were small. This term is calculated from Equation 7.7, and is denoted by the symbol Ω in Equation 7.4. The calculation of ψ and P are described in Appendices B and C.

Figure 7.3 shows the net solar absorption by the experimental canyon system (K_t^*) for August 13. Albedos of 0.62, 0.52 and 0.13 were used for the west wall, east wall and ground respectively (see Chapter 3). The comparable experimental data in Figure 7.3 are based on 4 days of observation (August 8, 9, 13 and 14, 1973) and represent instantaneous readings at the given times. In the morning experimental-model differences are <50 W m^{-2}.

In the afternoon, however, the model consistently underestimates the fluxes. The maximum underestimate is ≃50 W m^{-2} at 1400 PST. Reasons for these differences are unexplained, but could include the following:

(i) temporal changes in the attenuation of $K{\downarrow}_t$ due to the diurnal transport of pollutants by the sea breeze circulation,

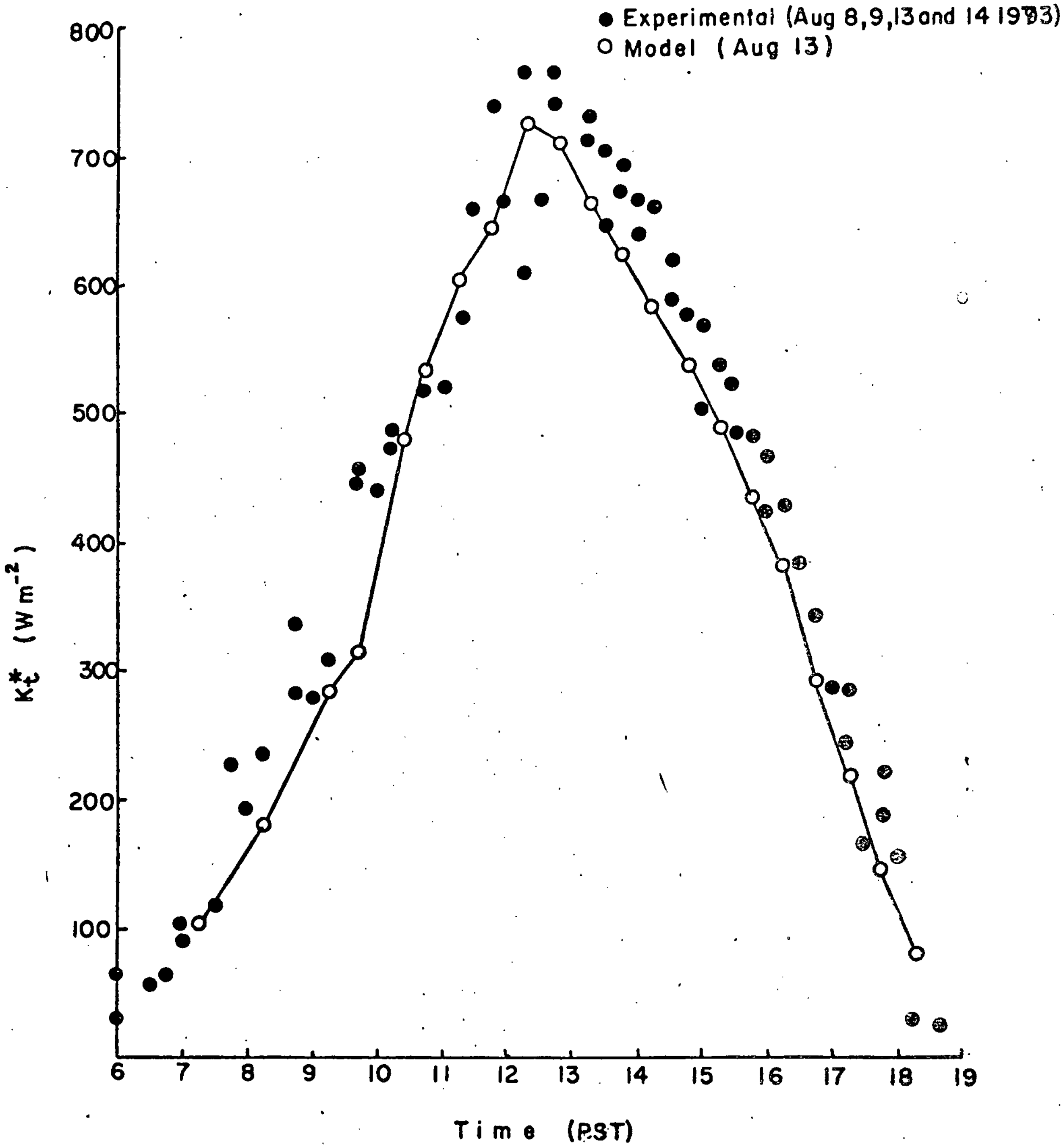

Fig. 7.3 Net solar flux (K_t^*) for the canyon system.

(ii) improper assumptions regarding the radiative properties of the walls and their paint, including the possibility that the surfaces are non-Lambertian,

(iii) measurement errors.

On a mean daily basis the discrepancy between the model and measurements K_t^* above the canyon is about 7% (389 W m^{-2} measured, 365 W m^{-2} calculated). However, the discrepancy between the model and measurements from the individual canyon surfaces is <1% (363 W m^{-2} measured; 365 calculated). This raises the possibility that the measurements above the canyon are in error but this could not be further proven. Thus for daily totals the model is probably adequate, but requires further work to gain confidence in predicting hourly values.

D. STAGE III - THE RELATION BETWEEN K^* AND Q^*

Prompted by difficulties in measuring Q^*, and the low density of standard networks, several studies have attempted to define relations between K^* and Q^*. Monteith and Szeicz (1961) and Davies and Buttimor (1969), among others, have investigated the usefulness of a surface heating coefficient (h) which relates the thermal response of the surface to the net radiant input, and is defined by $h = -dL^*/dQ^*$. According to this approach the relation between Q^* and K^* has the form:

$$Q^* = K^*/(1 + h) + a \qquad (7.8)$$

where a is a constant obtained from a linear regression of Q^* and K^*.

Idso (1968) has criticized the heating coefficient concept on the grounds that it is inappropriate to expect a single constant to represent the interaction of all the exchanges contributing to the thermal balance (and therefore L^*) at a surface. Similarly, on statistical grounds Gay (1971) argued against plotting K^* vs Q^*, and proposed that the long-wave response would be better given by a plot of K^* vs L^*. The slope of this relation ($\lambda = dL^*/dK^*$) will then be negative, zero or positive depending on whether for a given δK^*, $\delta L\uparrow$ is greater, equal or less than $\delta L\downarrow$.

Unfortunately, measurement limitations in this study precluded the implementation of the Gay (1971) approach. In order to obtain Q^* it was therefore necessary to resort to the physically less satisfactory relation between K^* and Q^* (Equation 7.8). Such an analysis is therefore only defended on the grounds of practicality, and no detailed physical interpretations (e.g., heating coefficients) will be pursued. Clearly further work should attempt to follow the physical linkages between K^*, L^* and Q^*.

Hourly Q^* measurements for the individual canyon surfaces on September 1-5, 7, and 9-11 were averaged to obtain a mean $\bar{Q}^*$ day, and Q_t^* was obtained by use of Equation 4.4. Corresponding K_t^* values were computed for September 10, as in STAGE II. The relation between K^* and Q^* is given in Figure 7.4. The canyon results (walls, floor and canyon top) form a well defined relationship for modelling purposes ($r^2 = 0.96$; $S.E._{Q*} = 28.0$ W m^{-2}). This is to be expected since Q^* contains K^* as its dominant term. Equally the roof-top measurements from the U.B.C. Geography Department building show a strong correlation ($r^2 = 0.98$; $S.E._{Q*} = 16.7$ W m^{-2}). The difference between the two could be related to the error in computing K^* for the canyon (Stage II), or measurement errors in K^* for the roof, or it may be real (difference in canyon/roof warming/ cooling rates).

E. STAGE IV - THE RELATION BETWEEN Q_t^* AND Q_{Gt}

Partitioning the net radiant energy into its component turbulent and storage energy fluxes is of central importance in any modelling scheme of the urban energy balance. Given the theoretical difficulties involved in obtaining Q_H (see Chapter 1), this section discusses another approach.

Following Priestley (1959) the ratio of sensible to subsurface heat flux in the absence of evaporation can be described by:

$$\frac{Q_H}{Q_G} = \frac{\rho c_p K_H \partial\theta/\partial z}{k \partial T/\partial z} \qquad (7.9)$$

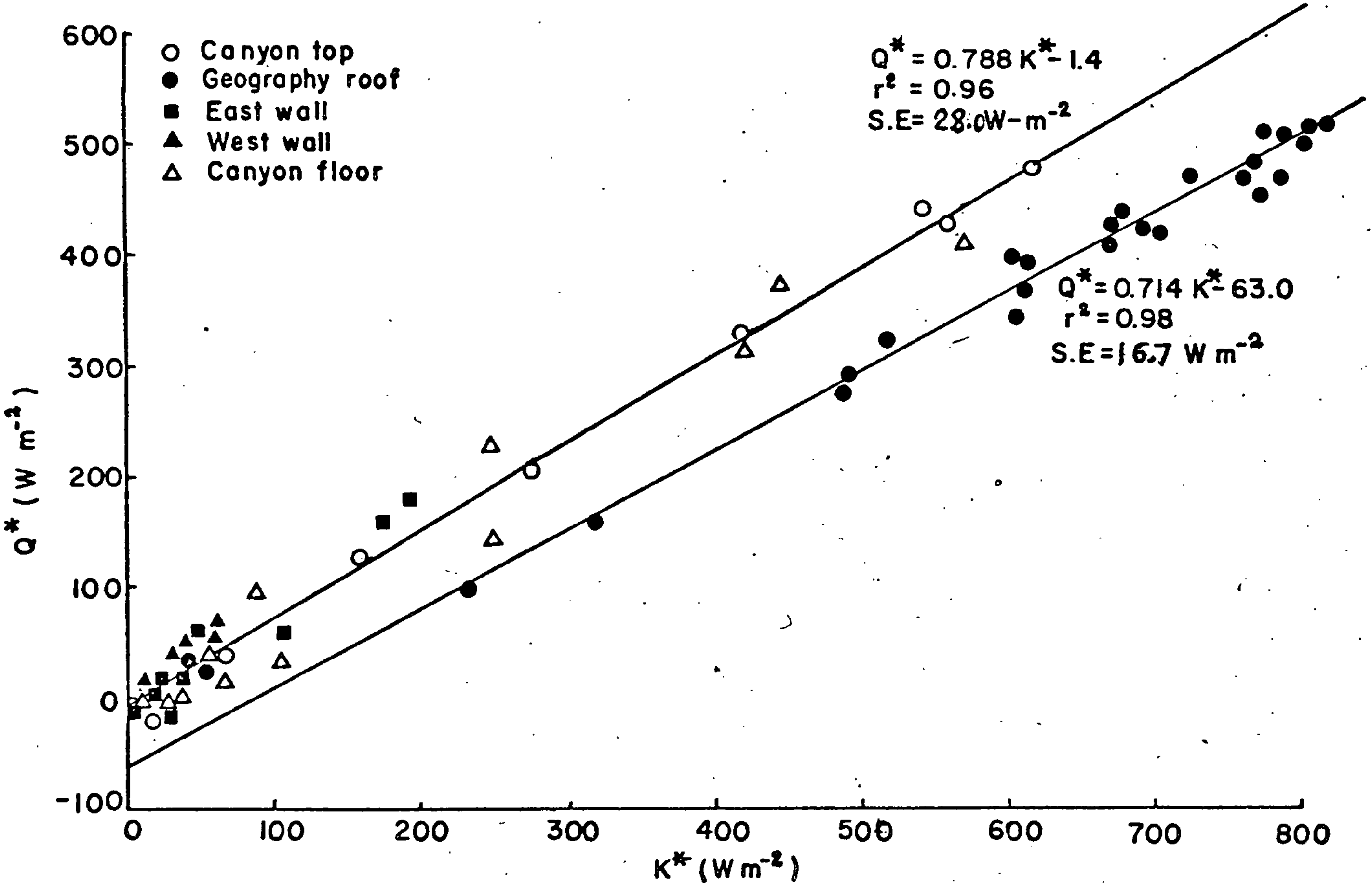

Fig. 7.4 Relation between K* and Q* from canyon and roof measurements. Note that canyon values of Q* are measured hourly average fluxes for September 1-5, 7, 9-11, 1973. K* values for the canyon are corresponding theoretical calculations for September 10, 1973. All roof data are measured hourly averages obtained on June 17, 18, 1974.

where

K_H = turbulent diffusivity for heat,

Θ = potential temperature.

Furthermore the thermal conductivity k can be written in terms of a thermal diffusivity κ:

$$\kappa = k/\rho' c' \tag{7.10}$$

and

ρ' = density of the surface material,

c' = specific heat of the surface material.

Schmidt (1918) derives the following relation:

$$\frac{Q_H}{Q_G} = \frac{\rho c_p \sqrt{K_H}}{\rho' c' \sqrt{\kappa}} = \frac{\rho c_p \sqrt{K_H}}{\mu} \tag{7.11}$$

Thus the ratio of the two fluxes is related to the physical properties of the two media, and to the aerodynamic properties of the location. Therefore under varying synoptic conditions and in the absence of latent heat transfer, K_H is the only term to change in the right hand side of Equation 7.11.

Hourly averaged values of Q_t^* and Q_{Gt} are available for the canyon. Neglecting the small latent heat term, Q_{Ht}/Q_{Gt} can be obtained from $Q_{Ht}/Q_{Gt} = (Q_t^*/Q_{Gt})-1$, and therefore K_H can be obtained for the light wind condition of the experimental period. However, it must remembered that K_H normally refers to a horizontal surface. The resultant K_H obtained in this analysis refers to a canyon configuration. To prevent confusion the canyon diffusivity will be labelled K_H'.

Figure 7.5 shows hourly Q_t^* and Q_{Gt} for the canyon during the calm, cloudless spell in the first half of September. The relationship is well defined. Furthermore, two different regimes are noticed. The late evening, early morning and nighttime data (Q_{Gt} <50 W m^{-2}) have a lower slope than the rest. This is probably due to the lower level of turbulent activity at night. The greater scatter in the >50 W m^{-2} data reflects the variability of the daytime turbulent heat flux. On this basis two distinct regimes in partitioning are recognized, and referred to as the 'night' and 'day' condition regimes.

Using a mean thermal admittance ($\bar{\mu}$) of 1.73 x 10^3 J m^{-2} K^{-1} s$^{-\frac{1}{2}}$, for the three canyon surfaces (Chapter 4), and a value of 1.20 x 10^3 J m^{-3} K^{-1} for the heat capacity of air, the solution to Equation 7.11 is $Q_{Ht}/Q_{Gt} = 0.69 \text{ m}^{-1}\text{s}^{\frac{1}{2}} \sqrt{K_H'}$. Since $Q_{Ht}/Q_{Gt} = Q_t^*/Q_{Gt}-1$ values of Q_{Gt} can be obtained using the slopes of the Q_{Gt} vs Q_t^* relationships (night-weak turbulence; day-strong turbulence) shown in Figure 7.5. The slopes are 2.22 and 4.70 for the night and day cases respectively. These yield values of K_H' of 3.13 m^2 s^{-1} at night and 28.7 m^2 s^{-1} by day. The latter agrees to within an order of magnitude with daytime values of K_H (Sellers, 1965; Priestley, 1959).

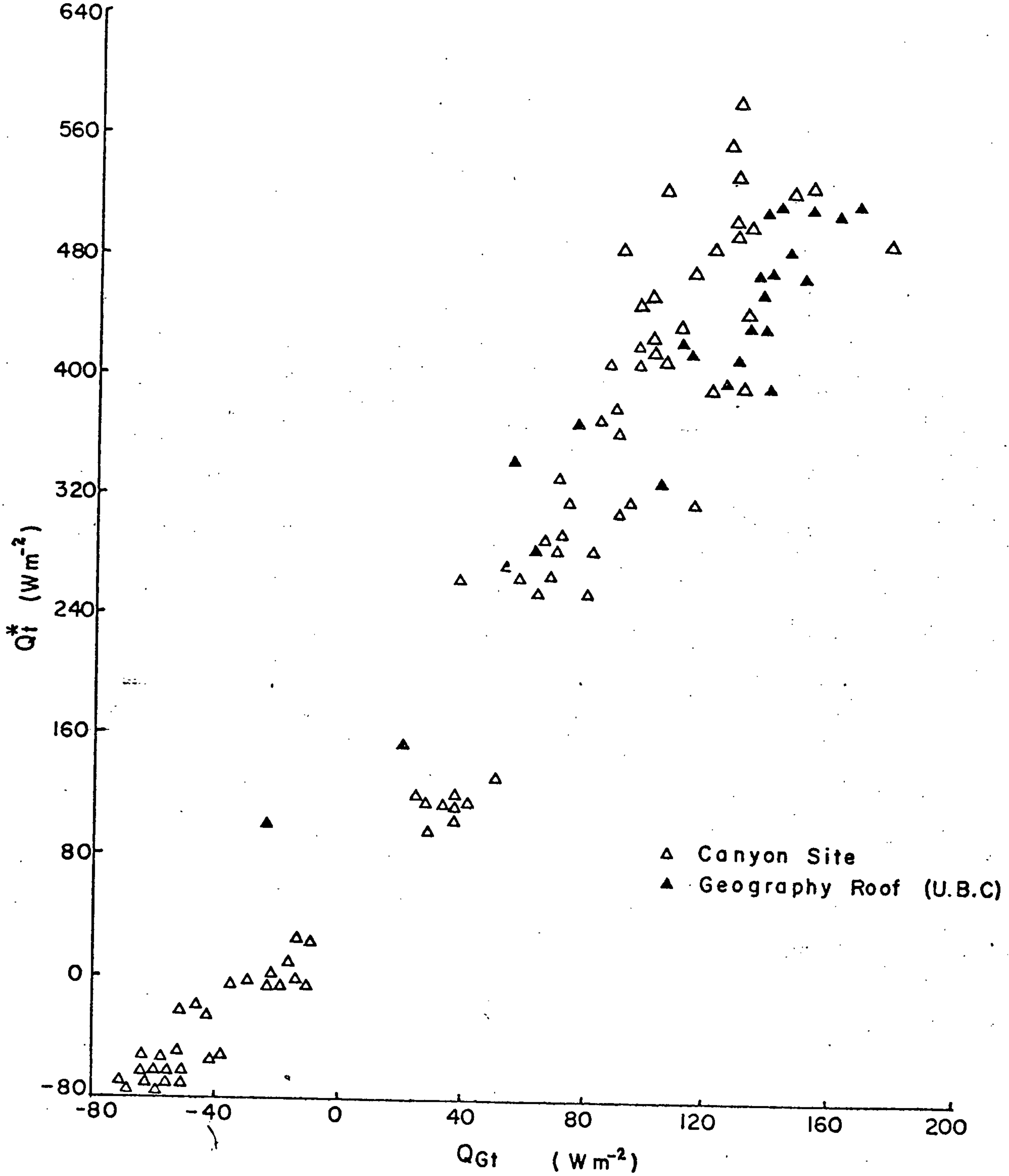

Fig. 7.5 Radiation between hourly Q_t^* and Q_{Gt} for canyon and roof measurements.
September 1-5, 7, 9-11, 1973. (Canyon)
June 17, 18, 1974 (Geography Building roof)

Future work should investigate the relation between Q^* and Q_G for a variety of urban surfaces and configurations under the same synoptic conditions. As a first step in such an analysis, Q^* and Q_G values from the Geography Department roof are included in Figure 7.5. The data represent mean hourly values collected during relatively calm clear conditions on June 17, 18, 1974. The data give indications of a hysteresis loop between the morning and afternoon results. This is similar to the results of Fuchs and Hadas (1972) working over dry loessial soil. If this phenomenon is characteristic of dry, horizontal surfaces, future work must incorporate it into modelling schemes.

F. CONCLUSION

In reviewing the model STAGES it is clear that the solar terms K↓ and K* can be calculated in an urban canyon. In the case of K* this assumes an accurate knowledge of the albedo of the component surfaces. The daytime model was, however, unable to incorporate long-wave exchange in the canyon. At night the situation is simplified, and the relation between L^* and the sky view factor (Chapter 4) is well defined, and in conjunction with a Brunt-type cooling analysis allows calculation of canyon cooling rates (Chapter 4). The relation between Q^* and Q_G is promising, but requires testing in other geometric configurations and for other surface materials.

Since the model is directed towards prediction of Q_H relatively large errors in such intermediate terms as Q_G may be acceptable if the resultant Q_H error is small.

CHAPTER 8

SUMMARY OF CONCLUSIONS

The following major conclusions may be drawn from the preceding study:

[1] In agreement with theoretical models, the diurnal spatially integrated albedo of the canyon system shows three distinct periods. The first and last periods are dominated by a large solar reflection of the east and west walls. The middle period has a low albedo and represents the contribution of the canyon ground. Thus two distinct albedo peaks occur which support the Lambertian assumption for the canyon surfaces. The absorption efficiency of the canyon relative to a horizontal surface varies from a minimum of 1.2 when one of the walls is fully irradiated to a maximum of 1.5 at noon.

[2] The net all-wave radiation is dominated by the solar term during the day. The actual amount of radiant energy received depends on the solar zenith and azimuth angles. Thus the Q^* trace for each wall is characterized by a peak. At night the net long-wave radiation deficit (L^*) in the canyon increases linearly with sky view factor. Divergence of net long-wave radiation is found to exist along the longitudinal

length of the canyon, and total divergence in the canyon-air volume is the main air cooling mechanism at night. Values of Q_t^* and spatially averaged values of k and C gave good estimates of the canyon-air cooling when used in the Brunt equation.

[3] The subsurface heat flux in each canyon wall responds to solar radiation during the day. Therefore a distinct peak in Q_G occurs for each wall as it is irradiated. Divergence of Q_G was found to introduce only a small error in the measurements.

[4] The transport of heat by advection is strongly dependent on the wind field. The hot and cold sources seemed to be localized to the south and north end of the canyon respectively. With winds ~ 2 m s^{-1} on cloudless summer days, the net advection is approximately 70 W m^{-2}. With winds of 1 m s^{-1} the value drops to 15 W m^{-2}. A mean circulation develops along the canyon cross-section if the external wind is at right angles to the canyon length. This mean flow may also be an important mechanism in transporting heat to, or from, the canyon-air volume. Maximum values for Q_t^* and Q_{Gt} at solar noon during a clear summer period are 510 and 140 W m^{-2} respectively. Similarly maximum Q_{Et} is 50 W m^{-2}, while maximum Q_{Ht} is approximately 320 W m^{-2}. At night both Q_{Et} and Q_{Ht} are

close to zero, and a balance seems to be established between Q_{Gt} and the net radiation deficit Q^*_t ($\sim$60 W m^{-2}).

[5] The solar radiation model predicts daily values of K^*_t which agree to within 7% with measured values. However, there seems to be consistently better prediction in the morning than in the afternoon. The relation between computed K^* and measured Q^* is well defined although considerable scatter exists. This relation may possibly be improved by taking simultaneous measurements of Q^* and K^*. Similarly, the relation between Q^* and Q_G is promising, but more measurements are needed over a variety of surfaces.

REFERENCES

Ansori, S. A. and M. Iqbal, 1971: *On Thermal Conductivities of Plant Products*, Dept. of Mech. Eng., Univ. of British Columbia, 37 pp.

Atwater, M. A., 1972: Thermal changes induced by urbanization and pollutants, *Conf. on Urban Env. and Second Conf. on Biometeor.*, Amer. Meteor. Soc., Phil, Penn., 153-158.

Bach, W. and W. A. Patterson, 1969: Heat budget studies in Greater Cincinnati, *Proc. Assoc. Amer. Geogr.*, 1, 7-11.

Barry, R. G. and R. E. Chambers, 1966: A preliminary map of summer albedo over England and Wales, *Q.J.R.M.S.*, 92, 543-548.

Best, A. C., 1931: Horizontal temperature differences over small distances, *Q.J.R.M.S.*, 57, 169-176.

Bornstein, R. D., 1972: Two dimensional non-steady numerical simulations of nighttime flow of a stable planetary boundary layer over a rough warm city, *Conf. on Urban Env. and Second Conf. on Biometeor.*, Amer. Meteor. Soc., Phil., Penn., 89-94.

B. C. Research, 1970: *Air Quality in British Columbia*, Environmental Pollution Studies, Project 2328, 125 pp.

Brooks, D. L., 1950: A tabular method for the computation of temperature change by infra-red radiation in the free atmosphere, *J. Meteor.*, 7, 313-321.

Brunt, D., 1941: *Physical and Dynamical Meteorology*, Cambridge Univ. Press, London, 428 pp.

Carslaw, H. S. and J. C. Jaeger, 1959: *Conduction of Heat in Solids*, Oxford Univ. Press, London, 510 pp.

Clarke, J. F., 1969: Nocturnal urban boundary layer over Cincinnati, Ohio, *Mo. Weath. Rev.*, 97, 582-589.

Craig, C. D. and W. P. Lowry, 1972: Reflections on the urban albedo, *Conf. on Urban Env. and Second Conf. on Biometeor.*, Amer. Meteor. Soc., Phil., Penn., 160-164.

Davies, J. A. and P. H. Buttimor, 1969: Reflection coefficients, heating coefficients and net radiation at Simcoe, Southern Ontario, *Agric. Meteor.*, 6, 373-386.

Davies, J. A., P. J. Robinson and M. Nunez, 1970: *Radiation Measurements over Lake Ontario and the Determination of Emissivity*, First Report, Contract No. HO 81276, Dept. of Geography, McMaster Univ., Hamilton, 85 pp.

Deacon, E. L., 1950: Radiative transfer in the air near the ground, *Australian J. of Sci.*, 3, 274-283.

Delage, Y. and P. A. Taylor, 1970: Numerical studies of heat island circulations, *Bound Layer Meteor.*, 1, 201-226.

Elsasser, W. M., 1942: *Heat Transfer by Infra-Red Radiation in the Atmosphere*, Harvard Meteor. Studies No. 6, Harvard Univ. Printing Office, Cambridge, Mass.

Elsasser, W. M. and M. F. Culbertson, 1960: *Atmospheric Radiation Tables*, Meteor. Monograph 6, No. 23, Amer. Meteor. Soc., Boston, Mass.

Emslie, J. H., 1971: English Bay Weather, *Pacific Yachting*, 4, 20-25.

Emslie, J. H. and J. Satterthwaite, 1966: *Air Pollution Meteorological Relationships at Vancouver, British Columbia*, Meteor. Branch, TEC-605.

Estoque, M. A., 1963: A numerical model of the atmospheric boundary layer, *J. Geophy. Res.*, 68, 1103-1113.

Estoque, M. A. and Bhumralkar, 1970: A method for solving the planetary boundary layer equations, *Bound. Layer Meteor.*, 1, 169-194.

Fleagle, R. G., 1950: Radiation theory of local temperature differences, *J. Meteor.*, 7, 114-120.

Fleagle, R. G., 1953: A theory of fog formation, *J. Mar. Res.*, 12, 43-50.

Fuchs, M. and C. B. Tanner, 1968: Calibration and field test of soil heat flux plates, *Soil. Sci. Soc. Amer. Proc.*, 32, 326-328.

Fuchs, M. and A. Hadas, 1972: The heat density in a non-homogeneous bare loessial soil, *Bound. Layer Meteor.*, 3, 191-200.

Fuggle, R. F., 1971: *Nocturnal Atmospheric Infra-Red Radiation in Montreal*, Ph.D. Thesis, McGill Univ., Montreal, 237 pp.

Funk, J. P., 1960: Measured radiative flux divergence near the ground at night, *Q.J.R.M.S.*, 86, 382-389.

Funk, J. P., 1961: A tabular method for the conputation of the radiative flux divergence near the ground, *J. Meteor.*, 18, 388-392.

Funk, J. P., 1962: Radiative flux divergence in radiation fog, *Q.J.R.M.S.*, 88, 233-249.

Gaevskaya, G. N., K. Y. Kondrat'yev, K. E. Yakusheva, 1963: Flux divergence and heat regime in the lowest layers of the atmosphere, *Izvestia Atm. Ocean Phys.*, 12, 742-748.

Gay, L. W., 1971: The regression of net radiation upon solar radiation, *Arch. Meteor. Geophys. Biokl.*, B19, 1-14.

Georgii, H. W., 1969: The effects of air pollution on urban climates, *Bull. Wld. Health Org.*, 40, 625-635.

Haltiner, G. J. and F. L. Martin, 1957: *Dynamical and Physical Meteorology*, McGraw-Hill, Toronto, 420 pp.

Hare, F. K. and M. K. Thomas, 1974: *The Climate of Canada*, Wiley, Toronto, 256 pp.

Harry, K. F., 1955: *Some Aspects of the Meteorology of the South-western B.C. Coast*, Meteor. Branch, TEC-217.

Harry, K. F., and J. B. Wright, 1967: *The Climate of Vancouver*, Meteor. Branch, TEC-258.

Hay, J. E., 1971: Precipitable water over Canada: II distribution, Atmos., 9, 101-111.

Houghton, H. G., 1954: On the annual heat balance of the northern hemisphere, *J. Meteor.*, 11, 1-9.

Idso, S. B., 1968: An analysis of the heating coefficient concept, *J.Appl. Meteor.*, 7, 716-717.

Idso, S. B., 1971: A simple technique for the calibration of long-wave radiation probes, *Agric. Meteor.*, 8, 235-243.

Idso, S. B., 1972: Calibration of soil heat flux plates by a radiation technique, *Agric. Meteor.*, 10, 467-471.

I.H.V.E. Guide, 1969: Institute of Heating and Ventilation, England.

Kawamura, T., 1965: Some considerations on the cause of city temperature at Kumayaga city, *Tokyo J. of Climatology*, 2, No. 2, 38-40.

Kondo, T., 1971: Effect of radiative heat transfer on profiles of wind, temperature and water vapour in the atmospheric boundary layer, *J. Meteor. Soc. Japan*, 49, 75-94.

Kratzer, P. A., 1956: *The Climate of Cities*, translated by the Amer. Meteor. Soc. Contract No. AF 19(604)-6113, 221 pp.

Kung, E. C., R. A. Bryson and D. H. Lenschow, 1964: Study of a continental surface albedo on the basis of flight measurements and structure of the earth's surface cover North America, *Mo. Weath. Rev.*, 92, 543-564.

Landsberg, H. E. and T. N. Maisel, 1972: Micrometeorological investigations in an area of urban growth, *Bound. Layer Meteor.*, 2, 365-370.

Leahey, D. M. and J. P. Friend, 1971: A model for predicting the depth and mixing layer over an urban heat island with applications to New York City, *J. Appl. Meteor.*, 10, 1162-1173.

Lee, T. H. and J. C. Gille, 1972: Temperature propagation in a non-grey radiating fluid, *Conf. on Atm. Radiation*, Amer. Meteor. Soc., Fort Collins, Col., 271-275.

Lettau, H., 1969: Note on the aerodynamic roughness-parameter estimation on the basis of roughness-element description, *J. Appl. Meteor.*, 8, 828-832.

Lieske, B. J. and L. A. Stroschein, 1967: Measurements of radiative flux divergence in the Arctic, *Arch. Meteor. Geophys. Biokl.*, B15, 68-81.

List, R. J., 1965: *Smithsonian Meteorological Tables*, Smithsonian Institution Press, Wash., 527 pp.

Lynch, A. J. and J. H. Emslie, 1972: *Lower Mainland Air Quality Study*, Final Report, National Health Grant 609-7-209, B.C., 117 pp.

McElroy, J. L., 1972a: A numerical model of the nocturnal urban boundary layer, *Proc. Symp. Air Poll. Turb. and Diff.*, Las Cruces, New Mex.

McElroy, J. L., 1972b: Effects of alternate land-use strategies on the structure of the nocturnal urban boundary layer, *Conf. on Biometeor.*, Amer. Meteor. Soc., Phil., Penn, 185-190.

Monteith, J. L., 1959: Solarimeter for field use, *J. Sci. Ins.*, 36, 341-346.

Monteith, J. L. and G. Szeicz, 1961: The radiation balance of bare soil and vegetation, *Q.J.R.M.S.*, 87, 159-170.

Myrup, L. O., 1969: A numerical model of the urban heat island, *J. Appl. Meteor.*, 8, 908-918.

Myrup, L. O. and D. L. Morgan, 1972: *Numerical Model of the Urban Atmosphere*, 1, Contributions in Atm. Sci. No. 4, Univ. of Cal., Davis, 237 pp.

Nkemdirim, L. C., 1972: A note on the albedo of surfaces, *J. Appl. Meteor.*, 11, 867-874.

Nunez, M., J. A. Davies and P. J. Robinson, 1971: *Solar Radiation and Albedo at a Lake Ontario Tower Site*, Third Report, Contract No. HO 81275, Dept. of Geography, McMaster Univ., Hamilton, 82 pp.

Nunez, M., J. A. Davies and P. J. Robinson, 1972: Surface albedo at a tower site in Lake Ontario, *Bound. Layer Meteor.*, 3, 77-86.

Oguntoyinbo, J. S., 1970: Reflection coefficients of natural vegetation, crops and urban surfaces in Nigeria, *Q.J.R.M.S.*, 96, 430-441.

Oke, T. R., 1972: City size and the urban heat island, *Atmos. Environ.*, 7, 769-779.

Oke, T. R., 1974: *A Review of Urban Climatology 1968-1973*, WMO Technical Note No. 34, World Meteor. Organiz., Geneva, 132 pp.

Oke, T. R. and C. East, 1971: The urban boundary layer in Montreal, *Bound. Layer Meteor.*, 1, 411-437.

Oke, T. R. and R. F. Fuggle, 1972: Comparison of urban/rural counter and net radiation at night, *Bound. Layer Meteor.*, 2, 290-308.

Oke, T. R., G. B. Maxwell and D. Yap, 1972: Comparison of urban/rural cooling rates at night, *Conf. on Urban Env. and Second Conf. on Biometeor.*, Amer. Meteor. Soc., Phil., Penn., 17-21.

Oke, T. R. and G. B. Maxwell, 1975: Urban heat island dynamics in Montreal and Vancouver, *Atmos. Environ.*, (in press).

Pandolfo, J. P., D. Cooley and E. Newburg, 1963: *Preliminary Investigations of Numerical Models for the Short-Period Prediction of Wind, Temperature and Moisture in the Atmospheric Boundary Layer*, Final Report, 7047-7080, The Travellers Research Center Inc.

Pandolfo, J. P., M. A. Atwater and G. E. Anderson, 1971: *Prediction by Numerical Models of Transport and Diffusion in an Urban Boundary Layer*, Final Report, Vol. 1, CPA 70-62, Center for Environment and Man, Inc., Hartford, Connecticut.

Pasquill, F., 1950: Some further considerations of the measurement and indirect evaluation of natural evaporation, *Q.J.R.M.S.*, 76, 287-301.

Peterson, J. T., 1969: *The Climate of Cities: A Survey of Recent Literature*, Nat. Air Poll. Control Admin., Pub. No. AP-59, 48 pp.

Powell, R. W., 1957: Experiments using a thermal comparator for measurements of thermal conductivity, surface roughness and thickness of foils or surface deposits, *J. Sci. Ins.*, 34, 485-492.

Priestley, C.H.B., 1959: *Turbulent Transfer in the Lower Atmosphere*, The Univ. of Chicago Press, Chicago and London, 130 pp.

Probald, F., 1972: Deviations in the heat balance. The basis of Budapest's climate, *International Geog.*, 1972, Univ. Tor. Press, 184-186.

Rider, N.E. and G. D. Robinson, 1950: Notes on the measurement and estimation of atmospheric radiation, *Q.J.R.M.S.*, 76, 37-51.

Rouse, W. R. and J. G. McCutcheon, 1972: The diurnal behaviour of incoming solar and infra-red radiation in Hamilton, Canada, *International Geog.*, 1972, Univ. Tor. Press, 191-196.

Saal, R. N. J., W. Henkelom and P. C. Blokker, 1940: Physical Constants and Asphaltic Bitumens, *J. Inst. Petroleum*, 26, 29-38.

Schmidt, W., 1918: Wirkungen des luftaustausches auf das klima und den taglichen gang der lufttemperatur in der hoke, *Sitzber. Akad. Wissensch. Wien*, 127, 1942-1957.

Sellers, W. D., 1965: *Physical Climatology*, The Univ. of Chicago Press, Chicago and London, 272 pp.

Summers, P. W., 1965: An urban heat island model: its role in air pollution with application to Montreal, *First Cdn. Conf. on Micrometeor.*, Toronto.

Tag, P. M., 1969: *Surface Temperatures in an Urban Environment*, Unpub. M.Sc. Thesis, Dept. of Meteor., Penn. State Univ., 69 pp.

Terjung, W. H. and S. F. Louie, 1973: Solar radiation and urban heat islands, *Annals of the Assoc. Amer. Geog.*, 63, No. 2, 181-207.

Terjung, W. H. and S. F. Louie, 1974: A climatic model of urban energy budgets, *Geog. Annalysis*, 6, 341-367.

Timanovskaya, R. G. and G. P. Faraponova, 1967: Measurements of radiative heat influx in the atmospheric ground layer, *Izvestia Atm. Ocean Phys.*, 3, No. 12, 742-748.

Tuller, S. E., 1973: Microclimatic variations in a downtown urban environment, *Geog. Annaler*, 54, Ser. A., 123-135.

Tyson, P. D., W. J. F. du Toit and R. F. Fuggle, 1972: Temperature structure above cities: review and preliminary findings from the Johannesburg Urban Heat Island Project, *Atmos. Env.*, 6, 533-542.

Vukovich, F. M., 1971: Theoretical analysis of the effect of mean wind and stability on a heat island circulation characteristic of an urban complex, *Month. Rev.*, 99, 919-926.

Wagner, N. K. and T. W. Yu, 1972: Heat island formation: a numerical experiment, *Conf. on Urban Env. and Second Conf. on Biometeor.*, Amer. Meteor. Soc., Phil., Penn., 83-88.

Wise, A. F. E., 1971: Effects due to groups of buildings, *Intnl. Conf. on Architect. Aerodyn., Phil. Trans. Roy. Soc., London*, A269, 469-485.

Wu, S. S., 1965: A study of heat transfer coefficients in the lowest 400 metres of the atmosphere, *J. Geophys. Res.*, 70, 1801-1807.

Yap, D. H., 1973: *Sensible Heat Fluxes in and near Vancouver*, Unpub. Ph.D. Thesis, Univ. of B.C., 177 pp.

Yap, D. H. and T. R. Oke, 1974: Sensible heat fluxes over an urban area - Vancouver, B.C., *J. Appl. Meteor.*, (in press).

Zdunkowski, W. G. and D. C. Track, 1971: Application of a radiative-conductive model to the simulation of nocturnal temperature changes over different soil types, *J. Atm. Sci*, 10, 937-948.

APPENDIX A

HEAT FLUX PLATE CALIBRATION [IDSO (1971, 1972) TECHNIQUE]

The Idso (1972) technique of heat flux plate calibration involves exposing the flux plate to the heat output of a hot plate under controlled conditions.

The hot plate used was made of aluminum (15 x 20 x 1 cm) and the output could be varied from 0 to 20 W. An FD 300 diode was inserted at a depth of 0.5 cm under the centre of the plate. This was achieved by drilling a hole in from one side and parallel to the face of the plate. The diode was sealed in with silicone rubber cement. The temperature given by the diode was assumed to be that of the surface, T_s. The diode output was continuously monitored on a potentiometric strip-chart recorder. The surfaces of the hot plate and the heat flux plate were sprayed with black paint.

The experiment was conducted in a controlled light and temperature environment, with the hot plate placed with its face in a vertical plane, and the heat flux plate suspended parallel to it and 10 cm from its centre. The hot plate was heated to a high temperature (≈50°C), and then allowed to cool to room temperature by altering the power output. During the cooling phase both T_s and the heat flux plate output were monitored.

Under these conditions the total radiation received by the heat flux plate from the blackened hot plate is given as:

$$L\downarrow = \varepsilon.VF.\sigma T_s^4 \qquad (A.1)$$

where VF is the view factor of the hot plate as seen from the heat flux plate. The value of VF was calculated to be 0.495 following the method of Davies *et al.* (1970) and ε was assumed to be 0.95. The flux plate output (μV) will depend upon $L\downarrow$ and therefore T_s. A plot of this output vs $L\downarrow$ yields a straight line whose slope defines a calibration factor (CF) for the flux plate response to a net radiation change ($\mu V/W\ m^{-2}$). Further Idso (1972) shows that the net radiation of the vertical flux plate (Q^*) is related to the heat conducted through the plate (Q_G) by:

$$\varepsilon Q^* = 2Q_G \qquad (A.2)$$

Thus, the calibration of the sample heat flux plate (CF_1) is found to be:

$$CF_1 = \tfrac{1}{2} \cdot \varepsilon\ CF \qquad (A.3)$$

APPENDIX B

CALCULATION OF THE SOLAR ANGLE OF INCIDENCE ON THE VERTICAL WALLS OF THE CANYON (ψ)

By definition, the angle of incidence is the angle between the normal to the surface (vector 1) and the direct solar radiation (vector 2). This angle can be calculated if the direction cosines of the two lines are known with respect to an arbitrary axis. Denoting the angle of incidence as ψ we have:

$$\cos \psi = \cos j_1 \cos j_2 + \cos p_1 \cos p_2 + \cos q_1 \cos q_2 \tag{B.1}$$

where j, p and q are the direction cosines of vectors 1 and 2 against the x, y and z axes respectively.

Choosing co-ordinates with the x-axis normal to the wall; the y axis running horizontal and on the wall; and the z axis vertical and on the wall, we have:

$$\cos j_1 = 1,$$

$$\cos j_2 = \sin Z' \sin(180 - \phi'),$$

$$\cos p_1 = \cos q_1 = 0$$

and ϕ' is the azimuth angle between the solar beam and the canyon longitudinal direction.

Therefore:

$$\cos \psi = \sin Z' \sin \phi'$$

and

$$\psi = \cos^{-1}(\sin Z' \sin \phi'). \qquad (B.2)$$

APPENDIX C

CALCULATION OF SUNLIT PORTION OF CANYON (P)

Figure C.1(a) illustrates the azimuthal geometry of the canyon situation. In C.1(b), a ray grazing the top of the eastern wall strikes the opposite wall at some unknown depth H' measured from the top of the canyon wall. From geometry it can be deduced that:

$$H' = [7.54/\sin \phi']/\tan Z' \tag{C.1}$$

and therefore the sunlit portion of the wall (P) is given as:

$$P = \frac{H' - 1.72 \text{ m}}{5.59 \text{ m}} \tag{C.2}$$

In the late morning sunlight strikes the ground directly and the portion of the ground that is in shadow X_m is:

$$X_m = \frac{7.31(7.54)}{H'} \tag{C.3}$$

so that

$$P = \frac{7.54 \text{ m} - X_m}{7.54 \text{ m}} \tag{C.4}$$

Similarly, in the early afternoon [Figure C.1(d)] the length of shadow is:

$$X_A = \frac{5.59\ (7.54)}{H'} \tag{C.5}$$

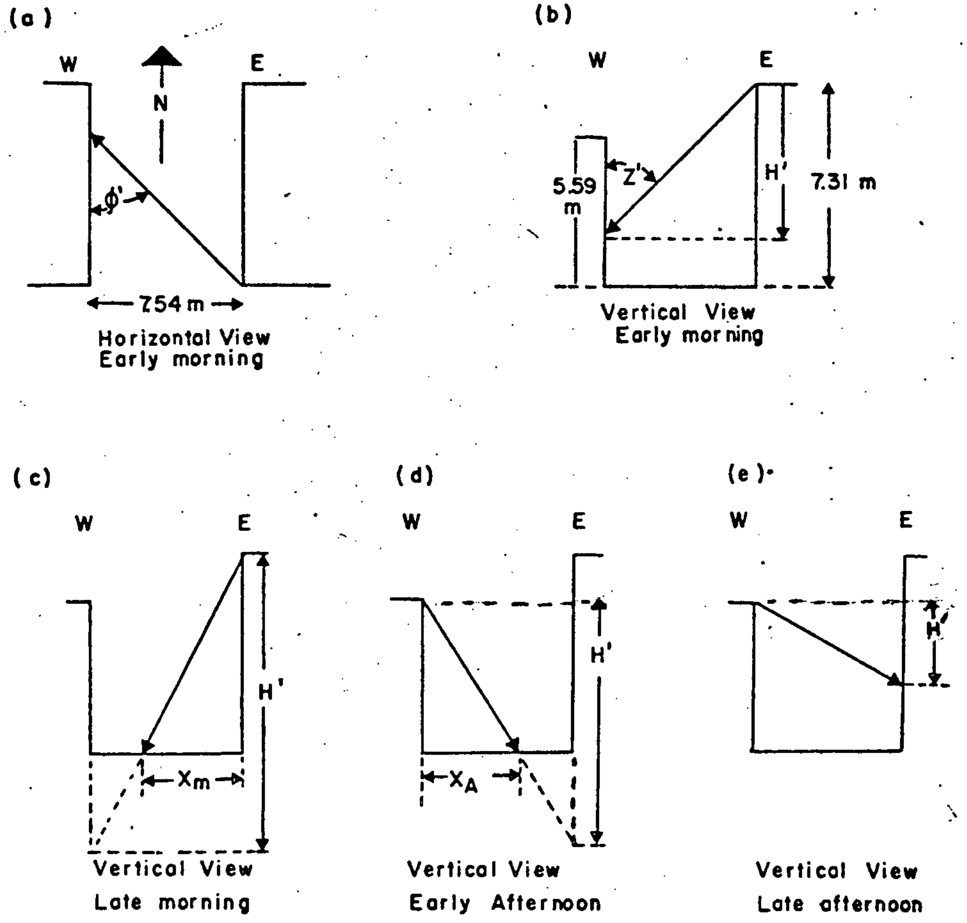

Fig. C.1 Shadow lengths in the canyon.

and

$$P = \frac{7.54\ \text{m} - X_A}{7.54\ \text{m}} \tag{C.6}$$

In the late afternoon [Figure C.1(a)] the total sunlit portion is simply given by:

$$P = \frac{1.72\ \text{m} + H'}{7.31\ \text{m}} \tag{C.7}$$